Local Geoid Determination from GRACE Mission

by

Ramon V. Garcia

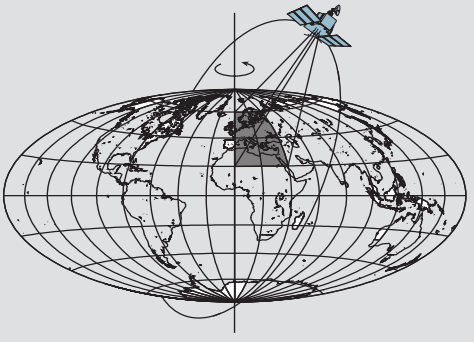

Report No. 460

Geodetic and GeoInformation Science
Department of Civil and Environmental Engineering and Geodetic Science
The Ohio State University
Columbus, Ohio 43210-1275

February 2002

LOCAL GEOID DETERMINATION FROM GRACE MISSION

By
Ramon V. Garcia

Report No. 460

Geodetic Science and Surveying
Department of Civil and Environmental Engineering and Geodetic Science
The Ohio State University
Columbus, Ohio 43210-1275

February 2002

ABSTRACT

An analysis is made about the feasibility of using in-situ GRACE measurements for local gravity field determination as an alternative to global solution methods, which yield solutions in terms of spherical harmonic coefficients. The method investigated is based on integral inversion aided with regularization techniques. The observables considered are potential differences (*DT)* and gravity disturbance differences (*DGD).*

Both observables are affected by position, velocity and acceleration errors. With respect to position errors, the higher precision requirement is in relative position for *DT*, which requires about 1 cm of absolute positional accuracy to produce 0.01 m^2/s^2 error. For velocities, the higher precision requirement is in relative velocity for both *DT* and *DGD.* The observable *DT* required the higher precision 10^{-5} mgal in relative acceleration.

The disturbing potential *T* at the Earth's surface, assumed to be a sphere, can be obtained from values of *DT* and *DGD* given at satellite's altitude. The process turns out to be ill-posed mainly due to gravity field attenuation at the operative altitude of the GRACE mission (300-500 km).

Data error requirements are very demanding for downward continuation of both *DT* and *DGD*. The Tikhonov regularization method was applied for the following configuration: a grid of $0^o.8$ sampling interval for a 24^o square area at 400 km altitude. Measurement errors smaller than $1x10^{-5}$ m^2/s^2 in *DT* are required to achieve solution errors of the level of 1 m^2/s^2 and with a relative error of about 10%. However, this increased to only 3 m^2/s^2 with 0.01 m^2/s^2 measurement error. It is found that model errors due to discrete and finite sampling cause large mean solution errors.

The principal inversion methods employed were the Tikhonov, singular value decomposition, the conjugate gradient and the 1-D fast Fourier transform (FFT) method. Their performance was compared using simulations by employing three test areas with the same configuration described above, but different geographical location. The regularization methods were applied for both *DT* and *DGD* observables Overall, the Tikhonov method performed better than the other methods. For the above configuration, *T* was obtained with about 2.5 m^2/s^2 precision neglecting the mean error.

In the search of the best regularization parameter (α), the L-curve method, which can be applied to the Tikhonov, DSVD and the 1D-FFT, combined with Tikhonov, methods, was analyzed and yielded good results when considering only random errors in the

measurements. However, when considering model errors, the method did not produce satisfactory results. A geometry adaptive method was formulated to find the best α. The method consists of determining a *k* factor that relates the residual norm related to the corner of the L-curve with the residual related to the best α.

Finally, the Tikhonov regularization combined with B-spline smoothing was applied. The method yielded smaller solution errors using the above configuration. The solution errors obtained were about 1.2 and 1.1 m^2/s^2 for $1^o.2$ resolution using *DT* and *DGD*, respectively. The corresponding relative error was about 10%. This could potentially produce about 10 cm geoid for about 150 km resolution. All simulations were made using the geopotential model EGM96.

Acknowledgments: The research documented in this report was supported by a grant from the Center for Space Research, University of Texas, Austin; Contract No. UTA98-0223.

PREFACE

This report was prepared by Ramon V. Garcia Lopez, a graduate research assistant, Department of Civil and Enviromental Engineering and Geodetic Science, under the supervision of Professor Christopher Jekeli. This research has been supported by the Center for Space Research, University of Texas, Austin; Contract No. UTA98-0223.

This report was also submitted to the Graduate School of The Ohio State University as a dissertation in partial fulfillment of the requierements for the PhD degree.

ACKNOWLEDGMENTS

I wish to thank my advisor Dr. Christopher Jekeli for his invaluable support and research guidance. I will be eternally grateful for his amazing patience and time dedicated in correcting my grammar, stylistic, and scientific errors.

I am also grateful to Dr. C. K. Shum for his support and for discussing with me various aspects of this dissertation.

I would also like to thank all the graduate students of my department that I have had the pleasure to work with.

TABLE OF CONTENTS

Page

LIST OF TABLES

LIST OF FIGURES

CHAPTER 1

INTRODUCTION

The accurate determination of the Earth's gravity field benefits sciences like geophysics and geodesy, among others. For instance, in geophysics a better knowledge of the gravity field yields better boundary conditions in the study of the Earth's interior. In geodesy it is essential to obtain a more accurate geoid for the improvement of local and global vertical datum. Moreover, the better the knowledge of the gravity field, the more precise is the satellite orbit determination required for geodetic positioning using satellite methods.

Terrestrial and airborne gravimetric methods do not provide global coverage in our efforts to map the Earth's gravity field. The alternative is by satellite methods that, although they have lower resolution, have the potential of being more efficient and capable of producing better global solutions. In addition to that, satellite methods can be used to determine temporal gravity field variations. These methods are being revitalized with the advent of some satellite gravity mapping missions to be launched within the next five years; the GRACE and CHAMP (already lunched in July, 2000) missions, which are of satellite-to-satellite tracking (SST) type, and the GOCE mission, which is of satellite gravity gradiometry (SGG) type. These three missions will produce an enormous amount of measurements that need to be processed in order to obtain improved solutions of the Earth's gravity field either for regional or global scope. The present study concentrates on the analysis of local gravity estimation using SST data as obtained from the GRACE mission to be launched in November 2001.

1.1 Satellite to Satellite Tracking Methods

As mentioned above, SST (as well as SGG) methods have the potential of playing an important role in gravimetric geodesy. Even though they provide solutions with less resolutions than terrestrial and airborne gravimetric methods they can still significantly contribute to precisely determine and improve the knowledge of the medium and long wavelengths of the terrestrial gravity field and their temporal variations in an efficient way. Moreover, since they are able to produce global data coverage, SST methods can also be used to map those areas of the world for which there are few or no other gravimetric measurements.

There are two important SST configurations; the high low configuration formed by one or more high orbiting satellites (like GPS) and a low-orbiting one; and the configuration

formed by two low-orbiting satellites at about 200-500 km altitude following each other along the same orbit separated by a few hundred kilometers.

Of the two SST configuration types the low-low type is the one that appears to map the Earth's gravity field with better resolution (Reigber, 1988). Unlike the high-low configuration, the two orbiting satellites are being more strongly perturbed by shorter-wavelength variations of the gravity field. This is the main reason why it has received much more attention by geodesists. And so, in this contribution we focus on studying its use for regional gravity field recovery.

1.2 Basic Equations

In SST, the measurements to be considered as observable are usually the intersatellite range rate $\dot{\rho}_{12}$ or line of sight (LOS) velocity and the range-rate rate $\ddot{\rho}_{12}$ or LOS acceleration. We have, in an inertial frame, the following relationship between range rate and the satellite velocity vectors

$$\dot{\rho}_{12} = \mathbf{e}_{12} \cdot \dot{\mathbf{X}}_{12} \tag{1.1}$$

where $\mathbf{e}_{12}$ is the unit vector along the LOS between both satellites and $\dot{\mathbf{X}}_{12} = \dot{\boldsymbol{X}}_2 - \dot{\boldsymbol{X}}_1$ is the velocity difference vector. Here we assign 1 for the trailing satellite and 2 for the leading satellite. On the other hand, the LOS acceleration is given by

$$\ddot{\rho}_{12} = \mathbf{e}_{12} \cdot \ddot{\mathbf{X}}_{12} + \dot{\mathbf{e}}_{12} \cdot \dot{\mathbf{X}}_{12} \tag{1.2}$$

or according to Seeber, (1993)

$$\ddot{\rho}_{12} = \mathbf{e}_{12} \cdot \ddot{\mathbf{X}}_{12} + \frac{\dot{\mathbf{X}}_{12} \cdot \dot{\mathbf{X}}_{12} - \dot{\rho}_{12}^2}{\rho_{12}} \tag{1.3}$$

which can be rewritten as

$$\ddot{\rho}_{12} = \mathbf{e}_{12} \cdot \ddot{\mathbf{X}}_{12} + \frac{1}{\rho_{12}}\left((\dot{y}_{12}^{o})^2 + (\dot{z}_{12}^{o})^2\right) \tag{1.4}$$

The last term on the right-hand side is a centrifugal type term with $\dot{y}_{12}^{o}$ and $\dot{z}_{12}^{o}$ being the components of $\dot{\boldsymbol{X}}_{12}$ perpendicular to the LOS direction, which means that they are independent of the LOS velocity $\dot{\rho}_{12}$. The vector $\ddot{\mathbf{X}}_{12} = \ddot{\mathbf{X}}_2 - \ddot{\mathbf{X}}_1$ represents the vector of acceleration differences where $\ddot{\mathbf{X}}_2$ and $\ddot{\mathbf{X}}_1$ are the total accelerations of the corresponding satellite in an inertial frame. They are given by the sum of the corresponding accelerations $\mathbf{a_1}, \mathbf{a}_2$ (the total specific forces) sensed by an accelerometer and the corresponding gravitational accelerations $\mathbf{g_1}, \mathbf{g}_2$. Then, we can write

$$\begin{aligned}\ddot{\mathbf{X}}_{12} &= \ddot{\mathbf{X}}_2 - \ddot{\mathbf{X}}_1 \\ &= \mathbf{a}_2 + \mathbf{g}_2(\boldsymbol{X}_2) - \mathbf{a}_1 - \mathbf{g}_1(\boldsymbol{X}_1) \\ &= \mathbf{a}_{12} + \mathbf{g}_{12}\end{aligned} \tag{1.5}$$

The main idea is to recover the terrestrial gravitational field. Thus, it is necessary to establish the relationships between the measurements such as $\dot{\rho}_{12}$ and $\ddot{\rho}_{12}$ and the parameters describing the gravitational field. For the case of $\dot{\rho}_{12}$ the relationship can be established, for instance, by using the energy integral of motion (Seeber, 1993), which relates the potential value at the satellite's location with the velocity vector present in equation (1.1). On the other hand, the relationship of $\ddot{\rho}_{12}$ with gravitation can be inferred from equations (1.3) and (1.5).

1.3 Dedicated Missions

In the late 1970's and early 1980's a couple of missions with very similar characteristics where proposed for the concept. The names of the missions were the Gravitational Satellite GRAVSAT (Pisacane and Yionoulis 1980) and the Geopotential Research Mission GRM (Keating et al., 1986). For several years, NASA was pursuing the development of the GRM mission. However, the mission never materialized.

The purpose of the GRM mission was to map the global gravity and magnetic fields to a half wavelength of 100 km resolution with an expected accuracy of 2.5 mgal in the gravity anomaly and 0.1 m in the geoid. The two co-orbiting satellites were supposed to be released from the Space Shuttle in 160 km altitude, circular dual polar orbits. They would be in a drag free orbit due to a Disturbance Compensation System (DISCOS) located at the center of mass of each satellite (Fischell and Pisacane, 1978). The intersatellite distance was considered to be adjustable from 150 to 500 km. Its variation would be measured with a two-way Doppler link operating at frequencies of 42-91 GHz in the continuous wave (CW) band using a highly stable 5 MHz oscillator. The obtained observables were intended to be averaged over 4 seconds and have an accuracy of 1 μm/s.

The mission was designed for about six months providing an equatorial sub-satellite track spacing of 7 km. For orbit determination, the Defense Mapping Agency (DMA) tracking Doppler network was proposed. The expected position accuracy was about 2 meters (Keating, et al., 1986).

1.4 The GRACE Concept

In November of 2001, the Gravity Recovery And Climate Experiment (GRACE) mission, which is also a satellite mission in the low-low configuration, is expected to be launched see (Stanton, 2000). This mission is a joint project between the National Aeronautics and Space Administration (NASA) and the Deutsches Zentrum fur Luft und Raumfahrt (DLR). Its primary objective is to obtain accurate global models for the mean and time-variables components of the Earth's gravity field for up to five years that would benefit oceanography, hydrology, glaciology and solid Earth sciences. Another science objective is to provide several hundred globally distributed profiles every day of the excess delay or bending angle of the GPS transmitted signal due to ionosphere and atmosphere using limb-sounding. These can be converted to total electron content and refractivity in the ionosphere and troposphere, respectively (ibid). In this mission the two co-orbiting satellites will be flying in a near polar, near circular orbit at 300-500 km altitude. The intersatellite distance will be nominally 220 ± 50 km, and it will be measured using a microwave (K-band) tracking system providing two one way ranges at a data rate of 10 Hz, each obtained by comparing an on board generated phase to the received phase. Ultra Stable Oscillators (USO) will provide time tag for the radar measurements. Then, ranges will be averaged or smoothed over ten seconds to provide range rates and range accelerations. The total error in the measured intersatellite range will be 10 microns for 0.1 to 0.0001 Hz. In the case of range rates, the expected accuracy is about 10^{-6} m/s. Each satellite will also carry a geodetic quality GPS receiver to enable accurate orbit determination and a high accuracy superSTAR accelerometer in order to ensure that non-gravitational accelerations due to atmospheric drag, solar radiation pressure, thermal effect, etc, can be accurately modeled and removed. The precision in the accelerometer measurements is about 10^{-10} m/s^2 over 0.1 to 0.00005 Hz (Stanton, 2000). Since the intersatellite distance will only be a few hundred kilometers, the errors due to media effect will be minimized as compared to space-based or ground-based tracking, ensuring homogeneity of data quality over the mission lifetime. External calibration of the on board GPS system will be possible with a dedicated Laser Retro Reflector (LRR) on each satellite. The GPS, together with laser ranging from the ground will ensure precise orbit determination. The employment of the GPS system will actually make this mission a combined low-low and low-high configuration type rather than just the low-low type.

We can see from the above information that the GRACE mission will have important differences with respect to the previous proposed missions. Its satellites will have 300-500 km altitude, while previous missions were considered to be at 150-250 km altitude. It will make use of the GPS system not available before, and unlike GRM, the satellites will have on board accelerometers to measure the non-gravitational forces since they will not be drag-free. The mission, as opposed to the 6 months planned for the previous missions, is projected to endure al least 5 years giving opportunity to study the time variations of the gravity field.

1.5 Low-Low SST Techniques

Several relevant error and performance analyses (Douglas et al., 1980; Rummel, 1980; Jekeli and Rapp, 1980; Pisacane and Yionoulis, 1980) have been made and interesting methods proposed during the last 20 years for processing SST data, specifically in the low-low configuration, for both, global (Kaula, 1983; Colombo, 1984; Sjöberg, 1982; Wagner, 1983) and local applications (Hajela, 1974, 1977; Rummel, 1975; Wichiencharoen, 1985). While some of the methods consider the use of range rates through least squares (Douglas et al., 1980), least squares collocation (LSC) (Colombo, 1981), the expansion in terms of eigenfunction series (Ilk, 1984, 1985, 1987), the energy integral in an approximate way (Fischell and Pisacane, 1978; Gaposchkin, 1998; Wagner, 1983), and its use to get potential differences in a rigorous way (Jekeli, 1998a), some other methods consider the use of range accelerations with least squares (Pisacane and Yionoulis, 1980; Wichiencharoen, 1985), and with LSC (Hajela, 1977, 1978, 1979, 1981; Rummel, 1975, 1980; Rummel et al., 1976; Wichiencharoen, 1985). Most of these studies were made considering GRM type missions. Thus, these methods will yield different results when applied to GRACE measurements. The main reason is the higher altitude of the GRACE orbit. It is well known that gravity attenuates with elevation making the system more unstable causing errors to amplify.

In this contribution, we analyze the use of the in-situ observables potential differences and gravity disturbance differences, obtained from LOS velocity or LOS acceleration measurements, to directly compute disturbing potential values at the Earth's surface in its spherical approximation instead of solving for gravity anomalies or spherical harmonic coefficients, as most of the methods mentioned above do. With this alternative technique, the solution is obtained by integral inversion that relates the in-situ observables to the disturbing potential. The performance of this new approach is analyzed for regional gravity field determination, although it has the potential to be used for global modeling.

1.5.1 Use of Range Rates

One common approach, in the use of the range rate to "map" the terrestrial gravity field consists of assuming that both satellites pass over the same disturbance, which requires ignoring the rotation of the gravity field. Another assumption often made is to consider the range rate to be equal to the in-along-track speed between the satellites since the intersatellite distance is relatively small. Then, based on the energy integral of motion (Seeber, 1993) or the principle of impulse momentum (Wagner, 1983), the following equation is obtained; see for instance, Gaposchkin (1998) and Wolff (1969):

$$\Delta v = \dot{\rho}_{12} = \frac{T_2 - T_1}{v_0} = \frac{\Delta T}{v_0} \tag{1.6}$$

where ΔT is the difference in the disturbing potential, v_0 is the nominal or scalar velocity of the satellite. Then the classical decomposition of the disturbing potential into Fourier components of ordinary Kepler elements (Kaula, 1966) can be used to relate the range

rate to the harmonic coefficients of the disturbing potential. The problem is that, for the GRACE mission, the rotation of the gravity potential has been found to be not small enough to be ignored (Jekeli, 1998), and it could amount to 1 m^2/s^2.

1.5.2 Use of Range-Rate Changes

Now we consider the changes in range-rates or the line of sight (LOS) acceleration between the two GRACE satellites as the measurements. The objective, here, is to derive gravity disturbances which can be used for local gravity modeling, or geopotential modeling. By using equations (1.4) and (1.5) we can write

$$\ddot{\rho}_{12} = \mathbf{e}_{12}^{\mathrm{T}}(\mathbf{a}_{12} + \mathbf{g}_{12}) + \frac{1}{\rho_{12}}\left((\dot{y}_{12}^{\mathrm{o}})^2 + (\dot{z}_{12}^{\mathrm{o}})^2\right) \tag{1.7}$$

After subtracting a normal field (not the usual one, which includes centrifugal acceleration due to Earth's rotation), this equation yields differences of the component of the gravity disturbance vector along the line-of-sight direction. We have

$$\mathbf{e}_{12}^{\mathrm{T}}(\mathbf{a}_{12} + \mathbf{g}_{12} - \boldsymbol{\gamma}_{12}) = \mathbf{e}_{12}^{\mathrm{T}}(\mathbf{a}_{12} + \mathbf{g}_2 - \mathbf{g}_1 - \boldsymbol{\gamma}_2 + \boldsymbol{\gamma}_1) \tag{1.8}$$

then

$$\begin{aligned} \mathbf{e}_{12}^{\mathrm{T}}(\mathbf{a}_{12} + \mathbf{g}_{12}) &= \mathbf{e}_{12}^{\mathrm{T}}(\delta\mathbf{g}_2 - \delta\mathbf{g}_1) + \mathbf{e}_{12}^{\mathrm{T}}\mathbf{a}_{12} + \mathbf{e}_{12}^{\mathrm{T}}\boldsymbol{\gamma}_{12} \\ &= \delta g_{\varepsilon,2} - \delta g_{\varepsilon,1} + \mathbf{e}_{12}^{\mathrm{T}}\mathbf{a}_{12} + \mathbf{e}_{12}^{\mathrm{T}}\boldsymbol{\gamma}_{12} \\ &= \delta g_{\varepsilon,12} + \mathbf{e}_{12}^{\mathrm{T}}\mathbf{a}_{12} + \mathbf{e}_{12}^{\mathrm{T}}\boldsymbol{\gamma}_{12} \end{aligned} \tag{1.9}$$

Where $\delta\mathbf{g}_1$ and $\delta\mathbf{g}_2$ are gravity disturbance vectors at the corresponding satellite location, and $\delta g_{\varepsilon,1} = \mathbf{e}_{12}^{\mathrm{T}}\delta\mathbf{g}_1$, $\delta g_{\varepsilon,2} = \mathbf{e}_{12}^{\mathrm{T}}\delta\mathbf{g}_2$ are their projections along the LOS direction. Substituting equation (1.9) to (1.7) and solving for $\delta g_{\varepsilon,12}$, we have

$$\delta g_{\varepsilon,12} = \ddot{\rho}_{12} - \Phi_{12} - \mathbf{e}_{12}^{\mathrm{T}}\mathbf{a}_{12} - \mathbf{e}_{12}^{\mathrm{T}}\boldsymbol{\gamma}_{12} \tag{1.10}$$

with

$$\Phi_{12} = \frac{1}{\rho_{12}}\left((\dot{y}_{12}^{\mathrm{o}})^2 + (\dot{z}_{12}^{\mathrm{o}})^2\right) \tag{1.11}$$

or, subtracting a reference field

$$DGD = \Delta\delta g_{\varepsilon,12} = \ddot{\rho}_{12} - \boldsymbol{\Phi}_{12} - \mathbf{e}_{12}^{\mathrm{T}}\mathbf{a}_{12} - \mathbf{e}_{12}^{\mathrm{T}}\boldsymbol{\gamma}_{12} - \delta g_{\varepsilon 0,12}$$
$$= \delta g_{\varepsilon,12} - \delta g_{\varepsilon 0,12} \qquad (1.12)$$

In this way, we can obtain differences of gravity disturbances in the direction of $\mathbf{e}_{12}$ in terms of the LOS acceleration, the inter-satellite range and the velocity components perpendicular to the LOS, (these two last quantities are contained in the centrifugal term), and the measurement of non-gravitational forces contained in $\mathbf{a}_{12}$. The gravity disturbance component as in equation (1.10) can be used to obtain by integral inversion disturbing potential values at the Earth's surface. According to Hotine, (1968), the relationship between the disturbing potential given at the Earth's surface, considered to be a sphere, with the gravity disturbance at some elevation can be defined by a functional of Poisson's integral, see (chapter 3).

In the past, one popular method to process SST data was the computation of gravity anomalies from line-of-sight accelerations (Jekeli and Rapp, 1980; Colombo, 1984; Hajela, 1974; Rummel, 1975, 1980). Results from some studies (assuming GRM, GRAVSAT type missions) showed that gravity anomalies could be determined with about 4-6 mgal accuracy and geoid undulations with accuracy of about 10 cm for 100-140 km resolution (Jekeli and Rapp, 1980; Hajela, 1981; Rummel, 1980).

1.5.3 The Energy Integral

The idea of using the energy integral for a satellite was introduced by Bjerhammer, (1968). Later on, Wolff, (1969) proposed its use for the low-low concept according to equation (1.6). This technique has been considered and analyzed by other geodesists, see for instance Fischell and Pisacane (1978); Rummel (1980); Sjöberg (1982) and Wagner (1983). The basic idea of this approach is to approximate the potential difference between both satellites by the range rate multiplied by the satellite's total velocity. The assumptions involved may not make the method adequate for the GRACE mission, if very precise gravitation field determination is desired. The approximations would involve model errors up to 0.5 m^2/s^2 (Jekeli, 1998b). Moreover, since the rotation of the gravitational field, which is also neglected is of the order of 1 m^2/s^2 (ibid.), Jekeli (1998a) has derived a rigorous method to obtain potential differences from absolute and relative satellite velocities. No approximation in the relative velocity is made and the rotational gravitational potential is considered.

We start with the energy equation for the satellite, which relates the total velocity with the potential of gravitation at the satellite's location in an inertial frame. For a non-rotating Earth and with no non-conservative fields, the energy equation is given by (Seeber, 1993)

$$\frac{1}{2}v^2 - V = E \qquad (1.13)$$

where v is the scalar satellite velocity, V is the earth's gravitational potential at the satellite's location and E is a constant of energy. The Earth's rotation causes the gravitation at a specific point in space to change in time. In order to account for this variation, the energy equation is written as follows, see Jekeli (1999):

$$\frac{1}{2}v^2 - V = -\int_{t_0}^{t} \frac{\partial V}{\partial t} dt + E \tag{1.14}$$

In order to approach reality, the vector containing the specific forces $\boldsymbol{F} = (\boldsymbol{F}_x \quad \boldsymbol{F}_y \quad \boldsymbol{F}_z)$ acting on the satellite also needs to be considered. Then we write

$$V = \frac{1}{2}v^2 - \int_{t_0}^{t} \boldsymbol{F} \cdot \dot{\mathbf{X}} dt + \int_{t_0}^{t} \frac{\partial V}{\partial t} dt + E \tag{1.15}$$

Assuming that we measure the satellite's velocity along its orbit, as well as the specific forces acting on the satellite we can obtain the potential from equation (1.15). We ignore the gravitational effects from the sun, moon and other planets gravity field on the potential at satellite's location. For the second integral in the right hand side of equation (1.15) we have the following equation (ibid):

$$\int_{t_0}^{t} \frac{\partial V}{\partial t} dt = \omega_{\mathrm{e}} \left(y\dot{x} - x\dot{y} \right) + E \tag{1.16}$$

Then, solving for the potential in equation (1.14)

$$V = \frac{1}{2}v^2 + \omega_e(\dot{x}y - x\dot{y}) + E \tag{1.17}$$

For a pair of relatively close satellites we can compute the potential difference the point of location of each satellite

$$V_2 - V_1 = V_{12} = \tfrac{1}{2}(v_2^2 - v_1^2) + \omega_e(x_2\dot{y}_2 - \dot{x}_2 y_2 - x_1\dot{y}_1 + \dot{x}_1 y_1) + E_{12} \tag{1.18}$$

with $\boldsymbol{X} = (x, y, z)$, $\dot{\boldsymbol{X}} = (\dot{x}, \dot{y}, \dot{z})$ being the position and velocity vectors, respectively; also $v^2 = \dot{\boldsymbol{X}} \cdot \dot{\boldsymbol{X}}$ and $\dot{\boldsymbol{X}}_{12} = \dot{\boldsymbol{X}}_2 - \dot{\boldsymbol{X}}_1$. After some arrangements we obtain

$$V_{12} = \dot{\boldsymbol{X}}_{12} \cdot \dot{\boldsymbol{X}}_1 + \tfrac{1}{2}\dot{\boldsymbol{X}}_{12} \cdot \dot{\boldsymbol{X}}_{12} + \omega_e(x_1\dot{y}_{12} + x_{12}\dot{y}_1 + x_{12}\dot{y}_{12} - \dot{x}_1 y_{12} - \dot{x}_{12} y_1 - \dot{x}_{12} y_{12}) + E_{12} \tag{1.19}$$

Equation (1.19) can be considered a model for the potential difference if the velocity vectors of both satellites are considered as measurements. By subtracting a reference field we obtain an expression for differences of disturbing potential

$$DT = V_{12} - V_{012} \tag{1.20}$$

where V_{12} is computed with equation (1.19) and V_{012} is the potential difference computed from a reference field. Some initial error analyses (Jekeli, 1999) indicate that errors of $1x10^{-4}$ m/s in absolute velocities and of $1x10^{-6}$ m/s in range-rates can yield errors of about 0.01 m^2/s^2 in potential differences, which is comparable to millimeter accuracy in geoid undulation differences at satellite altitude. As with gravity disturbances, potential differences can also be used to obtain the disturbing potential at the Earth's surface through inversion, in this case directly using Poisson's integral.

1.6 Regional Integration with In-situ Measurements

One important approach in the recovery of the gravitational field from SST observables consists of solving for the spherical harmonic coefficients of global geopotential models (Sjöberg, 1978, 1982; Wagner, 1983; Reigber, 1988; Tapley, 1973). One of the methods, being considered by The University of Texas to process GRACE data, is a non linear orbit determination and parameter recovery method (Tapley, 1973). This method makes use of Newton's equation of motion, which characterize the vehicle's trajectory:

$$\ddot{\mathbf{X}} = \frac{\mu \boldsymbol{X}}{\left|\boldsymbol{X}\right|^3} + R(\boldsymbol{X}, t) \tag{1.21}$$

where μ is the gravitational constant and R is the vector of perturbations. The acceleration vector $\ddot{\mathbf{X}}$ can be considered as a function of the satellite's position and velocity vector at time t, and a vector $\boldsymbol{\alpha}$ containing constant parameters that characterize the perturbing forces like the non-spherical gravitational potential, which on its own, is parameterized in terms of spherical harmonic coefficients.

$$\ddot{\mathbf{X}} = f(\boldsymbol{X}, \dot{\boldsymbol{X}}, \boldsymbol{\alpha}, t) \tag{1.22}$$

The relationship in equation (1.22) is not linear. Then, the linearization will require some initial approximation of the unknown parameters. Once the initial values are available the quantities to be solved are the corrections ($\delta \mathbf{x}$) to those initial values. In the case of the parameters, $\boldsymbol{\alpha}$, the corrections are $\delta\boldsymbol{\alpha}$. The solution is obtained by least squares adjustment (Tapley, 1973)

$$\delta\boldsymbol{\alpha} = \left(H^T R^{-1} H\right)^{-1} H^T R^{-1} \delta\mathbf{x} \tag{1.23}$$

where H is the matrix containing the partial derivatives of the observations **x** (composed of the satellite's position and velocity vectors) with respect to the parameters $\boldsymbol{\alpha}$; and R is the variance-covariance matrix of the observations. Since the actual observations could be range, range-rate, and/or range acceleration the orbital state vectors $(\boldsymbol{X}, \dot{\boldsymbol{X}})$,need to be expressed in terms of these, which is relatively simple.

Another approach to obtain gravity parameters, consists of using gravity induced linear orbit perturbations. This method is based on the fact that of all perturbing forces acting on a satellite the force produced by the anomalous part of the geopotential is dominant, especially for low orbiting satellites. Thus the deviation of a satellites motion from central force motion will be produced mainly by the anomalous potential. The method uses the classical decomposition of the disturbing potential into Fourier components of ordinary Kepler elements (Kaula, 1966) to relate the range rates to the harmonic coefficients of the disturbing potential. The solution of these coefficients is also done by least squares adjustments. As with the previous method, the solution involves the inversion of large systems of equations and hence involves large amounts of computation time. This method has been applied in some SST analyses for gravity recovery (see e. g., Kaula, 1983; Wagner, 1983; Mackenzie and Moore, 1997).

One alternative to the above methods is the direct use of in-situ observations as values given on a boundary surface. These values can be related to the geopotential gravitational field either through spherical harmonic expansion, which is suited for global model solutions or through integrals like Poisson's, which can be used for regional gravity determination. This study focuses on the latter approach. As mentioned before, the potential and the gravity disturbance differences obtained from range rates and range rate rates, respectively, can be related to the potential at the Earth's surface by using Poisson's integral (Heiskanen and Moritz, 1966, Hotine, 1968). In this way, in-situ measurements can, in principle, be used to solve directly for the disturbing potential at the Earth's surface. Some initial tests have yielded better results with this approach than with direct estimation of spherical harmonic coefficients in the polar areas where the in-situ measurements are densest (Jekeli and Garcia, 2000). Still, a more broad and profound analysis is required.

1.7 The Downward Continuation

One important problem of SST and SGG methods is the downward continuation of measurements from satellite height to the earth's surface where the solution is required. The downward continuation is an ill-posed problem, since the gravity field attenuates with altitude. This causes small measurement and systematic errors to amplify. Therefore, downward continuation of SST measurements needs to be stabilized by an appropriate regularization or smoothing. This fact obliges us to be more careful with measurement and model errors. Especially for the GRACE mission, in which the altitude will be higher than in previously missions contemplated, the instability of the solutions will be more severe. In order to illustrate the amplification of errors, Poisson's integral was used to downward continue potential values given a 30x30 grid with $0^o.4$ sampling interval and at

400 km altitude. Random errors with standard deviation of ± 0.01 m^2/s^2 were added to the potential values. The downward-continued potential values without regularization were in error by up to $1x10^6$ m^2/s^2 at the Earth's surface.

Some geodesists have addressed the downward continuation problem with different regularization techniques: least squares collocation (LSC) with smoothed data (Hajela, 1977, 1978, 1979); stabilized integrals (Rummel, 1980); singular value decomposition, (Schwarz and Gerstl, 1979); the Tikhonov method (Schwarz, 1979 ; Ilk, 1993, 2000); and the conjugate gradient method (Schuh et al., 1996). Some of the analyses have concentrated on SGG, see for instance (Klees et al., 2000), (Arabelos and Tscherning, 1990), and (Schuh, 1996).

One difficulty associated with regularization methods is the determination of the optimum regularization parameter (α) involved (Schwarz, 1979; Bouman, 1998; Ilk, 1993; Hansen and O'Leary, 1993). For small α a good approximation to the least square estimator is obtained but the effect of data errors are large. Large α suppresses data errors but increase approximation errors. No precise recipe for the choice of α has been discovered, which could be used for any problem. There are some iteration-based methods like the discrepancy principle (Bouman, 1998). However, they do not always lead to the best solution even if convergence is achieved (Ilk, 1993). The convergence is more difficult to achieve as the process becomes more unstable. A method, called the L-curve method (Hansen and O'Leary, 1993), to compute the best regularization parameter and that is based on the trade off between perturbation and regularization errors have yielded relatively good results in some tests made in this research.

This study also concentrates on analyzing the performance of regularization and the determination of the best α using the L-curve method. Tests were made to analyze effects of measurement and model errors, data altitude, sampling interval and integration area on solution errors.

1.8. Fourier Methods

Fourier technology can also be exploited here. The evaluation of Stokes' and Poisson's integrals has been efficiently achieved as convolutions using 2-D Fast Fourier Transforms in planar and spherical approximation (Blaha et al., 1996; Forsberg and Sideris, 1993; Schwarz et al., 1990; Sideris and Li, 1993; Sideris and She, 1995; Tziavos, 1996). This has the advantage, compared to numerical integration, of being able to process large amounts of gridded data in a short period of time. The downward continuation can be performed by inverting or deconvolving the process in the frequency domain (Zhang, 1995). Still, there are a couple of drawbacks. For example, data need to be uniformly gridded at the same satellite altitude. In the case of planar approximation, errors increase with the area, while with the spherical approximation, errors due to the convergence of meridians increase with area along meridians. Nonetheless, this effect is diminished with the multiband spherical approximation (Forsberg and Sideris, 1993). A method that avoids these errors for upward continuation is numerical integration combined with 1-D

FFT along parallels (Haagmans et al., 1993). The evaluation of integrals with this method is as exact as with numerical integration. Thus, in principle, we should be able to do 2-D inversion or downward continuation avoiding inversion of large systems and getting the same accuracy as direct integral inversion. Obviously, this method also allows the processing of more data, being at the same time more time-efficient than direct conventional inversion in the space domain. A kind of deconvolution can also be applied involving a matrix the same size as in numerical integration but, with a block diagonal structure, which makes it much easier to invert.

Deconvolution is an efficient way of performing inversion. The solution is obtained by simple division in the frequency domain or by fast deconvolution algorithms. The technique has been successfully applied in some sciences like seismology, spectroscopy, and imaging; see, for instance, (Bertero and Boccacci, 1996) and (Lagendijk, 1997). One problem associated with deconvolutions is the presence of non-physical data produced by the non-periodic nature of real data (Jansson, 1998). Some iteration methods like the Projected Landweber method manage to get around this problem and have been applied with some success in the mentioned sciences. This approach could be employed for inversion of integrals used in geodesy like Poisson's integral, allowing for processing of more data than regular inversion methods.

CHAPTER 2

GRACE INDIRECT OBSERVABLES

In the previous chapter, we treated equations relating GRACE measurements $\dot{\rho}_{12}$ and $\ddot{\rho}_{12}$ with potential differences (*DT*) and gravity disturbance differences (*DGD*), see equations (1.12), (1.19) and (1.20). These equations involve position, velocity and acceleration quantities. Therefore, their errors will affect the precision of the observables. In this chapter we do some error analysis in the determination of *DT* and *DGD* according to equations (1.14) and (1.31).

2.1 Potential Differences

2.1.1 Effect of Position Errors

From equation (1.19), we can see that absolute and relative position elements are involved in the determination of *DT*. All the terms related to the rotational gravitation include either an absolute or a relative positional element. For uncertainties in absolute positional elements we can write the following error equation, assuming $\delta x_1 = \delta y_2$

$$\delta DT(\delta x) = -\omega_e(\dot{x}_{12} - \dot{y}_{12})\delta x \tag{2.1}$$

For relative position errors we have, assuming $\delta x_{12} = \delta y_{12}$

$$\delta DT(\delta x_{12}) = -\omega_e(\dot{x}_1 - \dot{y}_1)\delta x_{12} \tag{2.2}$$

In order to evaluate these formulas, we consider the following values; $\omega_e = 0.00007292115$, $\dot{x}_1 = \dot{y}_1 = 7500$ m/s, $\dot{x}_{12} = \dot{y}_{12} =$ 200 m/s. With these values in the previous equations we obtain that, one meter of error in absolute satellite position will produce about 0.01 m^2/s^2 of error on *DT*. The same error will be obtained by 1 cm of error on relative position. These results are in agreement with results in (Jekeli, 1998a).

The presence of the reference or normal field on the equation for *DT* introduces the registration error, which seems to impose a mayor restriction for position related errors. This registration error can be estimated considering the gradient of the potential, that is, the gravitational acceleration. If we take its largest component, which along the radial

direction at GRACE altitude is about 8.7 m/s^2, then a 1 cm radial orbit error will cause about 0.1 m^2/s^2 error, which is larger than errors produced by 1cm of error in relative position. Nevertheless, if the orbits of both satellites are highly correlated, we could even use the gradient of the potential differences. Employing the EGM96 geopotential model, we estimated this gradient at 400 km altitude. The estimated values of the gradient were about 0.001 m/s^2 in the along track direction and about 0.0001 m/s^2 in the radial direction. Thus, a 10 cm orbit error will cause about 0.01 m^2/s^2 error.

2.1.2 Effect of Velocity Errors

In the computation of *DT* with equation (1.19) and (1.20), velocity quantities are present in all the terms except in the reference field term. Thus, some error analysis is also required here for both, absolute and relative satellite velocities. For this purpose, we differentiate equation (1.19) obtaining

$$\begin{aligned}\delta DT = {} & \dot{x}_{12}\delta\dot{x}_1 + \dot{y}_{12}\delta\dot{y}_1 + \dot{z}_{12}\delta\dot{z}_1 + \dot{x}_1\delta\dot{x}_{12} + \dot{y}_1\delta\dot{y}_{12} + \dot{z}_1\delta\dot{z}_{12} + \dot{x}_{12}\delta\dot{x}_{12} + \dot{y}_{12}\delta\dot{y}_{12} + \dot{z}_{12}\delta\dot{z}_{12} \\ & + \omega_e\left[-y_{12}\delta\dot{x}_1 + x_{12}\delta\dot{y}_1 - (y_1 + y_{12})\delta\dot{x}_{12} + (x_1 + x_{12})\delta\dot{y}_{12}\right]\end{aligned} \tag{2.3}$$

Grouping common terms with respect to absolute and relative velocities we can write

$$\begin{aligned}\delta DT = {} & \left[\dot{x}_{12} - \omega_e y_{12} \quad \dot{y}_{12} + \omega_e x_{12} \quad \dot{z}_{12}\right]\left[\delta\dot{x}_1 \quad \delta\dot{y}_1 \quad \delta\dot{z}_1\right]^{\mathrm{T}} + \\ & \left[\dot{x}_1 + \dot{x}_{12} - \omega_e(y_1 + y_{12}) \quad \dot{y}_1 + \dot{y}_{12} + \omega_e(x_1 + x_{12}) \quad \dot{z}_1 + \dot{z}_{12}\right]\left[\delta\dot{x}_{12} \quad \delta\dot{y}_{12} \quad \delta\dot{z}_{12}\right]^{\mathrm{T}}\end{aligned} \tag{2.4}$$

which is like considering the velocity vector of satellite one and the vector of velocity differences as measured quantities. Assuming equal errors for components of $\dot{\boldsymbol{X}}_1$ and for $\dot{\boldsymbol{X}}_{12}$. That is

$$\delta v_1 = \delta\dot{x}_1 = \delta\dot{y}_1 = \delta\dot{z}_1,\ \ \delta v_{12} = \delta\dot{x}_{12} = \delta\dot{y}_{12} = \delta\dot{z}_{12} \tag{2.5}$$

and substituting into (2.4)

$$\begin{aligned}\delta DT(\delta v_1) &= \left[(\dot{x}_{12} - \omega_e y_{12})^2 + (\dot{y}_{12} + \omega_e x_{12})^2 + (\dot{z}_{12})^2\right]^{\frac{1}{2}}\delta v_1 \\ \delta DT(\delta v_{12}) &= \left[\left(\dot{x}_1 + \dot{x}_{12} - \omega_e(y_1 + y_{12})\right)^2 + \left(\dot{y}_1 + \dot{y}_{12} + \omega_e(x_1 + x_{12})\right)^2 + (\dot{z}_1 + \dot{z}_{12})^2\right]^{\frac{1}{2}}\delta v_{12}\end{aligned} \tag{2.6}$$

These equations give a relationship between *DT* errors and absolute and relative position and relative errors. Further assuming, for error analysis purposes, that $\dot{x}_1 = \dot{y}_1 = \dot{z}_1 = v_1$,

$\dot{x}_{12} = \dot{y}_{12} = \dot{z}_{12} = v_{12}$, $y_1 = x_1 = p$, $y_{12} = x_{12} = p_{12}$ we obtain a more simple set of equations

$$\begin{aligned} \delta DT(\delta v_1) &= \left[2(\omega_e p_{12})^2 + 3(v_{12})^2\right]^{\frac{1}{2}} \delta v_1 \\ \delta DT(\delta v_{12}) &= \left[2\left(\omega_e p\right)^2 + 3v^2\right]^{\frac{1}{2}} \delta v_{12} \end{aligned} \tag{2.7}$$

We now numerically estimate the effects of errors in the velocity vectors $\dot{\mathbf{X}}_1$ and in $\dot{\mathbf{X}}_{12}$ according to equation (2.7). We assume for the involved quantities the following nominal values

$$\begin{aligned} &\omega_e = 0.00007292115,\ v_1 = 7500 \text{ m/s},\ v_{12} = 200 \text{ m/s}, \\ &p = 6771\ km,\ p_{12} = 200\ km \end{aligned} \tag{2.8}$$

Using these numerical values we find that for a *DT* error of 0.01 m^2/s^2 we require errors of less that $1 \cdot 10^{-4}$ m/s in absolute velocity and $1 \cdot 10^{-5}$ m/s in relative velocity. Previous analyses have yielded similar results, see (Jekeli, 1998a). This means that for this situation errors coming from $\dot{\boldsymbol{X}}_1$ produce errors on *DT* about one order of magnitude smaller than errors coming from $\dot{\boldsymbol{X}}_{12}$. That is, the accuracy for velocity differences will be more demanding than for absolute velocity components.

This shows that the accuracy required for the vector of velocity differences $\dot{\boldsymbol{X}}_{12}$ is at least one order of magnitude higher than for the velocity vector $\dot{\boldsymbol{X}}_1$. The velocity vector $\dot{\boldsymbol{X}}_{12}$ can be obtained using GPS differential positioning, with respect to both GRACE satellites. However, the range rate $\dot{\rho}_{12}$, which can be obtained with better precision, can also be incorporated as a measurement to improve the accuracy of $\dot{\boldsymbol{X}}_{12}$. Then, the errors of the relative velocity measurement produced from both systems, GRACE and GPS, will have different effect on the estimated vector $\dot{\boldsymbol{X}}_{12}$. Let's do some analysis on the effect of errors in $\dot{\rho}_{12}$. Assuming the orbits of both GRACE satellites to be polar so the velocity vectors can be represented by two perpendicular components in the orbital plane say, along the *Z*-axis and along a perpendicular direction *P*. Then we can represent the absolute and relative velocity vectors as

$$\dot{\boldsymbol{X}}_{\boldsymbol{1}} = \begin{bmatrix} \dot{p}_1 & \dot{z}_1 \end{bmatrix}^T,\ \dot{\boldsymbol{X}}_{\boldsymbol{2}} = \begin{bmatrix} \dot{p}_2 & \dot{z}_2 \end{bmatrix}^T,\ \dot{\boldsymbol{X}}_{\boldsymbol{12}} = \begin{bmatrix} \dot{p}_{12} & \dot{z}_{12} \end{bmatrix}^T \tag{2.9}$$

Now, using equation (2.4) and approximating for simplicity, $p \simeq x$, $\dot{p} \simeq \dot{x}$, $y \simeq 0$, $\dot{y} \simeq 0$, then the terms containing ω_e will be equal to zero. Thus, we can write the following error equation

$$\delta DT(\delta \dot{p}_{12}, \delta \dot{z}_{12}) = \left[\left(\dot{p}_1 + \dot{p}_{12} \right)^2 (\delta \dot{p}_{12})^2 + (\dot{z}_1 + \dot{z}_{12})^2 (\delta \dot{z}_{12})^2 \right]^{\frac{1}{2}} \tag{2.10}$$

On the other hand, the range rate $\dot{\rho}_{12}$ can be approximated by

$$\dot{\rho}_{12}^2 \approx \dot{z}_{12}^2 + \dot{p}_{12}^2 \tag{2.11}$$

Since $\dot{z}_{12}$ and $\dot{p}_{12}$ are perpendicular each other, we can also write

$$\dot{\rho}_{12} = \cos(\phi)\dot{z}_{12} = \sin(\phi)\dot{p}_{12} \tag{2.12}$$

where ϕ is the latitude. Applying error propagation to equation (2.12) and using equation (2.10) we obtain the following error equation

$$\delta DT(\delta \dot{\rho}_{12}) \approx \left[\left(\dot{p}_1 + \dot{p}_{12} \right)^2 (\sin(\phi)\delta \dot{\rho}_{12})^2 + (\dot{z}_1 + \dot{z}_{12})^2 (\cos(\phi)\delta \dot{\rho}_{12})^2 \right]^{\frac{1}{2}} \tag{2.13}$$

using the following approximations, $\dot{p}_1 = \dot{z}_1 = v$ we arrive to the simple error equation

$$\delta DT(\delta \dot{\rho}_{12}) \approx v \delta \dot{\rho}_{12} \tag{2.14}$$

For GRACE mission an error 10^{-6} in $\dot{\rho}_{12}$ will produce about 0.01 m^2/s^2 of error in *DT*. This level of error propagation is similar to the one obtained for v_{12} in equation (2.7). Since there is no presence of ω_e, it is evident from equations (2.10) and (2.13) that for a polar orbit the rotational effect on the potential does not impose any additional precision requirement for $\dot{\rho}_{12}$. Since GRACE orbit is near polar, we could expect a relatively small effect of the rotational potential in the error requirements for $\dot{\rho}_{12}$.

The effect of non-gravitational forces on the potential differences, see equations (2.19), (2.21) and (2.22) involves also the presence of velocity vectors. Thus, velocity errors will have additional effects on potential difference errors, due to the consideration of this effect. However, they can be expected to be smaller than the velocity errors effect obtained so far. From equation (2.22) we can obtain, using previous velocity values assumptions, the following equation

$$V_{12,a} = 20\,000 \left| (F_{2,x} + F_{2,y} + F_{2,z}) v_{12} - (F_{12,x} + F_{12,y} + F_{12,z}) v \right| \tag{2.15}$$

Then, applying error propagation we obtain the error equation

$$\delta V_{12,a}(\delta v_{12}, \delta v) = 20\,000 \left[(F_{2,x} + F_{2,y} + F_{2,z})^2 (\delta v_{12})^2 - (F_{12,x} + F_{12,y} + F_{12,z})^2 \delta v^2 \right]^{1/2} \tag{2.16}$$

Assigning $F_{12} = |\boldsymbol{F}_{12}|$, $F = |\mathbf{F}|$ we get the approximation

$$\delta V_{12,a}(\delta v_{12}, \delta v) \simeq 20\,000\left[F^2(\delta v_{12})^2 + F_{12}^2(\delta v)^2\right]^{1/2} \tag{2.17}$$

or considering the effect of absolute and relative velocity errors separately we have

$$\begin{aligned} \delta V_{12,a}(\delta v) &\simeq 20\,000 F_{12}\delta v \\ \delta V_{12,a}(\delta v_{12}) &\simeq 20\,000 F \delta v_{12} \end{aligned} \tag{2.18}$$

The two main non-gravitational forces are the atmospheric drag and the solar radiation pressure. For GRACE orbit altitude these forces can have values up to 10^{-3} m/s^2 and 10^{-5} m/s^2 respectively, see (Seeber, 1993; Kim, 2000). With these values and using equation (2.18) we find that absolute and relative velocity errors of 10^{-4} and 10^{-5} m/s, respectively, will produce potential errors smaller than 0.001 m^2/s^2.

2.1.3 Effect of Accelerometer Errors

GRACE satellites will have on board accelerometers to measure accurately non-conservative forces including atmospheric drag, solar radiation pressure, earth radiation pressure and thermal forces. From equation (1.15) the effect of these measured forced on the gravitational potential can be written as

$$V_a = -\int_{t_0}^{t} \boldsymbol{F} \cdot \dot{\mathbf{X}} dt \tag{2.19}$$

We define the vector representing the specific forces for both satellites as $\mathbf{F_1}$, $\mathbf{F_2}$ for trailing and leading satellites, respectively, and expanding the inner product of equation (2.19), we can obtain

$$\begin{aligned} V_{12,a} &= \int_{t_0}^{t} \left(\boldsymbol{F_1} \cdot \dot{\mathbf{X}}_1 - \boldsymbol{F_2} \cdot \dot{\mathbf{X}}_2\right) dt \qquad = \int_{t_0}^{t} \left(\boldsymbol{F_1} \cdot \dot{\mathbf{X}}_1 - \boldsymbol{F_2} \cdot \left[\dot{\mathbf{X}}_1 + \dot{\mathbf{X}}_{12}\right]\right) dt \\ &= \int_{t_0}^{t} \left[\left(\boldsymbol{F_1} - \boldsymbol{F_2}\right) \cdot \dot{\mathbf{X}}_1 + \boldsymbol{F_2} \cdot \dot{\mathbf{X}}_{12}\right] dt = \int_{t_0}^{t} \left[\boldsymbol{F_2} \cdot \dot{\mathbf{X}}_{12} - \boldsymbol{F_{12}} \cdot \dot{\mathbf{X}}_1\right] dt \end{aligned} \tag{2.20}$$

Expanding the dot products

$$V_{12,a} = \int_{t_0}^{t} \left[F_{2,x}\dot{x}_{12} + F_{2,y}\dot{y}_{12} + F_{2,z}\dot{z}_{12} - F_{12,x}\dot{x}_1 - F_{12,y}\dot{y}_1 - F_{12,x}\dot{z}_1 \right] dt \tag{2.21}$$

The integral in this equation is difficult to evaluate since there are no analytic expressions for the force and velocity vectors involved. In order to be able to perform error estimation, we'll assume these quantities to be constant. The expected accuracy of acceleration measurements is 10^{-10} m/s^2 over 0.1 to 0.00005 Hz (Stanton, 2000). This would correspond to a maximum period of 20 000 seconds. Evaluating the integral for this period so we can estimate the maximum error produced, thus

$$\begin{aligned} V_{12,a} &= 20\,000 \left| F_{2,x}\dot{x}_{12} + F_{2,y}\dot{y}_{12} + F_{2,z}\dot{z}_{12} - F_{12,x}\dot{x}_1 - F_{12,y}\dot{y}_1 - F_{12,x}\dot{z}_1 \right| \\ V_{12,a} &= 20\,000 \left| (\dot{x}_{12} + \dot{y}_{12} + \dot{z}_{12})F_2 - (\dot{x}_1 + \dot{y}_1 + \dot{z}_1)F_{12} \right| \end{aligned} \tag{2.22}$$

where we have assumed $F = F_{2,x} = F_{2,y} = F_{2,z}$, $F_{12} = F_{12,x} = F_{12,y} = F_{12,z}$. Then, applying error propagation we obtain the error equation

$$\delta V_{12,a}(\delta F, \delta F_{12}) = 20\,000 \left[\left(\dot{x}_{12} + \dot{y}_{12} + \dot{z}_{12}\right)^2 \delta F^2 + \left(\dot{x}_1 + \dot{y}_1 + \dot{z}_1\right)^2 \delta F_{12}^2 \right]^{1/2} \tag{2.23}$$

Assigning $v_{12} = \left|\dot{\mathbf{X}}_{12}\right|$, $v = \left|\dot{\mathbf{X}}_1\right|$ and $F = F_2$ we get the approximation

$$\delta V_{12,a}(\delta F, \delta F_{12}) = 20\,000 \left[v_{12}^2 \delta F^2 + v^2 \delta F_{12}^2 \right]^{1/2} \tag{2.24}$$

or considering the effect of absolute and relative acceleration errors separately we have

$$\begin{aligned} \delta V_{12,a}(\delta F) &= 20\,000 v_{12} \delta F \\ \delta V_{12,a}(\delta F_{12}) &= 20\,000 v \delta F_{12} \end{aligned} \tag{2.25}$$

Assuming $v_{12} = 200$ m/s and $v = 7500$ m/s for the velocity quantities, we obtain that an error of about 0.01 m^2/s^2 in *DT*, will be produced by an error of 10^{-8} m/s^2 in absolute acceleration and by an error of 10^{-10} m/s^2 in relative acceleration.

2.2 Gravity Disturbance Differences

2.2.1 Effects of Position Errors

In equation (1.12), which gives the expression for *DGD*, the presence of position related quantities are on the four last terms of the right hand side. For the second or centrifugal term (see also equation (1.11)), the effects of errors in $1/\rho_{12}$ will be very small due to the

large magnitude of ρ_{12}. Let's now analyze position errors from the terms $\mathbf{e}_{12}^T\mathbf{a_{12}}$ and $\mathbf{e}_{12}^T\boldsymbol{\gamma}_{\mathbf{12}}$. After differentiating equation (1.12) with respect to $\mathbf{e}_{12}$ we obtain

$$\delta DGD(\delta \mathbf{e}_{12}) = -\delta \mathbf{e}_{12}^T(\mathbf{a_{12}} + \boldsymbol{\gamma}_{12}) \tag{2.26}$$

but $\delta \mathbf{e}_{12}$ can be expressed in terms of relative position errors as follows

$$\begin{aligned} \delta \mathbf{e}_{12} &= \frac{\delta \mathbf{X}_{12}}{\rho_{12}} - \frac{\mathbf{X}_{12}}{\rho_{12}^2}\delta\rho_{12} \\ &\simeq \frac{\delta \mathbf{X}_{12}}{\rho_{12}} \end{aligned} \tag{2.27}$$

this is assuming $\delta\rho_{12}$ to be much smaller than $\delta \boldsymbol{X}_{\boldsymbol{12}}$. Then, further assuming $\gamma_{12} \approx |\boldsymbol{\gamma}_{12}|$, $a_{12} = |\mathbf{a_{12}}|$, $x_{12} = |\mathbf{X_{12}}|$ and substituting into equation (2.26) we arrive at the following simplified error equation

$$\delta DGD(\delta x_{12}) \simeq \frac{a_{12} + \gamma_{12}}{\rho_{12}}\delta x_{12} \tag{2.28}$$

For a meter of relative position error and assuming a_{12} = 0.01 m/s^2 and γ_{12} = 0.01 m/s^2 we would obtain an acceleration error of 0.01 mgal. This value is consistent with previous analyses; see Jekeli (1998a).

Finally for the last term in equation (1.12), the positional error is the registration error in computing the part representing the reference field of *DGD*. The gravitational gradient was estimated at orbit altitude using the EGM96 geopotential model. The estimated value for the radial component was 0.26 mgal/m, which means that for 10-cm radial orbit error the registration error would be about 0.03 mgal. Nevertheless, as considering for potential differences, if the orbits of both satellites are highly correlated, we could even use the gradient of the gravity difference. Using the EGM96 geopotential model, we estimated this gradient at 400 km altitude. The estimated values were about 0.0005 mgal/m in the along track direction and about 0.00001 mgal/m in the radial direction. With these gradient values a 10 m orbit error will cause about 0.01 mgal error.

2.2.2 Effect of Velocity Errors

Velocity quantities are only present in the centrifugal term of equation (1.14), and they are located in the plane perpendicular to the line-of-sight direction. After taking differentials of this equation, we obtain the following error equation

$$\delta\Phi_{12} \approx \frac{2}{\rho_{12}}\left(\dot{y}^{o}_{12} + \dot{z}^{o}_{12}\right)\delta\dot{x}_{12} - \frac{1}{\rho_{12}}\Phi_{12}\delta\rho_{12} \tag{2.29}$$

In this expression we have errors in the centrifugal term expressed as of range and velocity errors. This equation was evaluated considering a Keplerian orbit and assuming an inter-satellite separation of 200 km at 400 km altitude; velocity differences are then used in the potential difference error analysis. Figure 2.1 shows the relationships.

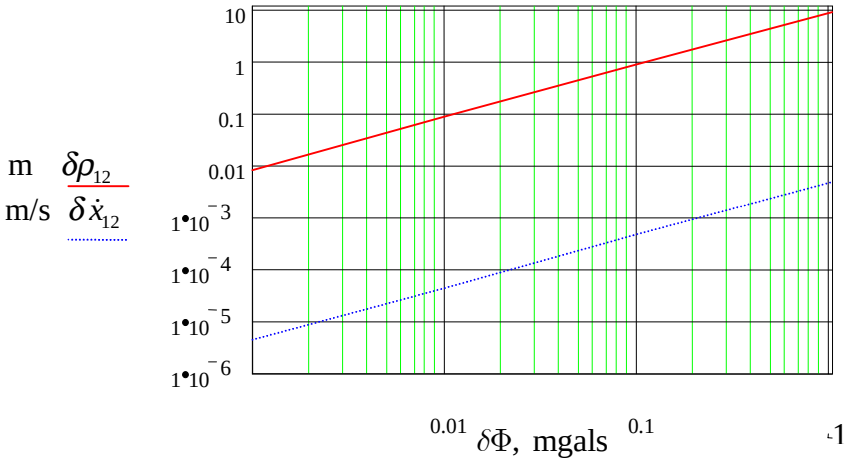

Figure 2.1: Error of the centrifugal acceleration term in terms of range errors and velocity errors orthogonal to the LOS.

We can see from the above figure that in order to obtain a 0.01 mgal error, the velocity difference errors need to be smaller that $1\cdot10^{-4}$ m/s ; whereas, range errors, 0.1 m will yield that acceleration error.

2.2.3 Effect of Acceleration Errors

The error equation is, from equation (1.12)

$$\begin{aligned}\delta DGD(\delta a_{12}) &\approx \left|\mathbf{e_{12}}\right|\delta a_{12} \\ &\approx \delta a_{12}\end{aligned} \tag{2.30}$$

We can see from this equation that acceleration errors coming from the accelerometer measurements will be relatively small since the total accelerometer errors will be about $1\cdot10^{-5}$ mgal and we can expect that the errors in computing its components along the LOS, as is required in equation (1.12), to be at most of the same order of the accelerometer error.

Table (2.1) summarizes position, velocity and acceleration error requirements to obtain potential differences and gravity disturbance differences with $0.01\,\mathrm{m}^2/\mathrm{s}^2$ and 0.01 mgal accuracy, respectively.

Observable Error	Error Requirements					
	Position m		Velocity m/s		Acceleration mgal	
	Abs	Rel	Abs	Rel	Abs	Rel
DT (0.01 $\mathrm{m}^2/\mathrm{s}^2$)	0.1	0.01	10^{-4}	10^{-5}	0.001	10^{-5}
DGD (0.01 mgal)	10	0.1	-----	10^{-5}	0.01	----

Table 2.1: Error requirements on position, velocity and acceleration to obtain potential and gravity disturbance differences with an accuracy of 0.01 $\mathrm{m}^2/\mathrm{s}^2$ and 00.1 mgal respectively.

CHAPTER 3

DISTURBING POTENTIAL DETERMINATION

The purpose of this chapter, is to derive some relationships between the in-situ GRACE observables *DT* and *DGD*, as obtained from equations (1.12) and (1.20), and the disturbing potential and gravity anomalies values at the Earth's surface, considered here to be a sphere with mean terrestrial radius. The sought-after relationships can be established by using integrals like those of Poisson and Stokes as seen below.

3.1 From Potential Differences

3.1.1 Using Poisson's Integral

Dirichlet's problem is one of the main boundary value problems of physical geodesy. This problem consists of determining a harmonic function in space given its values on a boundary surface. In spherical approximation Poisson's integral yields the solution for the space exterior to the sphere. According to this integral, if we have a potential function *V* given over a sphere of radius *R*, then the potential value in space for a point with spherical coordinates (r,ϕ,λ) is given by (Heiskanen and Moritz, 1967)

$$V_P(r,\phi,\lambda)=\frac{R(r^2-R^2)}{4\pi}\int_{\lambda'=0}^{2\pi}\int_{\phi'=0}^{\pi}\frac{V(R,\phi',\lambda')}{\rho(r,R,\psi)^3}\cos\phi' d\lambda' d\phi' \tag{3.1}$$

With:

$$\begin{aligned}&\rho(r,R,\psi)^2=r^2+R^2-2rR\cos(\psi)\\&\cos(\psi)=\cos(\phi)\cos(\phi')\cos(\lambda-\lambda')+\sin(\phi)\sin(\phi')\end{aligned} \tag{3.2}$$

Where:

V_P	Potential value at point p at radius *r*
R	Radius of a spherical earth
ϕ,λ	Latitude and longitude
ρ	Geometric distance between the point *P* and the integration point

ψ Angle between the point *P* and the integration point at the Earth's center.

Equation (3.1) can also be written as

$$V_P = \iint_{\sigma} K(r,\psi_{PQ}) V_Q d\sigma \tag{3.3}$$

where $K\left(r,\psi_{PQ}\right)$ represents the Poisson kernel and $d\sigma$ is a surface element. They are given by

$$K(r,\psi_{PQ}) = \frac{R(r^2 - R^2)}{4\pi\rho(r,R,\psi_{PQ})^3},\ d\sigma = \cos\phi_Q d\lambda d\phi \tag{3.4}$$

Poisson's integral is defined for harmonic functions. Therefore, it can be used for the disturbing potential *T*, which is a harmonic function. Then, from equation (3.3) we can write

$$T_p = \iint_{\sigma} K(r,\psi_{PQ}) T_Q d\sigma \tag{3.5}$$

This integral gives a simple relationship between the disturbing potential at the Earth's surface (approximated by a sphere) and its value at a point in space, given that $r \geq R$.

3.1.2 Computation of the Disturbing Potential

The potential measurements obtained from GRACE observables at orbit altitude are not *T* but *DT*. Therefore, we still need to establish the relationship between *DT* and *T* at the Earth's surface as follows. At a given epoch, the potential difference related to the points of location of both satellites (assuming $r_{p1} = r_{p2} = r$) is given by

$$DT_{P1,P2} = T_{P2}(r,\phi_{P2},\lambda_{P2}) - T_{p1}(r,\phi_{P1},\lambda_{P1}) \tag{3.6}$$

Applying equation (3.5) to (3.6) we obtain

$$DT_{P1,P2} = \iint_{\sigma} K(r,\psi_{P2,Q})T_Q d\sigma - \iint_{\sigma} K(r,\psi_{P1,Q})T_Q d\sigma$$
$$= \iint_{\sigma} \left[K(r,\psi_{P2,Q}) - K(r,\psi_{P1,Q}) \right] T_Q d\sigma \tag{3.7}$$

or

$$DT_{P1,P2} = \iint_{\sigma} \Delta K_{P1,P2,Q} T_Q d\sigma \tag{3.8}$$

Since the measurements are values of *DT*, the solution for *T* has to be obtained by integral inversion. In practice this presents some problems. Data are given in discrete form and often over a limited region introducing discretization and truncation errors. Moreover, due to the gravity field attenuation with altitude, the inversion process involved turns out to be ill-posed, which means that measurement and model errors will amplify in the inversion. Inversion methods for the matrix representation of this type of problems are treated in chapter 4.

Similar to equation (3.5), equation (3.8) relates the differences *DT* located also in space with *T* at the Earth's surface. It happens that we are trying to obtain the function itself from differences. Common sense tells us that this is not possible to do without some bias in the solution. One possible solution to this problem is to remove from the measurements components (i.e. a reference field), whose wavelengths are larger than the dimensions of the integration area σ. The removal of the reference field implies that it would not be present in the estimates of *T*. That is, they contain only the frequencies present in the residual field.

3.2 From Gravity Disturbance Differences

As seen in previous chapters, another in-situ measurement that can be obtained from GRACE is the difference of gravity disturbances *DGD*. By taking the gradient Poisson's integral, this observable is related to the disturbing potential at the Earth's surface in a similar way as is *DT* (see equation (3.8)). Furthermore, following a similar procedure with Stokes' integral, gravity anomalies at the Earth's surface can also be related to *DGD*. These relationships will be demonstrated in this section.

3.2.1 Using Poisson's Integral

The components $\delta_r, \delta_\phi, \delta_\lambda$ of the gravity disturbance vector $\delta\mathbf{g}$ along the coordinates lines of a spherical coordinate system r, ϕ, λ can be expressed in terms of the disturbing

potential. The derivation is similar as the one made in Heiskanen and Moritz (1967) between gravity anomalies and the disturbing potential. The components of the gravity disturbance vector are the partial derivative of the disturbing potential, which in spherical coordinates are

$$\delta_r = \frac{\partial T}{\partial r},\ \delta_\phi = \frac{1}{r}\frac{\partial T}{\partial \phi},\ \delta_\lambda = \frac{1}{r\cos\phi}\frac{\partial T}{\partial \lambda} \tag{3.9}$$

Here we will only concentrate on the components δ_ϕ and δ_λ since, the direction of the component δ_r is almost perpendicular the line of sight between both GRACE satellites. Substituting equation (3.5) into equation (3.9), we can compute at a point *P* in space the components δ_ϕ and δ_λ from disturbing potential values at the Earth's surface:

$$\begin{aligned}
\delta_{\phi,P} &= \frac{1}{r}\iint_\sigma T_Q \frac{\partial K(r,\psi_{PQ})}{\partial \phi} d\sigma \\
\delta_{\lambda,P} &= \frac{1}{r\cos\phi_P}\iint_\sigma T_Q \frac{\partial K(r,\psi_{PQ})}{\partial \lambda} d\sigma
\end{aligned} \tag{3.10}$$

The partial derivatives in equation (3.10) are given by

$$\frac{\partial K(r,\psi)}{\partial \phi} = \frac{\partial K(r,\psi)}{\partial \psi}\frac{\partial \psi}{\partial \phi},\ \frac{\partial K(r,\psi)}{\partial \lambda} = \frac{\partial K(r,\psi)}{\partial \psi}\frac{\partial \psi}{\partial \lambda} \tag{3.11}$$

Then, using equations (3.2) and (3.13)

$$\frac{\partial \psi}{\partial \phi} = -\cos\alpha,\ \ \frac{\partial \psi}{\partial \lambda} = -\cos\phi\sin\alpha \tag{3.12}$$

where α is the azimuth and is given by

$$\tan\alpha = \frac{\cos\phi'\sin(\lambda' - \lambda)}{\cos\phi\sin\phi' - \sin\phi\cos\phi'\cos(\lambda - \lambda')} \tag{3.13}$$

Using equations (3.12) and (3.13) with $\phi' = \phi_Q,\ \lambda' = \lambda_Q$ equation (3.10) becomes

$$\delta_{\phi,P} = -\frac{1}{r}\iint_{\sigma} T_Q \frac{\partial K(r,\psi_{PQ})}{\partial \psi}\cos\alpha_{PQ}\, d\sigma$$
$$\delta_{\lambda,P} = -\frac{1}{r}\iint_{\sigma} T_Q \frac{\partial K(r,\psi_{PQ})}{\partial \psi}\sin\alpha_{PQ}\, d\sigma \qquad (3.14)$$

where the partial derivative is given by

$$\frac{\partial K(r,\psi_{PQ})}{\partial \psi} = \frac{3rR^2(r^2-R^2)\sin\psi_{PQ}}{4\pi\rho_{PQ}^5} \qquad (3.15)$$

Substituting this into (3.14) we obtain the integrals that relate the gravity disturbance components δ_ϕ and δ_λ to the disturbing potential at the Earth's surface (ibid).

$$\delta_{\phi,P} = \frac{3R^2(r^2-R^2)}{4\pi}\iint_{\sigma} T_Q \frac{\sin\psi_{PQ}}{\rho_{PQ}^5}\cos\alpha_{PQ}\, d\sigma$$
$$\delta_{\lambda,P} = \frac{3R^2(r^2-R^2)}{4\pi}\iint_{\sigma} T_Q \frac{\sin\psi_{PQ}}{\rho_{PQ}^5}\sin\alpha_{PQ}\, d\sigma \qquad (3.16)$$

In chapter 1 we derived an expression for *DGD*, which is the difference of components δ_ε along the LOS direction with azimuth α'. This component can be obtained from the components δ_ϕ and δ_λ and, therefore, in terms of *T* as follows:

$$\delta_{\varepsilon,P} = \delta_{\phi,P}\cos\alpha' + \delta_{\lambda,P}\sin\alpha' = \iint_{\sigma} H(r,\psi_{PQ},\alpha_{PQ})T_Q\, d\sigma \qquad (3.17)$$

with

$$H(\psi_{PQ},\alpha_{PQ}) = \frac{R^2(r^2-R^2)}{4\pi}\frac{\sin\psi_{PQ}}{\rho_{PQ}^5}\left[\cos\alpha_{PQ}\cos\alpha' + \sin\alpha_{PQ}\sin\alpha'\right]$$
$$= \frac{R^2(r^2-R^2)}{4\pi}\frac{\sin\psi_{PQ}}{\rho_{PQ}^5}\cos(\alpha_{PQ}-\alpha') \qquad (3.18)$$

Equation (3.17) is a general expression for any component of the gravity disturbance vector perpendicular to the radial direction.

3.2.2 Computation of the Disturbing Potential

Similarly to potential differences, we only are able to obtain differences of the gravity disturbance as shown by equation (1.12). To relate them to the disturbing potential at the Earth's surface, we proceed as with the potential differences in the previous section. Then, similarly to *DT* with equation (3.6) (also assuming that $r_{p1} = r_{p2} = r$) , *DGD* can be given by

$$DGD_{P1P2} = \delta_{\varepsilon,P2}(r_{P2}, \phi_{P2}, \lambda_{P2}) - \delta_{\varepsilon,p1}(r_{P1}, \phi_{P1}, \lambda_{P1}) \tag{3.19}$$

This equation, together with equation (3.17) yields

$$\begin{aligned} DGD_{P1P2} &= \iint_{\sigma} H(r, \psi_{P2,Q}, \alpha_{P2Q}) T_Q d\sigma - \iint_{\sigma} H(r, \psi_{P1,Q}, \alpha_{P1Q}) T_Q d\sigma \\ &= \iint_{\sigma} \left[H(r, \psi_{P2,Q}, \alpha_{P2Q}) - H(r, \psi_{P1,Q}, \alpha_{P1Q}) \right] T_Q d\sigma \end{aligned} \tag{3.20}$$

Then, similar to equation (3.8)

$$DGD_{P1P2} = \iint_{\sigma} \Delta H_{QP1P2} T_Q d\sigma \tag{3.21}$$

The disturbing potential is obtained from the gravity disturbance differences also by inversion. This time, the differences correspond to a different function.

3.2.3 Using Stokes' Integral

It is well known that Stokes' integral relates the disturbing potential to gravity anomalies. According to Heiskanen and Moritz (1967).

$$T_p = T(r, \phi, \lambda) = \frac{R}{4\pi} \iint_{\sigma} S(r, \psi) \Delta g d\sigma \tag{3.22}$$

where $S(r, \psi)$ is the so-called Stokes' kernel.

Following the same procedure as in the previous section, one can arrive at expressions for δ_ϕ and δ_λ , but this time in terms of gravity anomalies

$$\delta_\phi = \frac{R}{4\pi\gamma}\iint_\sigma \Delta g \frac{\partial S(r,\psi)}{\partial \psi}\cos\alpha d\sigma$$
$$\delta_\lambda = \frac{R}{4\pi\gamma}\iint_\sigma \Delta g \frac{\partial S(r,\psi)}{\partial \psi}\sin\alpha d\sigma \qquad (3.23)$$

where the derivative with respect to ψ is given by (ibid)

$$\frac{\partial S}{\partial \psi} = \sin\psi\left[-\frac{2R^2 r}{\rho^3} - \frac{6R^2}{r\rho} + \frac{8R^2}{r^2} + \frac{3R^2}{r^2}\left(\frac{r - R\cos\psi - \rho}{\rho\sin^2\psi} + \ln\frac{r - R\cos\psi + \rho}{2r}\right)\right] \qquad (3.24)$$

Similar to equations (3.19) and (3.21) we arrive at an expression for the difference of gravity disturbances in terms of gravity anomalies. Thus, by integral inversion gravity anomalies can also be obtained from *DGD*. However, in order to obtain disturbing potential or geoid undulations we still need to evaluate Stokes' integral. We will not analyze the solution for gravity anomalies. Nevertheless, this approach could be used for calibration purposes in areas of good dense gravity anomalies measurements.

3.3 Evaluation of Integrals for Spherical Cap

For regional gravity mapping in geodesy, when evaluating integrals theoretically over the sphere, but practically restricted by measurements given only over a limited area the results will contain truncation errors. These errors will also be present in the solutions to the integral inversions. One common technique used to reduce this type of error is to subtract a reference field from the measurements. This reference field contains those frequencies of the signal with wavelengths longer than the dimension of the area ofintegration. This idea is based in the conventional Molodensky truncation theory in its modified form (see, for instance, Jekeli, 1981). According to this method we have, for instance, for Poisson's integral

$$T_p = \iint_{\sigma_c} K(\psi)(T - T')d\sigma + \sum_{n=2}^{n\max} t_n \qquad (3.25)$$

where nmax is the maximum degree of the reference field given in terms of a spherical harmonic series

$$T' = \sum_{n=2}^{n\max}\left(\frac{R}{r}\right)^{n+1} t_n \qquad (3.26)$$

By subtracting a low-degree reference field, the observed residual quantities are considered to be produced by the high frequency part of the gravitational field. Therefore, the measurements over a selected geographical region would be sufficient to estimate the residual disturbing potential within this region with satisfactory accuracy. This could also be helped by the attenuation of the integral’s kernel with increasing distance.

CHAPTER 4

THE DOWNWARD CONTINUATION (INVERSION) PROCESS

In previous chapters, we have established the relationship, through integration, of some GRACE observable like disturbing potential and gravity disturbance differences with the disturbing potential and gravity anomalies at the Earth's surface. In order to solve for either one of the last two quantities, an inversion of the corresponding integral is required according to equations like (3.8) and (3.21). Geodesists have used different techniques to evaluate integrals for data given over the sphere. The most popular methods, which will be treated in the following sections, are direct numerical integration, 2-D FFT and 1-D FFT combined with numerical integration. Each one of these methods will have a different inversion process associated with it.

The type of integrals that we need to invert (see equations (3.8) and (3.21)) involves the downward continuation from satellite's altitude to the Earth's surface. As mentioned in the introductory chapter, the downward continuation is known to be an ill-posed problem. Which means that small measurement errors will be greatly amplified with the downward continuation process. However, this problem can be overcome up to certain level by the use of regularization techniques. They will also be reviewed here.

4.1 Integral Evaluation Methods

4.1.1 Direct Numerical Integration

This method of integration is very precise. The data distribution is not required to be uniform. One problem is that, as the data increase in number, it quickly becomes computationally intensive. Let's consider the following integral over the sphere

$$g_{\mathrm{P}} = \iint_{\text{area}} K_{\mathrm{PQ}} f_{\mathrm{Q}} d\sigma_{\mathrm{Q}}, \quad d\sigma_Q = d\phi \cos\phi_Q d\lambda \tag{4.1}$$

Where

g_{P} is the evaluated quantity at point P.

f_{Q} is the integrated function at P.

K_{PQ} is the associated kernel function.

$d\sigma_Q$ is an element of surface area.

Integrals of this type are Poisson's, Stokes', and of course the ones in equations (3.8) and (3.21). We define by $\boldsymbol{A}$ the matrix representing the discretization of the integral in equation (4.1). Assuming a grid of evaluation and integration points with corresponding function values represented by vectors $\boldsymbol{g}$ and $\boldsymbol{f}$ respectively, we write symbolically

$$\boldsymbol{g} = \boldsymbol{A}\boldsymbol{f} \tag{4.2}$$

If, for instance, we have a regular grid with constant intervals $\Delta\phi, \Delta\lambda$ for the solution and measurement points, going from west to east and from south to north, an element of $\boldsymbol{A}$ will be given by

$$\boldsymbol{A}_{i,j} = K_{i,j}(\phi_i, \lambda_i, \phi_j, \lambda_j)\Delta\phi \cos\phi_j \Delta\lambda \tag{4.3}$$

with

$$\phi_i = \phi_1 + \left[\operatorname{int}\frac{i-1}{m}\right]\Delta\phi, \quad \lambda_i = \lambda_1 + \left[i - \left(\operatorname{int}\frac{i-1}{m}\right)m - 1\right]\Delta\lambda$$

$$\phi_j = \phi_1 + \left[\operatorname{int}\frac{j-1}{m}\right]\Delta\phi, \quad \lambda_j = \lambda_1 + \left[j - \left(\operatorname{int}\frac{j-1}{m}\right)m - 1\right]\Delta\lambda \tag{4.4}$$

$$i = 1, mn, \quad j = 1, mn$$

being ϕ_1, λ_1 the initial coordinates of the uniform grid, *m* the number of points along parallels and *n* the number of points along meridians.

4.1.2 Integral Evaluation with 2-D FFT

With the aid of FFT, the convolution theorem allows some integral to be evaluated in a much more efficient way than with direct numerical integration. By definition, a convolution between two functions *k(t)* and *f(t)* is given by

$$g(t) = (k * f)(t) = \int_{-\infty}^{\infty} k(t - t')\, f(t')\, dt' \tag{4.5}$$

This integral can be easily evaluated by using the convolution theorem (see Brigham, 1988): *The spectrum (Fourier) transform) of the convolution equals the product of the spectra (Fourier transforms) of the convolved functions.* That is, from

$$\hat{\mathrm{F}}(g(t)) = \hat{\mathrm{F}}((k * f)(t)) \tag{4.6}$$

we have, using their spectral representation in the frequency domain, whose variable is ω

$$G(\omega) = K(\omega)F(\omega) \tag{4.7}$$

with $\hat{\mathrm{F}}$ representing the Fourier Transform operator, G, *K*, *F* being the Fourier representation of the functions *g(t), k(t), f(t),* respectively and ω is the variable in the frequency domain. Applying the inverse Fourier Transform to equation (4.7), we obtain.

$$g(t) = \hat{\mathrm{F}}^{-1}(K(\omega)F(\omega)) \tag{4.8}$$

There are cases for which *g(t)* and *k(t)* are known and the solution for *f(t)* is needed. Applying a deconvolution can do this. From equation (4.7) we have

$$f(t) = \hat{\mathrm{F}}^{-1}\left(G(\omega)/K(\omega)\right) = \hat{\mathrm{F}}^{-1}\left(G(\omega)H(\omega)\right) \tag{4.9}$$

with $H(\omega) = 1/K(\omega)$. The same concept can be extended for the two-dimensional situation where we can write, similar to equation (4.7), the 2-D version of the convolution integral given by

$$g(t_1,t_2) = (k * f)(t_1,t_2) = \int_{-\infty}^{\infty}\int_{-\infty}^{\infty} k(t_1 - t_1^{'}, t_2 - t_2^{'})\, f(t_1^{'}, t_2^{'})\, dt_1^{'} dt_2^{'} \tag{4.10}$$

and in spectral representation

$$G(\omega_1,\omega_2) = K(\omega_1,\omega_2)F(\omega_1,\omega_2) \tag{4.11}$$

where ω_1, ω_2 are the two variables in the 2-D frequency domain. Similar to equation (4.8), the corresponding 2-D deconvolution will be

$$f(t_1,t_2) = \hat{\mathrm{F}}^{-1}\left(G(\omega_1,\omega_2)/K(\omega_1,\omega_2)\right) = \hat{\mathrm{F}}^{-1}\left(G(\omega_1,\omega_2)H(\omega_1,\omega_2)\right) \tag{4.12}$$

We will discuss more about deconvolutions later.

It is clear that convolution integrals require the kernel function to be expressed in terms of coordinate differences. It happens that kernel functions of integrals used in geodesy like Poisson's and Stokes', which can be written as functions of latitude and longitude, are expressed in terms of differences with respect to longitude but not with respect to latitude. To achieve the required form requires that we approximate the kernels, which introduces errors due to the meridian convergence that grow with the extension of the area of integration. For our study, from equations (3.2) and (3.13) the functions that need to be approximated are: $\cos(\psi)$ and $\tan(\alpha)$ which can be written as

$$\cos(\psi) = \cos(\phi)\cos(\phi'-\phi+\phi)\cos(\lambda'-\lambda) + \sin(\phi)\sin(\phi'-\phi+\phi)$$

$$\tan\alpha = \frac{\cos(\phi'-\phi+\phi)\sin(\lambda'-\lambda)}{\cos\phi\sin(\phi'-\phi+\phi) - \sin\phi\cos(\phi'-\phi+\phi)\cos\left(\lambda-\lambda'\right)} \tag{4.13}$$

We need to fix the second value of ϕ in $(\phi'-\phi+\phi)$ to a certain value, say ϕ_0 in (4.13) so the functions are expressed as functions of coordinate differences. Letting

$$\Delta\phi = \phi'-\phi,\ \ \Delta\lambda = \lambda'-\lambda \tag{4.14}$$

we can write

$$\cos(\psi) \simeq \cos(\phi_0)\cos(\phi_0+\Delta\phi)\cos(\Delta\lambda) + \sin(\phi_0)\sin(\phi_0+\Delta\phi)$$

$$\tan\alpha \simeq \frac{\cos(\phi_0+\Delta\phi)\sin(\Delta)}{\cos\phi\sin(\phi_0+\Delta\phi) - \sin\phi\cos(\phi_0+\Delta\phi)\cos\left(\Delta\lambda\right)} \tag{4.15}$$

This formula will give exact results only when $\phi = \phi_0$. The meridian convergence errors will increase as the distance between the computation point and the parallel with latitude ϕ_0 increases. A good choice for ϕ_0 is the mean latitude of the area. Now we can write integrals, like equations (3.1) and (3.17), in the fashion of a 2-D convolution with respect to latitude and longitude. Let's assume that functions of latitude and longitude *g, k,* and *f* are related as follows

$$g(\phi,\lambda) = \iint_{\sigma} k(\Delta\phi,\Delta\lambda)\, f(\phi',\lambda')\cos(\phi')d\phi d\lambda \tag{4.16}$$

which can be considered a 2-D convolution with respect to the coordinates ϕ and λ. Using the convolution operator * we can write

$$g = k*(f\cos(\phi)) \tag{4.17}$$

Then, according to the convolution theorem their spectra are related by

$$G(\omega_1,\omega_2) = K(\omega_1,\omega_2)\bar{F}(\omega_1,\omega_2) \tag{4.18}$$

With $\bar{F} = \hat{\mathrm{F}}(f\cos(\phi))$.

In order to evaluate integrals that involve differences, like the ones in equation (3.8) and (3.21), using the convolution theorem, the following assumptions have to be made: The

differences are to be given along meridians and with a constant angular distance between both satellites. Then using the space shifting property of Fourier Transforms (see Brigham, 1988)

$$f(t_1 - t_{1,0}, t_2 - t_{2,0}) \Leftrightarrow F(\omega_1, \omega_2) e^{-i2\pi\left[\omega_1 t_{1,0} + \omega_2 t_{2,0}\right]} \tag{4.19}$$

According to the assumptions just mentioned above, and considering potential and gravity disturbance differences as obtained from GRACE (see chapter 2), the grid formed by points of the leading satellite's positions will be the same as those of the trailing satellite's points but displaced by the angular distance separation to be designed as $\bar{\Delta}\phi$ and considered to be constant. Defining the observed quantity by Δg , and by g the related absolute values located at the trailing satellite's position, their spectra, ΔG, G , according to equation (4.19), are related as follows

$$\begin{aligned} \Delta G(\omega_1, \omega_2) &= G_2(\omega_1, \omega_2) - G_1(\omega_1, \omega_2) \\ &= G_1(\omega_1, \omega_2) e^{-i2\pi[\omega_2 \bar{\Delta}\phi]} - G_1(\omega_1, \omega_2) \\ &= G_1(\omega_1, \omega_2)\left[e^{-i2\pi[\omega_2 \bar{\Delta}\phi]} - 1 \right] \end{aligned} \tag{4.20}$$

We can see from this last equation that the zero frequencies along meridians have zero values for Δg and we are not able to solve for the corresponding frequencies of g. However, the introduction of some reference field, as is customary in geodesy, may alleviate the situation.

4.1.3 Integral Evaluation with 1-D FFT

Numerical integration it is known to be computationally intensive for large numbers of points. On the other hand evaluation of spherical convolutions with 2-D FT has the problem of meridian convergence, which makes the corresponding spatial interval along parallels change with different latitude. Another way to evaluate integrals over the sphere using spherical approximation, with more efficiency than direct numerical integration and avoiding the meridian convergence error is by using 1-D Fourier transform combined with numerical integration (see Haagmans, et. at, 1993). Still, the sampling interval has to be uniform along parallels. Assume that functions g and f are given on a grid of m points from west to east and n points along the meridians from south to north and let k be the kernel relating both as in equation (4.1). Values of g for points along a parallel of latitude ϕ_P are given by

$$g_{\phi_P}(\lambda_P) = \Delta\phi\Delta\lambda \cdot \hat{\mathrm{F}}_1^{-1}\left(\sum_{\phi_Q = \phi_1}^{\phi_n} \hat{\mathrm{F}}_1\left(k(\Delta\lambda_{PQ}) \right) \hat{\mathrm{F}}_1\left(f_{\phi_Q}(\lambda_Q) \cos\phi_Q \right) \right) \tag{4.21}$$

Where

$\hat{F}_1$ Represents the1-D Fourier transform.

$g_{\phi_P}(\lambda_P)$ Is the 1xm vector of g along the parallel of point P with latitude ϕ_P.

f_{ϕ_Q} Is the 1xm vector of f along the parallel of point Q with latitude ϕ_Q.

$k_{\phi_Q}(\Delta\lambda_{PQ})$ Is 1xm vector of k along the parallel of point Q with latitude ϕ_P.

That is, equation (4.21) will yield the evaluation of the integral in equation (4.1), after the appropriate discretization, for all points with latitude ϕ_P.

4.1.4 Cyclic Convolution Errors

Convolutions as shown by equations (4.5) and (4.10) are defined over the whole plane or line. In reality, only a finite amount of discrete data is usually available. This fact introduces discretization, truncation and edge effect errors. Furthermore, for computational efficiency one wants to employ discrete Fourier Transform, which implies an assumption of periodicity in the data and the kernel to be used. This produces the so-called cyclic convolution error. Discretization errors can only be reduced by reducing the sampling interval. Truncation errors are reduced with more area coverage or by applying kernel modification. Edge effect errors are avoided by discarding the solution near the edges. One way to eliminate the convolution error is to append zeros to the data and to extend the kernel periodically over double the area.

4.2 The Inversion Process (Inversion Methods)

Earlier in this chapter, it was mentioned that each method of integral evaluation is related to a different inversion process. In this section we discuss about these inversion methods. We want to mention that all these methods will still be affected by the ill-posedness of downward continuation. We will focus on that matter in the next section.

4.2.1 Space Domain Inversion

We call space domain inversion to the inversion associated to direct numerical integration. Considering measurement errors we can rewrite equation (4.2) as follows

$$\underset{nx1}{\mathbf{g}} = \underset{nxm}{\mathbf{A}}\ \underset{mx1}{\mathbf{f}} + \underset{nx1}{\mathbf{e}} \tag{4.22}$$

where n is the number of measurements and m is the number of unknowns, with $n \geq m$. Following the least squares principle, the value of the vector **f** is given by

$$\tilde{\mathbf{f}} = \left(\mathbf{A}^{\mathbf{T}}\mathbf{A}\right)^{-1}\mathbf{A}^{\mathbf{T}}\mathbf{g} \tag{4.23}$$

Direct numerical integration is known to be computationally intensive for large amounts of data. Besides that, the inversion process is very demanding on computer memory since **A** becomes a very large matrix. Still, this inversion is very accurate relative to the other two methods to be explained here.

4.2.2 Using 2-D FFT Convolution

In principle the inversion (deconvolution) using the 2-D deconvolution equation (4.12) is very simple as seen from that equation. Every spectral element of *f* is obtained by the simple ratio of the corresponding spectral elements of *g* and *k*. However, there is a problem about that. When we evaluate a convolution we employ padding techniques in order to remove cyclic-convolution errors. This will produce non-sensical data over the padding area. It happens that for the deconvolution case we do not have access to these unrealistic data. This lack of data will introduce errors in the solution. Here, we call those errors deconvolution errors. One way to get around this problem is to perform the deconvolution using some iteration method like the Projected Landweber method. These methods will be treated in the following section.

4.2.3 2-D Inversion with 1-D FFT

With respect to computational speed for a scalar computer, numerical integration using 1-D FFT is in the middle between direct numerical integration and the 2-D FFT method. While it is able to give exactly the same results in accuracy, it is faster than direct numerical integration. For inversion there seems to be a similar situation as we will see later. Apparently, nobody has tried so far to do 2-D inversion using 1-D FFT. We have found a way to do it that also allows to process more data than with space domain inversion. However, as in the 2-D FFT case there still remains the problem about the lack of knowledge of the unrealistic data produced in the implicit 1-D deconvolution, thus generating 1-D deconvolution errors. This problem could be expected to be less severe since it is only present along parallels. For this case, we start with equation (4.21) which, when solving for all parallels, can be expressed as

$$Y = AX \tag{4.24}$$

where from equation (4.21)

$$\begin{aligned} Y &= vec\left(\hat{F}_1\left(g_{\phi_1}\right), \hat{F}_1\left(g_{\phi_2}\right), \hat{F}_1\left(g_{\phi_3}\right), ..., \hat{F}_1\left(g_{\phi_n}\right)\right) \\ X &= vec\left(\hat{F}_1\left(f_{\phi_1}\cos\phi_1\right), \hat{F}_1\left(f_{\phi_2}\cos\phi_2\right), \hat{F}_1\left(f_{\phi_3}\cos\phi_3\right), ..., \hat{F}_1\left(f_{\phi_n}\cos\phi_n\right)\right) \end{aligned} \tag{4.25}$$

Considering the data to be over *n* parallels and *m* meridians

$$A = \begin{bmatrix} D_{11} & D_{12} & D_{13}... & D_{1n} \\ D_{21} & D_{21} & D_{23}... & D_{2n} \\ \vdots & \vdots & \vdots & \vdots \\ D_{n1} & D_{n2} & D_{n3}... & D_{nn} \end{bmatrix}, \qquad D_{i,j} = diag\left(\hat{F}_1\left(k_\phi(\Delta\lambda_{\phi_i,\phi_j})\right)\right) \tag{4.26}$$

Y will contain all the vectors of the spectral of the potential for every parallel at radius r, while X will have the same but at radius R. Thus they will be vectors containing nm elements. The size of every matrix D will be m by m and matrix A has size nm by nm. This matrix will be very large for larger numbers of measurements, thus, making it more difficult to solve for X. For instance, with a grid of 100x100 measurements the size of A would be 10000x10000. Furthermore, the elements of A are complex numbers since they are Fourier spectrum components. Still, since matrices D are diagonal matrices, matrix A will be a sparse banded matrix with mn^2 non-zero elements. Alternatively, can try to solve for the same component (i) of every spectral vector of the potential along the corresponding parallels. That is,

$$Y_i = A_i X_i \tag{4.27}$$

where

$$Y_i = \begin{bmatrix} \hat{F}_1\left(g_{\phi_1}\right)_i \\ \hat{F}_1\left(g_{\phi_2}\right)_i \\ \hat{F}_1\left(g_{\phi_3}\right)_i \\ \vdots \\ \hat{F}_1\left(g_{\phi_n}\right)_i \end{bmatrix}, \quad X_i = \begin{bmatrix} \hat{F}_1\left(f_{\phi_1}\cos\phi_1\right)_i \\ \hat{F}_1\left(f_{\phi_2}\cos\phi_2\right)_i \\ \hat{F}_1\left(f_{\phi_3}\cos\phi_3\right)_i \\ \vdots \\ \hat{F}_1\left(f_{\phi_n}\cos\phi_n\right)_i \end{bmatrix}, \quad A_i = \begin{bmatrix} D_{11}^i & D_{12}^i & D_{13}^i \ldots & D_{1n}^i \\ D_{21}^i & D_{22}^i & D_{23}^i \ldots & D_{2n}^i \\ D_{31}^i & D_{32}^i & D_{33}^i \ldots & D_{3n}^i \\ \vdots & \vdots & \ddots & \vdots \\ D_{n1}^i & D_{n2}^i & D_{n3}^i \ldots & D_{nn}^i \end{bmatrix} \tag{4.28}$$

and $D_{j,k}^i$ is a single element and matrix A_i is of size n by n. In this way we can solve for X_i which contains the spectral (i) component for every potential vector along the corresponding parallel at the earth surface.

Another way to look at this system of equations is the following. Let X and Y contain all the X_i's and Y_i's as follows

$$\begin{aligned} X &= vec\left(X_1, X_2, X_3, \ldots, X_m\right) \\ Y &= vec\left(Y_1, Y_2, Y_3, \ldots, Y_m\right) \end{aligned} \tag{4.29}$$

Then we have the system like equation (4.24) with A (with the same size) being a block diagonal matrix formed by matrices A_i.

4.2.4 Deconvolution Errors

The inverse operation of convolution integrals, like equations (4.5) and (4.10), is also called a deconvolution. This process can also be seen as a convolution on its own; with $h = \hat{\mathrm{F}}^{-1}(H)$ we can write, using the convolution theorem

$$f(t) = h(t) * g(t) \tag{4.30}$$

Thus, knowing *g(t)* and the deconvolution kernel *h(t)* we could easily solve for *f(t)* by using equation (4.6). As mentioned before, we have to take care of the cyclic convolution error if we want to have more accurate results and that can be done by using the appropriate padding strategy. However, there is a problem if we only know the analytic expression for the convolution kernel *k(t)* in the space domain. We can only obtain a discrete representation of *h(t)* for the area where data are given. Apparently, since we do not have access to its analytic expression we cannot use any padding technique to avoid the cyclic convolution errors. One common way to avoid this problem is to use some iterative methods like the Projected Landweber method for which we do not need to know the fictitious data implied by the convolution process. Furthermore, for the 1-D FFT case , if we are able to use data along the entire parallels we do not have to worry about cyclic-deconvolution errors. Extension of data along parallels will not increase the size of matrices A_i to be inverted, see equation (4.27), only the number of them. As a bonus, there will be no edge effect along parallels.

4.3 Regularization Methods

The downward continuation of quantities related to the terrestrial gravity field from the satellite's altitude is known to be a highly unstable process, even for the low-low SST concept. However, there are several techniques that can be employed to overcome or reduce the effect of the instability present on the solution of an ill-posed problem. Some of the most common methods used to stabilize an ill-conditioned process are: Tikhonov regularization method, truncated and damped singular value decomposition and least square collocation. Some iteration methods like Landweber and conjugate gradient method can also be used for systems involving large matrices. Except for the Landweber method, geodesists have pretty much treated these methods; see, for instance, Bouman (1998), Ilk (1993), Schwarz and Gerstl (1979), among others. A brief description of these methods is given below.

The basic idea of regularization consists of considering a family of approximate solutions depending on a positive parameter called a regularization parameter. The main property is that, in the case of noise-free data, the functions of the family converge to the exact solution of the problem when the regularization parameter tends to zero. In the case of noisy data one can obtain an optimal approximation of the exact solution for a non-zero value of the regularization parameter.

A mathematical problem is said to be well-posed if it satisfied the following conditions (Bertero, 1998; Hofmann, 1996; Schwarz and Gerstl 1979):

- The solution to the problem is unique.
- The solution exists for any data.
- The solution depends with continuity on the data.

If one of the three conditions above is not satisfied the problem is said to be ill-posed.

4.3.1 Tikhonov Regularization Method

Tikhonov regularization is the most important method for regularization of discretized noisy data problems present in geodesy and many other sciences. Suppose we have an ill-posed integral equation

$$\int_a^b K(x,y)\,f(y)dy = g(x) \quad a \le x \le b \tag{4.31}$$

The kernel K(x,y) is continuous and integrable. First, the system is made properly posed by defining the class of functions g_o that will solve equation (4.31). If we have an element of that class of functions, the corresponding $f_o(x)$ can be obtained within a certain approximation, see (Schwarz 1977; Hofmann, 1996)

$$\|f - f_o\| \le \delta \tag{4.32}$$

where $\|f\|$ means the L_2 norm,

$$\|f\| = \left\{ \int_a^b f^2(x)dx \right\}^{1/2} \tag{4.33}$$

Tikhonov now makes the assumption that $f_o(y)$ satisfies the inequality

$$\Omega(n)(f_o) < \infty \tag{4.34}$$

where $\Omega(n)(f)$ is a functional of the form

$$\Omega(n)(f) = \int_a^b \sum_{i=0}^{n+1} a_i(x) \left\{ \frac{d^i f(x)}{dx^i} \right\}^2 dx \tag{4.35}$$

$a_i(x)$ being a positive and continuous function. The class of functions obtained will depend on the selection of $\Omega(n)(f)$. The condition $\Omega(n)(f_o) < p$, where p is a constant, determines a compact set of solutions.

Then, a general method is determined for arriving at a regularizing operator B_α which, for any kind of function, $f(x)$, will produce the solution belonging to the prescribed class. Toward that end, Tikhonov uses the minimum condition (ibid)

$$\|Af - g\|^2 + \alpha\Omega(n)(f) \to \min \tag{4.36}$$

where

$$Af = \int_a^b K(x,y)\, f(y)dy \tag{4.37}$$

and $\alpha > 0$ is a regularization parameter to be chosen.
Finally, Tikhonov shows that the solution obtained converge toward the solution of the problem. That is, the solution

$$f_\alpha = B_\alpha g \tag{4.38}$$

minimizing (4.36) will converge uniformly to $g_o(y)$ as $\delta \to 0$. Let us consider the simple case $n = -1$, and $a_0(x) = 1$ where the minimum condition (4.36) reduces to

$$\|Af - g\|^2 + \alpha \|f\|^2 \to \min \tag{4.39}$$

where α is the positive Lagrange multiplier imposing a condition on the solution's norm in order to produce a stable solution. The solution corresponding to the minimum condition is

$$f_\alpha = \left(A^* A + \alpha I\right)^{-1} A^* g \tag{4.40}$$

which depends continuously on *f* where A^* is the adjoint of A. For a compact operator *A* with singular value decomposition (see next section) by $\{v_n, u_n\sigma_n\}$ the regularized solution can be given by.

$$f_\alpha^\varepsilon = \sum_{n=1}^{\infty} \frac{\sigma_n}{\sigma_n^2 + \alpha} \left\langle g^\varepsilon, u_n \right\rangle v_n = \sum_{n=1}^{\infty} \delta_n \frac{\left\langle g^\varepsilon, u_n \right\rangle}{\sigma_n} v_n \tag{4.41}$$

where g^ε is *g* contaminated by errors, and

$$\delta_n = \frac{\sigma_n^2}{\sigma_n^2 + \alpha} \tag{4.42}$$

where δ_i acts like a smoothing filter, which can also can be defined for less smoothing in the form

$$\delta_i = \frac{\sigma_i}{\sigma_i + \sqrt{\alpha}} \tag{4.43}$$

4.3.2 Singular Value Decomposition SVD

Let $A \in \mathbb{R}^{mxn}$ be a rectangular matrix with $m \geq n$. Then the SVD of *A* is expressed as

$$A = U \sum V^T = \sum_{i=1}^{n} u_i \sigma_i v_i^T \tag{4.44}$$

where $U = (u_1, u_2, ..., u_n)$ and $V = (v_1, v_2, ..., v_n)$ are matrices with orthogonal columns, such that $U^T U = V^T V = I_n$, and $\sum = diag(\sigma_1, \sigma_2, ..., \sigma_n)$ with $\sigma_1, \sigma_2, ..., \sigma_n$ being non-negative numbers called the singular values. They are arranged in decreasing order such that $\sigma_1 \geq \sigma_2 \geq ... \geq \sigma_n \geq 0$. The vectors u_i and v_i are the left and right eigenvectors of *A*, respectively. For discrete ill-posed problems, *A* turns out to be ill-conditioned and will have the following characteristics:

- The singular values σ_i will decay gradually to zero.
- The condition number given by σ_1/σ_n will be large.
- The left and right eigenvectors vectors u_i and v_i tend to have more sign changes in their elements as the index increase or σ_i decreases.

4.3.3 Truncated Singular Value Decomposition TSVD

In this method all the small singular values of *A*, are just ignored. The closest rank-k approximation A_k to *A* can be obtained by truncating the SVD expansion at *k*

$$A = A_k = \left(U \sum V^T\right)_k = \sum_{i=1}^{k} u_i \sigma_i v_i^T \quad k \leq n \tag{4.45}$$

This means that the singular values $\sigma_i \; i > k$ are considered to be zero. In this way, the almost rank deficient matrix *A* is replaced by an exactly rank deficient one, given by equation (4.44) that has a well defined null space of dimension $n - k$ spanned by the right eigenvectors vectors, $v_{k+1} ... v_n$ (Hansen, 1997). Based on this truncated *SVD* expansion the solution to the problem

$$\min \|f\| \text{ subject to } \min \|A_k f - g\| \tag{4.46}$$

will produce a regularized estimation for *f* given by

$$f_k = \sum_{i=1}^{k} \frac{u_i^T g}{\sigma_i} v_i \tag{4.47}$$

or using the filter factors δ_i

$$f_k = \sum_{i=1}^{n} \delta_i \frac{u_i^T g}{\sigma_i} v_i, \ \delta_i = \begin{cases} 1 \text{ for } i = 1...k \\ 0 \text{ for } i = k+1...n \end{cases} \tag{4.48}$$

This equation is similar to equation (4.41) for which δ is given by equation (4.42) or (4.43).

4.3.4 Damped Singular Value Decomposition DSVD

In the damped *SVD,* the cut off of the singular values is smoothly made by means of the filter factors δ_i this time defined as:

$$\delta_i = \frac{\sigma_i}{\sigma_i + \lambda} \tag{4.49}$$

where λ plays the role of regularization parameter.

4.3.5 Least Squares Collocation

Given a set of observations being linear functionals of the disturbing potential, least squares collocation (LSC) will yield the best approximation of any linear functional of the disturbing potential or the potential itself at any place above the Earth's surface (see Moritz, 1980). Moreover, this method is also feasible for interpolation being called least square prediction or interpolation. The observation equation is written as

$$\mathbf{y} = \mathbf{A}\mathbf{x} + \mathbf{s} + \mathbf{n} \tag{4.50}$$

where **y** is the observation vector of *m* observations, **A** is a known rectangular matrix of size *mxn*, **x** is a vector of *n* systematic parameters, **s** represents the signal to be solved, and **n** is the measurement noise vector. Assuming no systematic parameters, the vector **t** of a linear functional with respect to **s** at some selected points is estimated by

$$\mathbf{t} = \mathbf{C}_{\mathbf{ts}} (\mathbf{C}_{\mathbf{ss}} + \mathbf{D})^{-1} \mathbf{y} \tag{4.51}$$

where **D** is the covariance matrix of the vector **n**, $\mathbf{C}_{\mathbf{ts}}$ is the covariance matrix between the functional to be solved for at the corresponding points and the signal at the

measurement points and $\mathbf{C_{ss}}$ is the covariance matrix of the signal at the measurement points. The covariance matrices are computed from the covariance function of the potential through covariance propagation. LSC has been found (Rummel et al., 1979) to be related to Tikhonov regularization. The error variance/covariance matrix is given by

$$\mathbf{E_{tt}} = \mathbf{C_{tt}} - \mathbf{C_{ts}}(\mathbf{C_{ss}} + \mathbf{D})^{-1}\mathbf{C_{ts}^{T}} \tag{4.52}$$

We have that *DT* and *DGD* are not harmonic functions. Thus, theoretically it is not correct to use LSC to upward or downward continue them. Therefore, we are not considering this method for downward continuation. Nevertheless, we still can use it for interpolation and extrapolation purposes since the extrapolation distances are relatively small even in the vertical direction. Let's determine their covariance matrices. The covariance matrix C_{tt} for the disturbing potential in terms of spherical harmonic expansion is given by

$$C_{tt}(\psi, r_P, r_Q) = \sum_{n=0}^{360}\left(\frac{R_B^2}{r_P r_Q}\right)^{n+1} c_n P_n(\cos\psi) \tag{4.53}$$

where

ψ is the angle between the points P and Q from the origin (earth's center)

r_P, r_Q are radial distances from the origin to P and Q, respectively

R_B is the radius of the Bjerhammar sphere

c_n is the degree variance of the disturbing potential

P_n are the Legendre polynomials.

The disturbing potential degree variance can be computed by;

$$c_n = \sum_{m=-n}^{n} t_{nm}^2 \tag{4.54}$$

where t_{nm} are the coefficients of the disturbing potential spherical harmonic expansion. They can be expressed in terms of the corresponding harmonic coefficients of the real and normal gravitational potential, v_{nm} and v_{nm}^{normal}. The disturbing potential is given by

$$T(r,\phi,\lambda) = V(r,\phi,\lambda) - V_N(r,\phi,\lambda) \tag{4.55}$$

with:

$$V(r,\phi,\lambda)=\frac{GM}{r}\left(1+\sum_{n=2}^{N\max}\sum_{m=-n}^{n}\left(\frac{R}{r}\right)^{n+1}v_{nm}\bar{Y}_{nm}(\theta,\lambda)\right) \tag{4.56}$$

and

$$V_N(r,\phi,\lambda)=\frac{GM}{r}\left(1+\sum_{n=2}^{N\max}\sum_{m=-n}^{n}\left(\frac{R}{r}\right)^{n+1}v_{nm}^{normal}\bar{Y}_{nm}(\theta,\lambda)\right) \tag{4.57}$$

where GM is the gravitational constant times the Earth's mass and $\bar{Y}_{nm}$ is a fully normalized surface spherical harmonic function of degree n and order m. The harmonic expansion of T can then be given by

$$T(R,\phi,\lambda)=\sum_{n=2}^{N\max}\sum_{m=-n}^{n}\left(\frac{R}{r}\right)^{n+1}t_{nm}\bar{Y}_{nm}(\theta,\lambda) \tag{4.58}$$

The expression for the harmonic coefficients t_{nm} is now given by;

$$t_{nm}=\frac{GM}{R}\left(v_{nm}-v_{nm}^{normal}\right)=\frac{GM}{R}\delta v_{nm} \tag{4.59}$$

To derive the expression of the covariance function $C_{DTDT}(X_P,X_Q)$ we express the covariances in terms of the expectation operator E{ }, $(\mathrm{E}\{x\}=\mu_x)$, for a random quantity x. That is;

$$\begin{aligned}C_{DT_pDT_Q}&=E\left\{\left[DT_P-E\{DT_P\}\right]\left[DT_Q-E\{DT_Q\}\right]\right\}\\&=E\left\{DT_P\cdot DT_Q\right\}\\&=E\left\{\left(T_{P_2}-T_{P_1}\right)\cdot\left(T_{Q_2}-T_{Q_1}\right)\right\}\\&=E\left\{T_{P_2}\cdot T_{Q_2}-T_{P_2}\cdot T_{Q_1}-T_{P_1}\cdot T_{Q_2}+T_{P_1}\cdot T_{Q_1}\right\}\end{aligned} \tag{4.60}$$

Then,

$$\begin{aligned}C_{DT_PDT_Q}=&C_{TT}(\psi_{P_2Q_2},r_{P_2},r_{Q_2})-C_{TT}(\psi_{P_2Q_1},r_{P_2},r_{Q_1})-\\&C_{TT}(\psi_{P_1Q_2},r_{P_1},r_{Q_2})+C_{TT}(\psi_{P_1Q_1},r_{P_1},r_{Q_1})\end{aligned} \tag{4.61}$$

and also

$$C_{T_PDT_Q}=C_{TT}(\psi_{PQ_2},r_P,r_{Q_2})-C_{TT}(\psi_{PQ_1},r_P,r_{Q_1}) \tag{4.62}$$

Similarly, for DGD the covariance matrix is given by

$$C_{DGD_P DGD_Q} = C_{\delta_\varepsilon \delta_\varepsilon}(\psi_{P_2Q_2}, r_{p_2}, r_{Q_2}) - C_{\delta_\varepsilon \delta_\varepsilon}(\psi_{P_2Q_1}, r_{P_2}, r_{Q_1}) - C_{\delta_\varepsilon \delta_\varepsilon}(\psi_{P_1Q_2}, r_{P_1}, r_{Q_2}) + C_{\delta_\varepsilon \delta_\varepsilon}(\psi_{P_1Q_1}, r_{P_1}, r_{Q_1}) \tag{4.63}$$

where is given by equation (3.17). The derivation of the covariance $C_{\delta_\varepsilon \delta_\varepsilon}$ is not as straightforward. Knowing that the gravity disturbance is a linear functional of *T*, its covariance can be expressed in terms of C_{TT} using variance propagation. From equation (3.17) we can write

$$\begin{aligned} C_{\delta_{\varepsilon P}\delta_{\varepsilon Q}}(\psi_{PQ}, r_P, r_Q) &= C_{\delta_{\phi P}\delta_{\phi Q}}(\psi_{PQ}, r_P, r_Q)\cos^2\alpha + C_{\delta_{\lambda P}\delta_{\lambda Q}}(\psi_{PQ}, r_P, r_Q)\sin^2\alpha \\ &+ \left(C_{\delta_{\phi P}\delta_{\lambda Q}}(\psi_{PQ}, r_P, r_Q) + C_{\delta_{\lambda P}\delta_{\phi Q}}(\psi_{PQ}, r_P, r_Q)\right)\sin\alpha\cos\alpha \end{aligned} \tag{4.64}$$

where, using the derivative operator *D* and covariance propagation, we have for the variances of the meridian and east-west components the following equations

$$\begin{aligned} C_{\delta_\phi \delta_\phi}(\psi_{PQ}, r_P, r_Q) &= \frac{1}{r_P r_Q} D_{\phi_P} D_{\phi_Q} K(\psi_{PQ}, r_P, r_Q) \\ C_{\delta_\lambda \delta_\lambda}(\psi_{PQ}, r_P, r_Q) &= \frac{1}{r_P r_Q \cos\phi_P \cos\phi_Q} D_{\lambda_P} D_{\lambda_Q} K(\psi_{PQ}, r_P, r_Q) \\ C_{T\delta_\phi}(\psi_{PQ}, r_P, r_Q) &= \frac{1}{r_Q} D_{\phi_Q} K(\psi_{PQ}, r_P, r_Q) \\ C_{T\delta_\lambda}(\psi_{PQ}, r_P, r_Q) &= \frac{1}{r_Q \cos\phi_Q} D_{\lambda_Q} K(\psi_{PQ}, r_P, r_Q) \end{aligned} \tag{4.65}$$

Where $K = C_{TT}$. Now using $z = \cos\psi_{PQ}$ we can write

$$\begin{aligned} D_{\phi_Q} K &= D_{\phi_Q} zK' \\ D_{\lambda_Q} K &= D_{\lambda_Q} zK' \\ D_{\phi_P} D_{\phi_Q} K &= D_{\phi_P} zD_{\phi_Q} zK'' + D^2_{\phi_P\phi_Q} zK' \\ D_{\lambda_P} D_{\lambda_Q} K &= D_{\lambda_P} zD_{\lambda_Q} zK'' + D^2_{\lambda_P\lambda_Q} zK' \end{aligned} \tag{4.66}$$

with

$$K' = D_z K = \sum_{n=0}^{360} \left(\frac{R_B^2}{r_P r_Q} \right)^{n+1} c_n P_n'(\cos\psi_{PQ})$$
$$K'' = D_{zz} K = \sum_{n=0}^{360} \left(\frac{R_B^2}{r_P r_Q} \right)^{n+1} c_n P_n''(\cos\psi_{PQ}) \quad (4.67)$$

The formulas for the derivatives of z with respect to ϕ and λ using equation (3.2) are given by

$$D_{\phi_P} z = \cos\phi_P \sin\phi_Q - \sin\phi_P \cos\phi_Q \cos(\lambda_Q - \lambda_P)$$
$$D_{\phi_Q} z = \sin\phi_P \cos\phi_Q - \cos\phi_P \sin\phi_Q \cos(\lambda_Q - \lambda_P) \quad (4.68)$$
$$D^2_{\phi_P\phi_Q} z = \cos\phi_P \cos\phi_Q + \sin\phi_P \sin\phi_Q \cos(\lambda_Q - \lambda_P)$$

and

$$D_{\lambda_P} z = \cos\phi_P \cos\phi_Q \sin(\lambda_Q - \lambda_P)$$
$$D_{\lambda_Q} z = -\cos\phi_P \cos\phi_Q \sin(\lambda_Q - \lambda_P) \quad (4.69)$$
$$D^2_{\lambda_P\lambda_Q} z = \cos\phi_P \cos\phi_Q \cos(\lambda_Q - \lambda_P)$$

Finally, the formula for $C_{\delta g_\varepsilon \delta g_\varepsilon}(\psi_{PQ}, r_P, r_Q)$ can be obtained by combining equations (4.64), (4.65), (4.66), (4.67), (4.68) and (4.69).

4.3.6 Iteration Methods

Iterative methods have the advantage that no matrix inversion is required, thus, allowing the solution of systems involving larger matrices. Another advantage of these methods is that additional constraints can be incorporated into the solution algorithm. Some iteration methods can be used to regularize the solution of linear ill-posed problems. The role of the regularization parameter is played by the number of iterations. For the case of noisy data, there is a semi-convergence; when the number of iterations increases, the solution first approaches the true solution and then diverges. For regularization purposes, the idea is to stop the iteration process before the solution becomes oscillatory due to magnification of data errors.

4.3.6.1 The van Citterd Method

The van Citterd method (Jansson, 1998; Lagendijk and Biemond, 1991) is an iterative process applied to the original equation (4.2). In this method, the iteration starts assuming

g to be the first approximation f_0 of f. The difference $g - Af_0$ is in some way related to the error in the estimate of f, $f - f_0$. This difference of g could be applied as a correction to the estimate of f. Thus producing a new estimate of f :

$$f_1 = f_0 + \tau(g - Af_0) \tag{4.70}$$

One may continue the process hoping to obtain a better estimate:

$$f_{k+1} = f_k + \tau(g - Af_k) \tag{4.71}$$

where τ is called the relaxation parameter. This method is known for its very slow rate of convergence so it can only be applied to certain systems having some particular properties. The convergence problems are more serious when the data are band limited and are affected by out-of-band noise. Then, some prefiltering is required to alleviate the problem. The importance of this method rests in the fact that is the base of other more useful iterative methods like the Landweber method, which is explained below.

4.3.6.2 The Landweber Method

The Landweber or successive approximations method is an example of the so-called *gradient methods* (Jansson, 1998; Lagendijk and Biemond, 1991). On these iteration methods at each step, the new approximation is obtained by modifying the old one in the direction of the gradient of the discrepancy functional. The Landweber method is applied to the equation

$$A^*Af = A^*g, \text{ or } \bar{A}f = \bar{g} \tag{4.72}$$

It has a faster convergence rate than the van Citterd method (ibid), and the iteration is done in a similar way

$$f_{k+1} = f_k + \tau A^*(g - Af_k) \tag{4.73}$$

where τ is a relaxation parameter to be determined.

4.3.6.3 The Projected Landweber Method

In the projected Landweber method the simple Landweber method is modified in order to take into account a priori information about the solution. This feature can be used to solve some constrained least squares or deconvolution problems. Some of the constraints that can be applied are the following (Bertero et al., 1998):

- Non-negativity: $f(t) \geq 0$.
- Causality: $f(t) = 0$ for $t < 0$ if $g(t) = 0$ for $t < 0$.

- Finite duration $f(t) = 0$ for $t > T$.

The iteration scheme is as follows

$$f_{k+1} = P_c \left\{ f_k + \tau A^* (g - A f_k) \right\} \tag{4.74}$$

The relaxation parameter for this case has to satisfy the following condition

$$0 < \tau < \frac{2}{\|A\|} \tag{4.75}$$

For our situation, where we consider data over a limited area, we can only apply the last one of the above constraints. This method can be used, for instance, with the 1-D FFT method where the convolution *Af* is evaluated according to equation (4.21) and the operator P_c will consist of removing the effects of the padding technique used in the 1-D FFT convolution.

4.3.5.4 Conjugate Gradient Method

The conjugate gradient method is a direction method, which can be considered as a special orthogonal expansion, in the Gram-Schmidt sense, of the solution of the minimization problem (Hanke, 1995). This expansion is generated by making use of information of previous iteration steps. This method starts with the solution provided by methods like Landweber at step *k*, an approximation of which is a combination of the functions $A^T g$, $A^T A A^T g$, $(A^T A)^2 A^T g$, …, $(A^T A)^{k-1} A^T g$. Regardless of the choice of the relaxation parameter, the result of the kth iteration will always lie in a subspace spanned by these functions. This is the so-called *Krylov* subspace; see for instance (Bouman, 1998; Bertero and Boccacci, 1998), $\mathrm{K}^{(k)}(A^T A, A^T g)$, whose dimension is *k* if the above-mentioned elements are linearly independent. The conjugate gradient method provides the function $\mathrm{K}^{(k)}(A^T A, A^T g)$ which minimizes the discrepancy functional

$$\eta(f : g) = \frac{1}{2}(A^T A f , f) - (A^T g, g) \tag{4.76}$$

where (,) is the inner product operator. This method is known for its rapid convergence and is based on the iterative construction of two bases r_k and p_k :

- $r_0 = p_0 = \bar{g}$
- $\alpha_k = \dfrac{\|r_k\|^2}{\langle r_k, \bar{A} p_k \rangle}$
- $r_{k+1} = r_k - \alpha_k \bar{A} p_k$

- $\beta_k = -\dfrac{\left\langle r_{k+1}, \bar{A}p_k \right\rangle}{\left\langle p_k, \bar{A}p_k \right\rangle}$
- $p_{k+1} = r_{k+1} + \beta_k p_k$

Then, the iterative scheme for the computation of the approximate solution is given by

$$f_0 = 0, \quad f_{k+1} = f_k + \alpha_k p_k \tag{4.77}$$

4.3.6.5 Stopping Criterion

For any iteration method, a criterion for stopping the iteration process has to be defined. At the end of each iteration we can compute the relative residual error by:

$$\varepsilon_k = k \frac{\|Af_k - g\|}{\|g\|} \tag{4.78}$$

where *k* is a parameter to be determined and is commonly assumed to be one. We could stop the iteration if this quantity is of the order of the experimental error. This is called the discrepancy criterion.

4.3.7 Determination of Optimum Regularization Parameter

One of the main problems of regularization is the choice of the regularization parameter. We know that a small regularization parameter will yield a good approximation to the least squares estimator, see equation (4.22), but we may have large effects of measurement errors since the instability has not been sufficiently reduced. On the other hand, a large regularization parameter reduces the effect of measurement errors on the solution but, increases the regularization or approximation errors; see, for instance Schwarz (1979), Bouman (1998) and Ilk (1993). There are some techniques that help to do the search for an optimal regularization parameter; among the most popular methods are the discrepancy principle method (Morozov, 1984) and the L-curve method (Hansen, 1997). Methods for finding the optimum regularization parameter don't always lead to the best solution even if convergence is achieved (Ilk, 1993). The convergence is more difficult to achieve as the process becomes more ill-conditioned.

4.3.7.1 Discrepancy Principle

This method is considered as an posteriori method to find the regularization parameter (Bouman, 1998). If we are given the noisy measurements g^{ε} of g with errors ε:

$$g^{\varepsilon} = Af + \varepsilon \tag{4.79}$$

We choose the regularization parameter α such that

$$\alpha f_\alpha^\varepsilon + A^* A f_\alpha^\varepsilon = A^* g^\varepsilon \tag{4.80}$$

and

$$\left\| A f_\alpha^\varepsilon - g^\varepsilon \right\| = \sigma, \quad \sigma = \|\varepsilon\| \tag{4.81}$$

The regularization parameter is obtained by solving the following equation with Newton's method

$$Z(\alpha) = \left\| A f_\alpha^\varepsilon - g^\varepsilon \right\|^2 - \sigma^2 = 0 \tag{4.82}$$

Using equation (4.81) we can obtain an expression for the norm on equation (4.83) as follows

$$\begin{aligned} \left\| A f_\alpha^\varepsilon - g^\varepsilon \right\|^2 &= \left\langle g^\varepsilon - A f_\alpha^\varepsilon, g^\varepsilon - A f_\alpha^\varepsilon \right\rangle \\ &= \left\langle g^\varepsilon - A f_\alpha^\varepsilon, g^\varepsilon \right\rangle - \left\langle A^* \left(g^\varepsilon - A f_\alpha^\varepsilon \right), f_\alpha^\varepsilon \right\rangle \\ &= \left\| g^\varepsilon \right\|^2 - \left\langle f_\alpha^\varepsilon, A^* g^\varepsilon \right\rangle - \alpha \left\| f_\alpha^\varepsilon \right\|^2 \end{aligned} \tag{4.83}$$

we get for equation (4.82)

$$Z(\alpha) = \left\| g^\varepsilon \right\|^2 - \left\langle f_\alpha^\varepsilon, A^* g^\varepsilon \right\rangle - \alpha \left\| f_\alpha^\varepsilon \right\|^2 - \sigma^2 \tag{4.84}$$

which has a derivative with respect to α that is given by

$$Z'(\alpha) = -\left\langle \frac{df_\alpha^\varepsilon}{d\alpha}, A^* g^\varepsilon \right\rangle - \left\| f_\alpha^\varepsilon \right\|^2 - 2\alpha \left\langle \frac{df_\alpha^\varepsilon}{d\alpha}, f_\alpha^\varepsilon \right\rangle \tag{4.85}$$

From equation (4.80), we obtain

$$\frac{df_\alpha^\varepsilon}{d\alpha} = -\left(A^* A + \alpha I \right)^{-1} f_\alpha^\varepsilon \tag{4.86}$$

with the iteration scheme given by

$$\alpha_{n+1} = \alpha_n - \frac{Z(\alpha_n)}{Z'(\alpha_n)} \tag{4.87}$$

We start with some initial value for α and iterate until

$$\left\| A f_\alpha^\varepsilon - g^\varepsilon \right\| = \sigma \tag{4.88}$$

4.3.7.2 The L-curve Method

The L-curve method consists of plotting the norm $\left\| Lf_\alpha^\varepsilon \right\|$ of the regularized solution, where L is the differential operator (see Bouman, 1998 and Hansen, 1993), with respect to the residual norm (*res*), which is given by

$$res = Af_\alpha^\varepsilon - g^\varepsilon \tag{4.89}$$

The differential operator L is defined as

$$L = \frac{d^n}{dx^n} \tag{4.90}$$

In the simple case of $n = 0$, L is equal to the identity operator. For ill-posed problems, when plotted in log-log scale, the plot will have an L-shaped curve. Given the measurement g^ε , there will be an optimal α that balances the effects of the measurement and the regularization error on the solution. A characteristic of the L-curve is that the optimal regularization parameter is not far from the regularization parameter that corresponds to the L-curve corner. That is, by locating the corner of the curve we can obtain a regularized solution with good balance between the two error types.

In order to verify this, we consider the true solution *f*. The associated error of a regularized solution is given by

$$f_\alpha^\varepsilon - f = A_\alpha^+(g^\varepsilon - g) + (A_\alpha^+ - A^+)g \tag{4.91}$$

with

$$A_\alpha^+ = (A^*A + \alpha I)^{-1}A^*,\ A^+ = (A^*A)^{-1}A^* \tag{4.92}$$

Equation (4.91) shows that the error $f_\alpha^\varepsilon - f$ in the regularized solution consists of two components, namely, a perturbation error from the error ε in the measurements and a regularization error due to the regularization of the error free component g. When only a small regularization parameter is introduced, the error $f_\alpha^\varepsilon - f$ is dominated by perturbation errors. On the other hand, with a large value of the regularization parameter the error $f_\alpha^\varepsilon - f$ will be dominated by regularization errors. This method is also called the Miller method (Bertero, 1998).

The L-curve displays the trade-off between the regularized solution and residual norms. The vertical part of the curve corresponds to solutions where the effect of the ill-condition of the system due to data errors dominates. The horizontal part corresponds to solutions where regularization errors dominate. Thus, the best trade-off will be given by solutions located at the corner of the curve. This, allows us to compute a regularized solution with a good balance between the two error types. Figure (4.1) shows a typical shape of the L-curve.

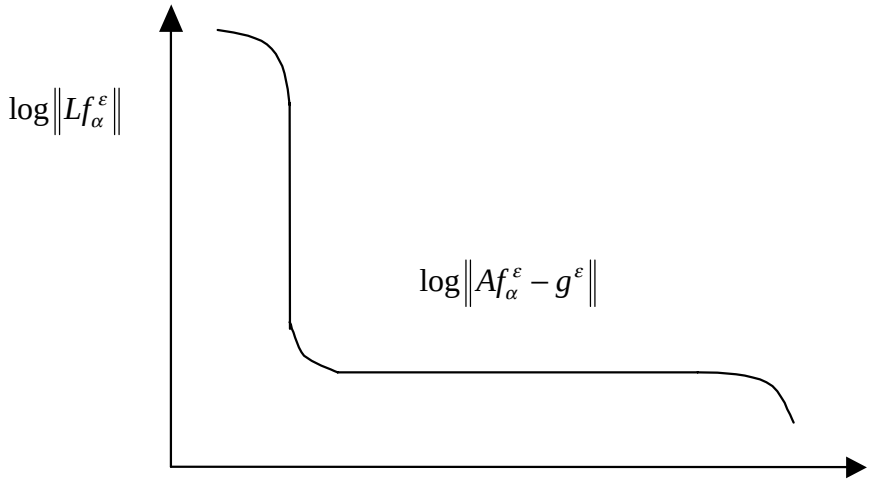

Figure 4.1: The L-*curve* in log-log scale, according to Hansen, 1997.

CHAPTER 5

NUMERICAL TESTS

5.1 The ill-posedness of the problem

We start our numerical analysis, by looking at the ill-posedness of the downward continuation process or the ill-condition of the matrices obtained after discretizing the integrals of equation (3.8) and (3.21). These integrals relate our observables, disturbing potential differences, *DT*, and differences of the gravity disturbance, *DGD*, given at satellite altitude, to the disturbing potential at zero altitude. A way to measure the ill-condition of a system is by using the condition number of the matrix to be inverted. For the inversion methods employed in this study, the solutions are obtained by the inverting matrix $N = (A^T A)$. The L_1 condition number of a matrix *N*, with nxn size, is defined to be $condn(N) = \|N\|_1 \|N^{-1}\|_1$, where $\|(\cdot)\|_1$ represents the L_1 norm operator. For a matrix, this operator is given by

$$\|N\|_1 = \max \|N^{\langle i \rangle}\|_1, \; i = 1, m, \quad \|N^{\langle i \rangle}\|_1 = \sum_{j=1}^{n} |N_{j,i}| \tag{5.1}$$

When the condition number is greater than 1/*e* (where *e* is the computer precision) then, the matrix is considered to be ill-conditioned and very small changes in the data will cause very large changes in the solution. For the following tests, the condition number was computed using a UDU^T or diagonal pivoting factorization for real, symmetric, indefinite coefficient matrices. That is

$$N = UDU^T \tag{5.2}$$

where *U* is an upper triangular matrix and *D* is a diagonal one. It is known that, in the discretization of integrals like Poisson's integral, the main factors affecting the ill-condition of the associated matrix are altitude, sampling interval and area coverage (number of data points). The higher the measurements the more unstable is the system due to the attenuation of the gravity signal with altitude. On the other hand, the ill-condition will also increase with a reduction in the sampling interval and with an increase of the solution and integration areas. Each of these factors will make the columns of the matrix numerically more similar.

5.1.1 Effects of Data Configuration Variations on System Stability

In order to analyze the altitude dependency of the system stability, the following geometric configuration was employed. Considering the unknown values of *T* to be at the Earth's surface on a regular grid with respect to meridians and parallels with 0.4^o sampling interval over a 12^o square area. The geographical location of the initial solution point is $\phi_0 = 45^o$, $\lambda_0 = 0^o$. The measurements, *DT* or *DGD*, were generated considering the middle point between the two satellites for every measurement to lie over the same grid of the unknowns but at constant altitude. We also assume that both satellites are on the same meridian and have a constant angular separation of 2^o (230 km); this intersatellite configuration will be assumed for all our tests, unless otherwise specified. The elements of the design matrices relating *T* with *DT* and *DGD*, of the above configuration, were computed according to equations (3.8), (3.21), (4.3) and (4.4). The condition number of the corresponding ($A^T A$) matrix was computed considering the measurements to be given at different altitudes. In Figure 5.1 we have the relationship between the condition number and the altitude of the data for both *DT* and *DGD* kernels. Here, we are assuming the numerical computer precision of 16 digits. Thus, according to the criteria mentioned above, it seems that the systems are ill-conditioned for altitudes greater than 150 km where the condition number is about $1x10^{15}$ for both type of kernels. Furthermore, since the operational altitude of the GRACE mission is projected to be within the 300-500 km range, we could expect according to Figure 5.1, the condition numbers of the related systems to be about $1x10^{19} - 1x10^{21}$ for the given geometrical configuration.

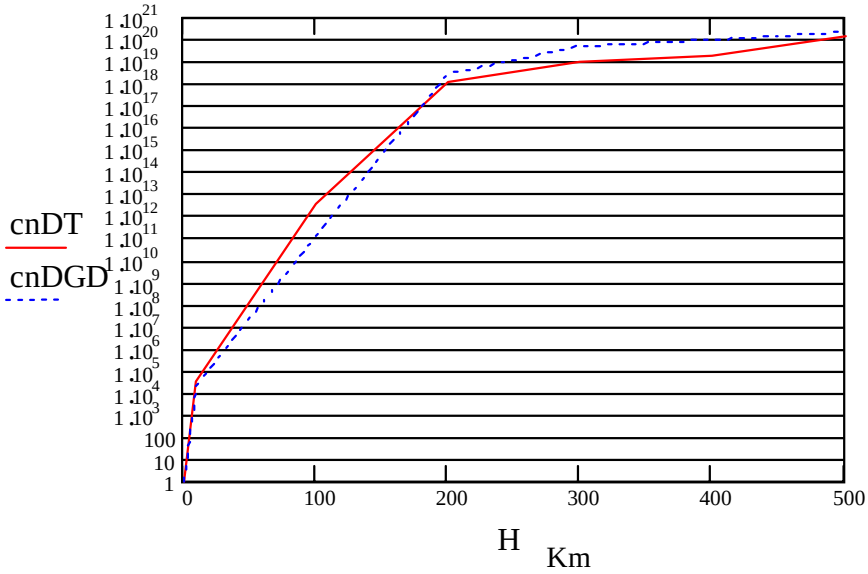

Figure 5.1: Condition number with respect to altitude of $A^T A$ for a grid with 0.4^o sampling interval covering 12^o square area and using kernels for *DT* (cn*DT*) and for *DGD* (cn*DGD*). The mid-latitude of the area is $\phi_m = 51^o$.

For the sampling interval variation effects, the condition number was computed for different data sampling intervals at 400 km altitude. Figure 5.2a shows the corresponding condition numbers for both kernels. As expected, the condition number increases as the sampling interval gets smaller, going from $8x10^{20}$ and $9x10^{21}$ at 0.2^o interval, respectively, for the *DT* and *DGD* kernels to about $8x10^{18}$ at $1^o.2$ interval for both kernels. However, for the range of sampling intervals considered in the Figure ($0^o.2$-$1^o.2$) the instability of the systems is approximately the same for either kernel.

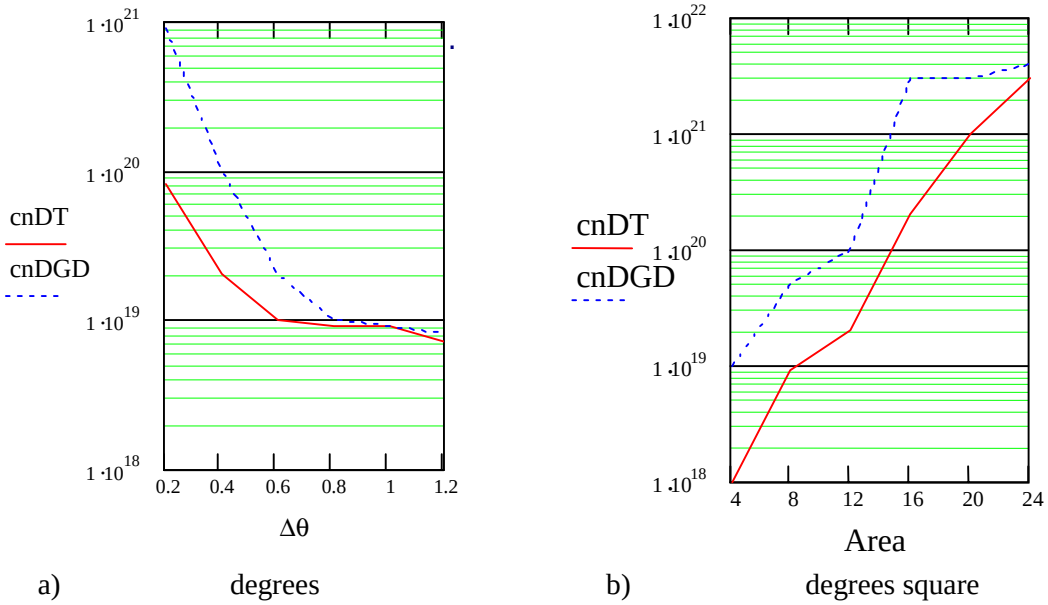

Figure 5.2: Condition number a) in terms of sampling interval for 12^o square and b) in terms of area coverage with $0^o.4$ sampling interval, using kernels for *DT* (cn*DT*) and for *DGD* (cn*DGD*), H=400 km $\phi_m = 51^o$.

With respect to dependency on area coverage, as mentioned before, the ill-condition increases with the area for a given sampling interval, provided the solution area increases correspondily. That is, more area means more points involved and a larger matrix to be inverted. This fact is supported by Figure 5.2b. Using $0^o.4$ constant intervals and with the same altitude of the data as in the previous test, the *DT* and *DGD* kernels were computed for several areas from 4^o to 24^o squares. The condition number increased from $1x10^{18}$ to $3x10^{22}$, respectively, for the *DT* kernel. On the other hand, the *DGD* kernel yielded relatively larger values, going from $1x10^{19}$ to $4x10^{22}$, respectively, for 4^o and 24^o square areas.

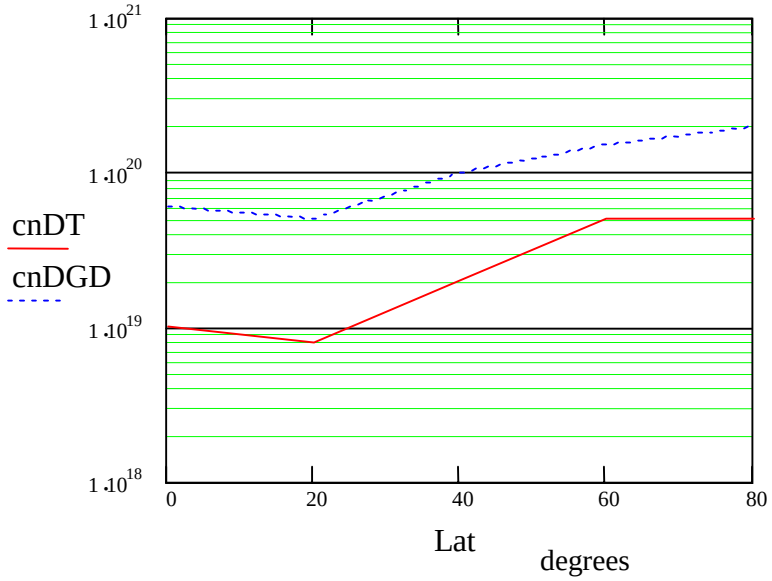

Figure 5.3: Condition number in terms of latitude (mid-latitude of the area) using kernels for *DT* (cn*DT*) and for *DGD* (cn*DGD*), H=400 km, sampling interval of $0^o.4$ and for 12^o square area.

For a grid of points being regular with respect to latitude and longitude, the ill-posedness tends to increase toward the polar regions due to the meridian convergence, which makes data points to get closer along parallels. Using the same regular grid as before, the condition number was computed for the *DT* and *DGD* kernels considering different mean latitudes. Figure 5.3 displays the condition numbers obtained. The variation is relatively small in going from the equator to 80^o latitude. The *DGD* kernel consistently yields larger condition numbers, from $6x10^{19}$ at the equator to $2x10^{20}$ at 80^o latitude, whereas the corresponding condition numbers of the *DT* kernel were $1x10^{19}$ and $5x10^{19}$, respectively.

5.1.2 Effects of Measurement and Model Errors

5.1.2.1 Measurement Errors

Next, we study the performance of regularization with the presence of measurement errors. In order to use a system of manageable size but having a relatively large area, a grid of $0^o.8$ sampling interval was employed, covering a 24^o square area. *DT* values were generated at 400 km altitude using the EGM96 geopotential model (Lemoine et al.,1998) with spherical harmonic coefficients with degree and order in the range 20-180 (from now on, unless otherwise specified, this gravitational field model will generate the quantities involved in all tests).

In order to determine the performance of regularization when only random errors in the measurement are present, we generated the *DT* by upward continuating to 400 km altitude (using equation 3.8) of disturbing potential values computed on the grid mentioned above at zero altitude. Then, we added random noise of different standard deviations to the *DT* thus generated. Subsequently, we estimated values of *T* at zero altitude using equation (4.39). By trial, we obtained the best α for every measurement noise level, that is, the one that yields the smallest standard deviation of the solution errors. Figure 5.4 plots the errors and the best α in terms of measurement errors considering the whole grid. Apparently, for this case, measurement errors smaller than $1x10^{-5}$ m^2/s^2 are required to obtain solution errors of 1 m^2/s^2 and a relative error of less than 10 % with respect to the signal. The associated best α is about $1x10^{-30}$. Figure 5.5 plots the dependency between α and the condition number of the system $(A^T A+\alpha_{best} I)$. It can be seen in the figure that for the above α, the system will have a condition number of $1x10^{10}$.

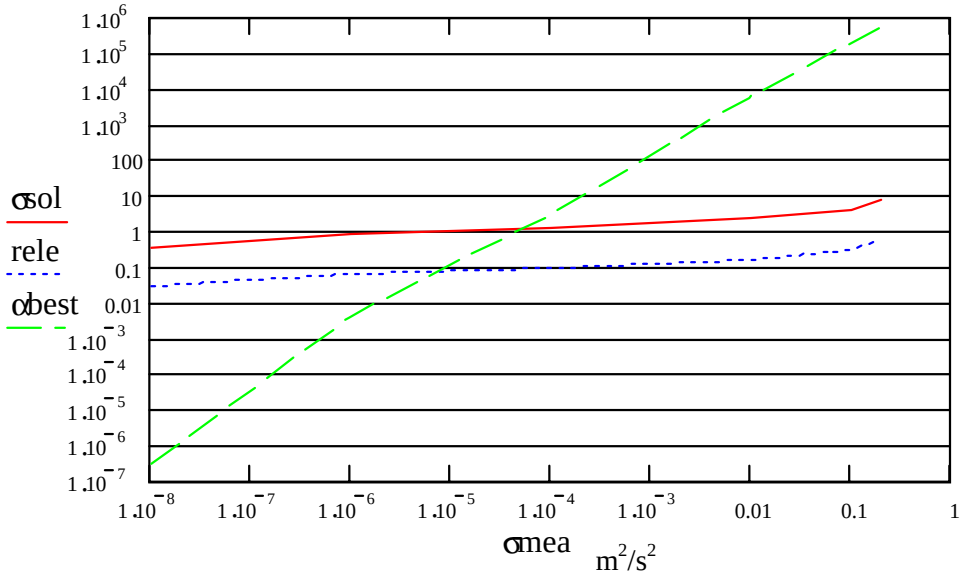

Figure 5.4: Relationship between the best α ($x10^{-29}$) and measurement and solution errors, in m^2/s^2, and relative solution errors, using kernel for *DT*, H=400 km, sampling interval of 0.8° and for 24° square area. $\phi_m = 51^o$.

Obviously, an ill-conditioned system will also amplify computational or round-off errors. For the previous test, when using errorless data and zero regularization parameter, the r.m.s. of the solution error was about $5 \cdot 10^{-3}$ m^2/s^2. The value of the optimum α found was about $1 \cdot 10^{-40}$ which yielded solution errors with a r.m.s. of $1 \cdot 10^{-5}$ m^2/s^2, which is relatively small. Therefore, we can say that errors of Figure (5.4) tests exclude model errors.

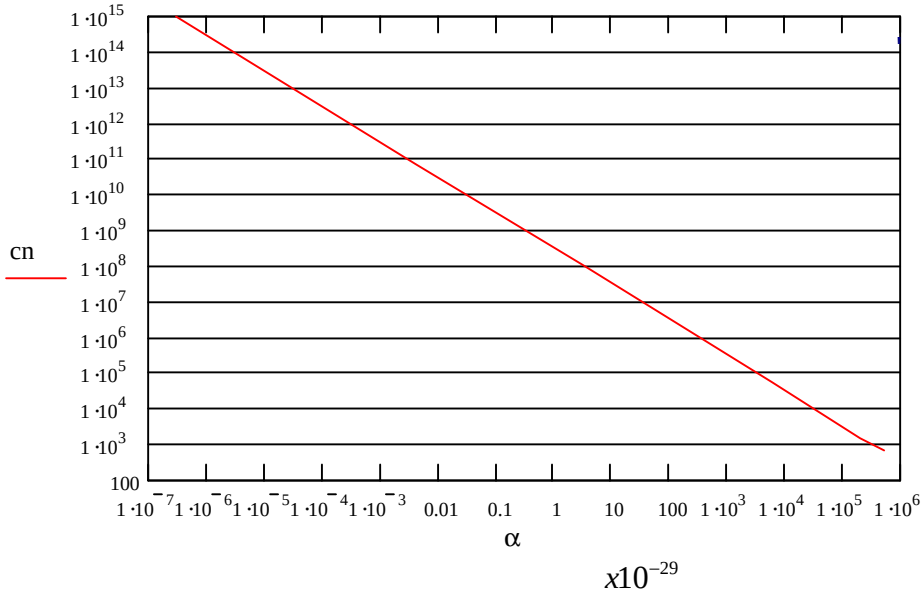

Figure 5.5: Condition number in terms of regularization parameter for *DT* kernel, H=400 km, sampling interval of 0.8^o and for 24^o square area $\phi_m = 51^o$.

Next, we apply the same procedure to several data sets generated at different locations along the same parallels so the same matrix can be used. Nine different and independent data sets from 0^o to 192^o longitude were generated. Then, the corresponding regularized solutions were obtained considering only random errors in the same way as in the previous test, but only with standard deviation of $\sigma = 0.01\,\mathrm{m^2/s^2}$. From now on we will only consider the measurement errors to have Gaussian distribution with $\sigma = 0.01\,\mathrm{m^2/s^2}$ for *DT* and $\sigma = 0.01\,\mathrm{mgal}$ for *DGD,* since they correspond to the achievable accuracy of GRACE as derived in chapter 2. Figure 5.6 displays the statistics of the solution errors. The value of the standard deviation varies between 2 and 9 $\mathrm{m^2/s^2}$ with an average value of 3 $\mathrm{m^2/s^2}$. The relative error varies from 8 to 40 % of the signal with an average value of 20%. These results agree with the relationships of Figure 5.4.

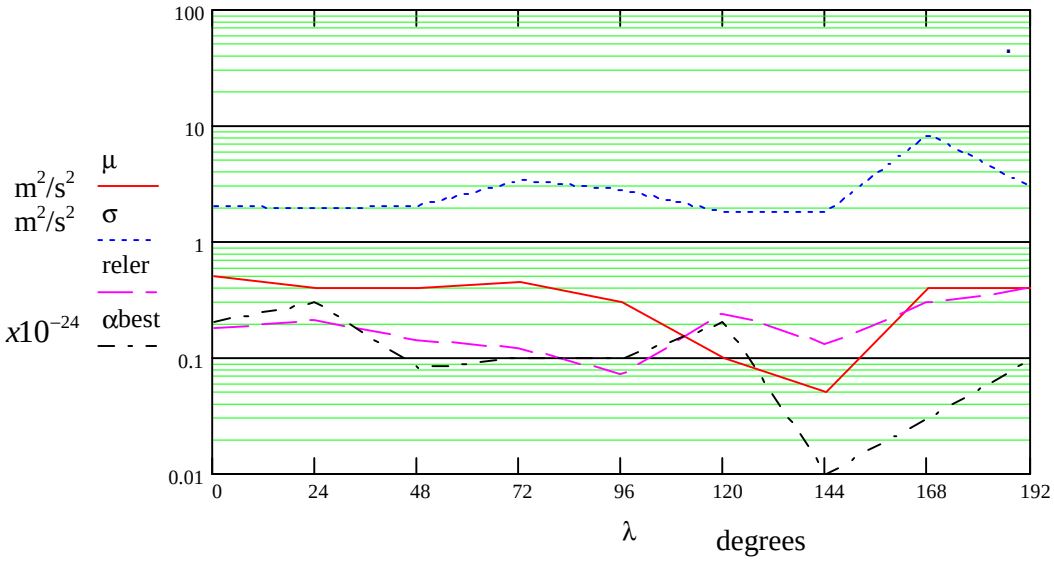

Figure 5.6: Solution errors and regularization parameters for different locations with respect to longitude for the *DT* kernel, H=400 km, sampling interval of $0^o.8$ and for 24^o square area. $\phi_m = 51^o$. Only random errors affect the solution (no model errors).

5.1.2.2 Model Errors

Now, we analyze regularization performance considering also model errors. That is, generating measurements at orbit altitude and then adding random noise and solving for *T* according to equation (4.39). In the solution of ill-posed problems, model errors are difficult to quantify due to the regularization required. This is not a problem for the direct process and it is illustrative to compare the associated model errors with data errors in this case. Figures 5.7 and 5.8 show the errors of computing *DT* and *DGD*, respectively, at 400 km altitude from errorless *T* values at ground level with $0^o.4$ sampling interval for different areas. Both Figures plot the standard deviation of errors for the central 4^o square area in terms of the data area size (plots a) and the corresponding relative errors (plots b). Two areas with different geographical location were tested. For instance, we can see that for both data types an area of 24^o square produces relative errors of about less than 5% and standard deviation of about 0.01-0.05 m^2/s^2 and 0.004-0.01 mgal, respectively, for *DT* and *DGD*. The related edge effect is relatively large. For instance, for the *DT* values computed for the area located at latitude 48^o, the total standard deviation of the errors of the whole grid was 0.8 m^2/s^2 with a mean value of 0.2 m^2/s^2. Figure 5.9 shows these errors. Figure 5.10 shows the errors of *DGD* obtained for the same area. The mean and standard deviation are, respectively, 0.06 and 0.26 mgal.

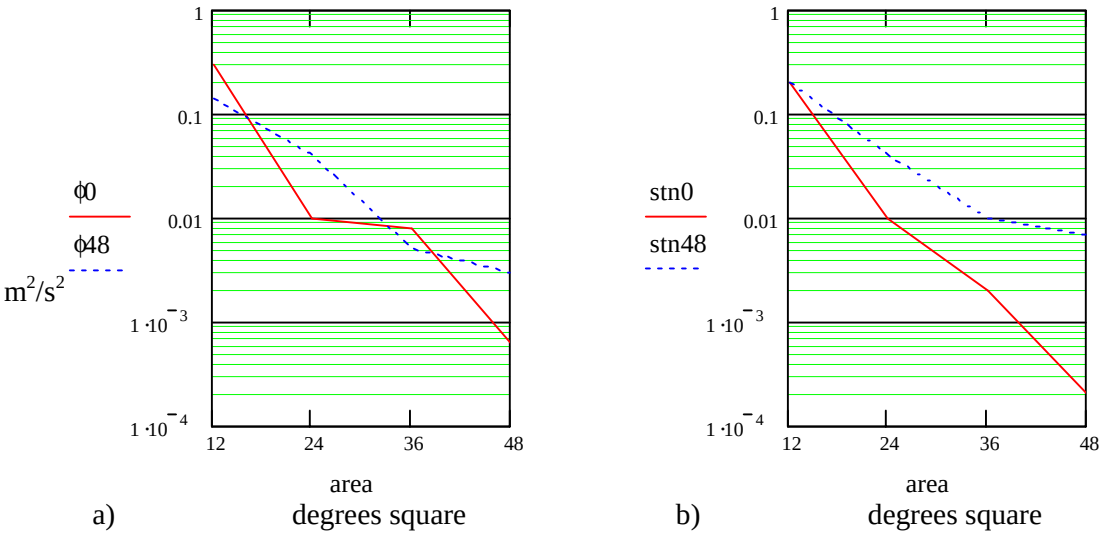

Figure 5.7 a) Standard deviation and b) relative errors on *DT* at 400 km altitude computed from *T* at the ground using different area coverage with $0^o.4$ sampling interval. Results for central 4^o square area. For two locations, at the equator and at latitude 48^o.

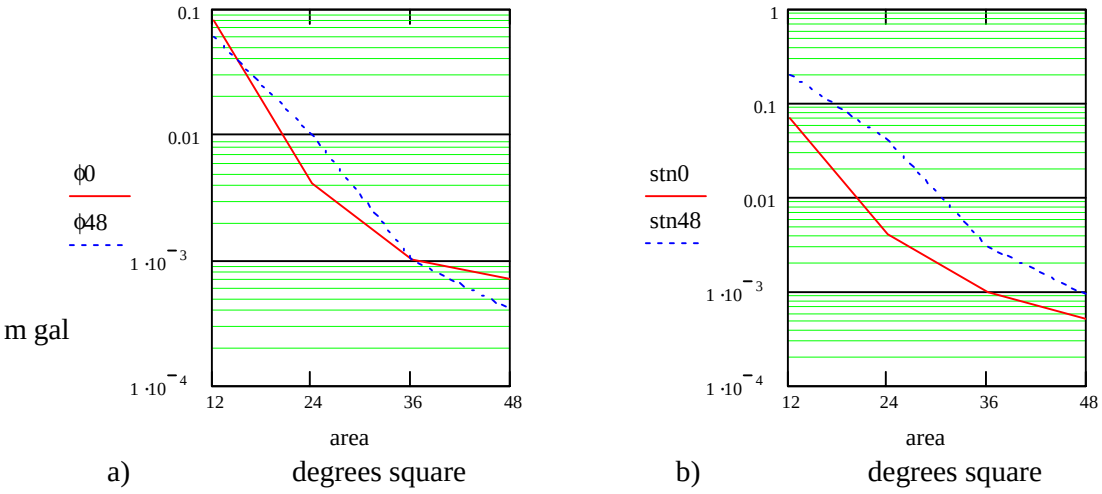

Figure 5.8 a) Standard deviation and b) relative errors in DGD at 400 km altitude computed from errorless *T* at ground level using different area coverage with $0^o.4$ sampling interval. Results are for central 4^o square area, at the equator and at latitude 48^o.

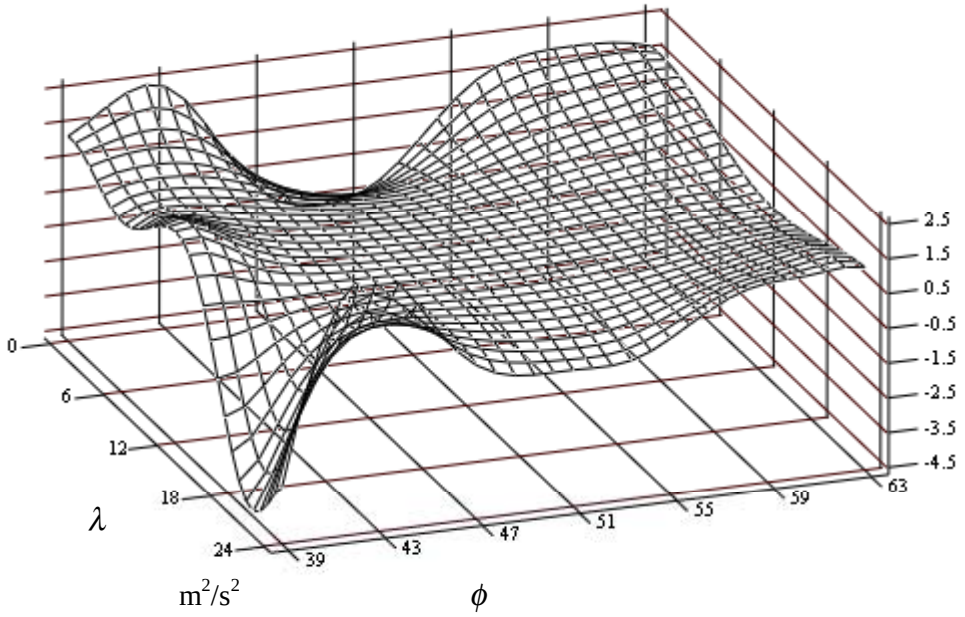

Figure 5.9: Errors of *DT* computed from errorless *T* at ground level with $0^{o}.8$ sampling interval.

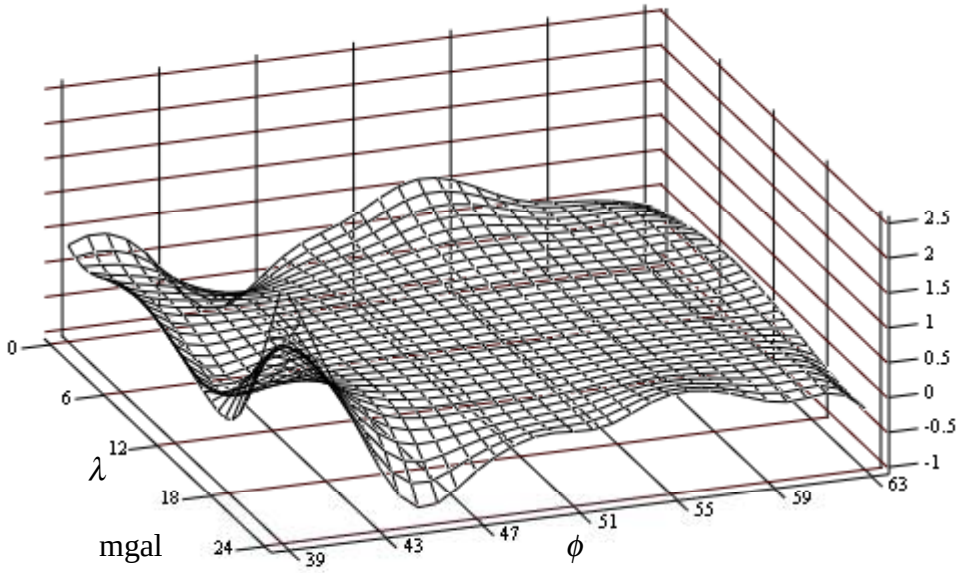

Figure 5.10: Errors of *DT* computed from errorless *T* at ground level with $0^{o}.8$ sampling interval.

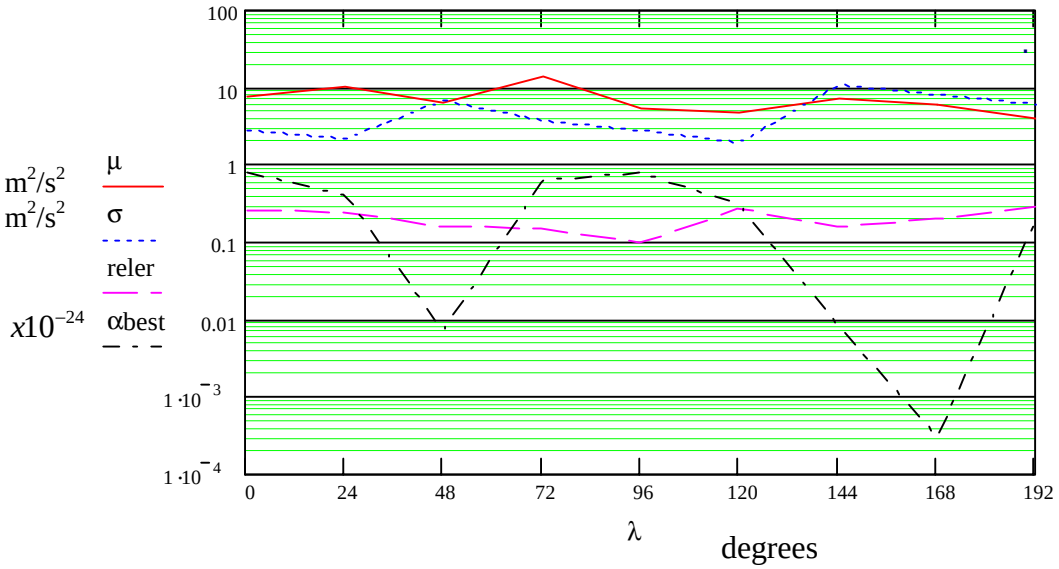

Figure 5.11: Solution errors and best α for different geographical locations with respect to longitude for the *DT* kernel, H=400 km, sampling interval of $0^o.8$ and for 24^o square area. $\phi_m = 51^o$, using EGM96(20-180). Only model errors affect the solution.

For all of our regularization tests, when considering model errors, the error analysis will be made for the central 4^o square area in order to avoid model errors associated mainly with the edge effects.

Larger errors (than in the case of only measurement error case) are obtained for the regularized downward continuation solution of *T* from *DT* when considering only model errors and the data configuration corresponding to Figure 5.6. Large mean values where also observed. The results for the central 4^o area are displayed in Figure 5.11. The average standard deviation and relative error are 5.0 m^2/s^2 and 20%. Thus, in the average, the standard deviation is almost twice as large as when only random noise affects the solution. The mean value varied from 4 to 11 m^2/s^2 with an average of 6.8 m^2/s^2. On the other hand, the average value of α was $3x10^{-25}$, whereas in the previous test it was of $1x10^{-25}$.

5.1.2.3 Edge Effect and Truncation Errors

Two problems related to the evaluation or inversion of discretized integrals restricted to a region are the edge effect and the truncation error. One way to deal with the edge effect is to disregard solution points near the edges. For the present tests, this effect seems to be severe, as we can see from Figures 5.12 and 5.13 where plots of the errors in *T*, obtained from *DT* in two different geographical locations, show values larger than 100 m^2/s^2 near the edges with a total standard deviation of about 48 m^2/s^2 in both figures. This is also

corroborated by Table 5.1 in Section (5.2.2) where some of the standard deviations corresponding to the total area are even larger than 48 m^2/s^2.

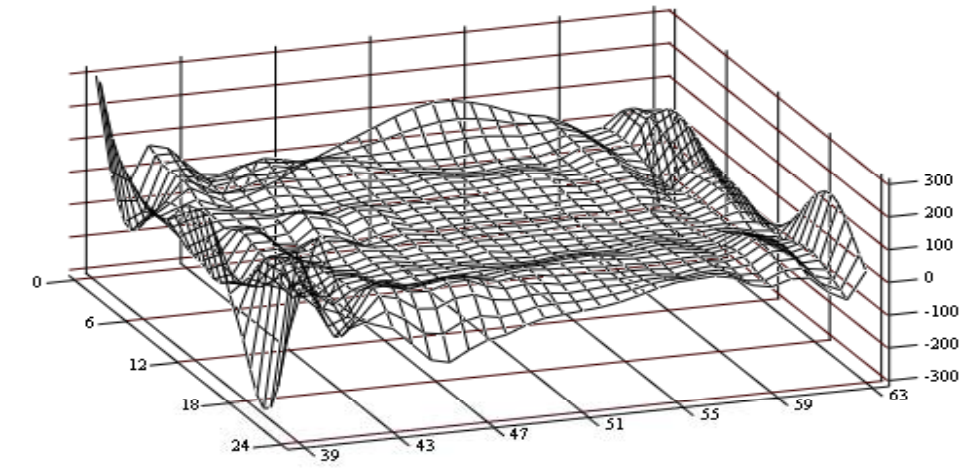

λ

m^2/s^2 ϕ

Figure 5.12: Plot of solution errors in *T* using *DT* with $\alpha = 8x10^{-25}$, H=400 km, sampling interval of $0^o.8$ and 24^o square data. $\phi_m = 51^o$, $\lambda_0 = 0^o$, using EGM96(20-180).

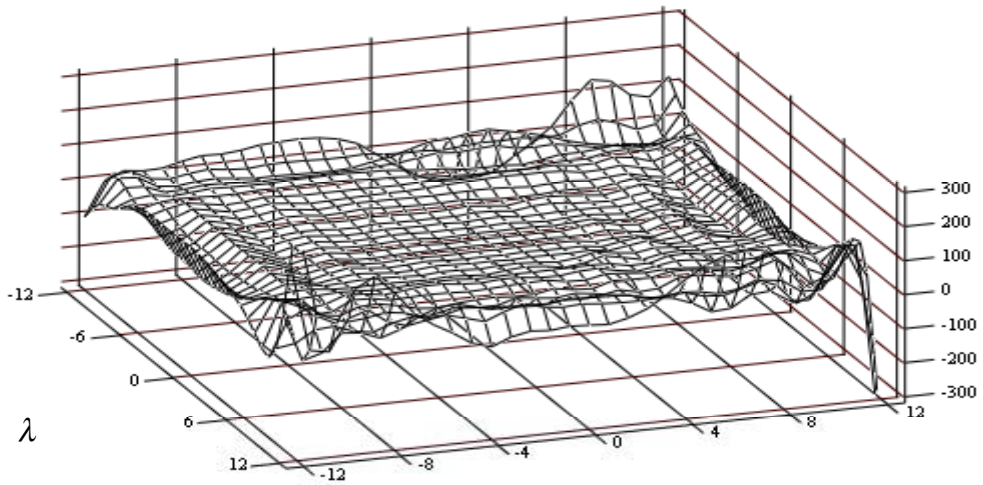

λ

m^2/s^2 ϕ

Figure 5.13: Plot of solution errors in *T* using *DT* with $\alpha = 8 \cdot 10^{-25}$, H=400 km, sampling interval of $0^o.8$ and 24^o square data. $\phi_m = 0^o$, $\lambda_0 = 0^o$, using EGM96(20-180).

One common practice to reduce the truncation errors is to subtract a reference field from the measurements according to equation (3.25). Another way to reduce this type of error is to follow Meissl's modification and Molodensky's truncation theory (see for instance Jekeli, 1981), which consist in modifying the kernel to reduce the Gibbs' phenomenon. However, this may not be as effective when dealing with differences of kernels since they are not symmetric and isotropic. Therefore, the simple remove/restore method is the only method considered here to reduce truncation errors for the kernels involved in this analysis.

5.1.2.4 Considering Model and Measurement Errors

Next, we obtained the regularized downward continuation solution of *T* from *DT* considering both model and random errors and the data configuration corresponding to Figures 5.6 and 5.11. The results for the central 4^o area are displayed in Figure 5.14. The average value obtained for the standard deviation and relative value of the errors were 5.9 m^2/s^2 and 23% respectively, which are slightly larger than the only model error case. The mean value varied from 1 to 11 m^2/s^2 with an average of 6 m^2/s^2. On the other hand, the average value of α was $6x10^{-25}$.

The same test, considering random and model errors, was repeated for the *DGD* kernel (Figure 5.15). The estimation errors obtained are similar as those from *DT*. The averages of the standard deviation and mean of the errors are 5.3 and 8.7 m^2/s^2, respectively. The average value of the relative error is 24%.

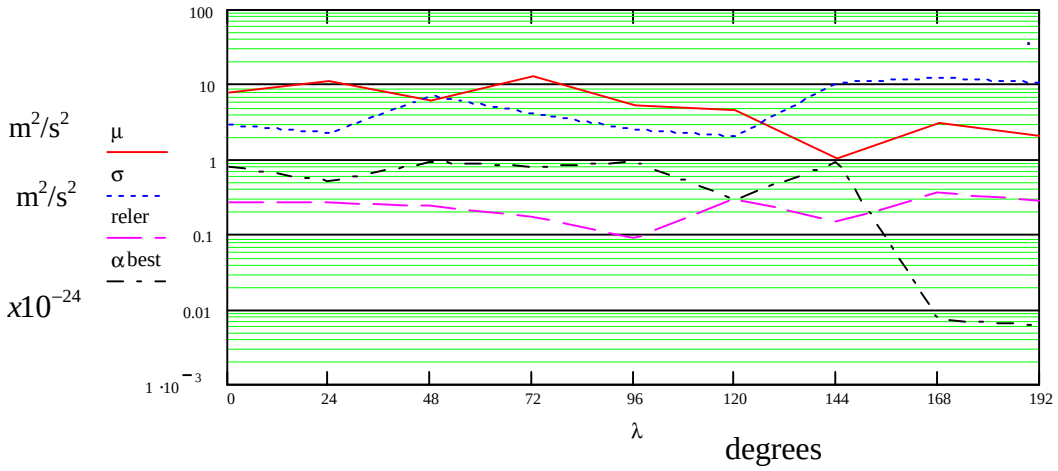

Figure 5.14: Solution errors and best α for different geographical locations with respect to longitude for the *DT* kernel, H=400 km, sampling interval of $0^o.8$ and for 24^o square area. $\phi_m = 51^o$, using EGM96(20-180). Both random and model errors affect the solution.

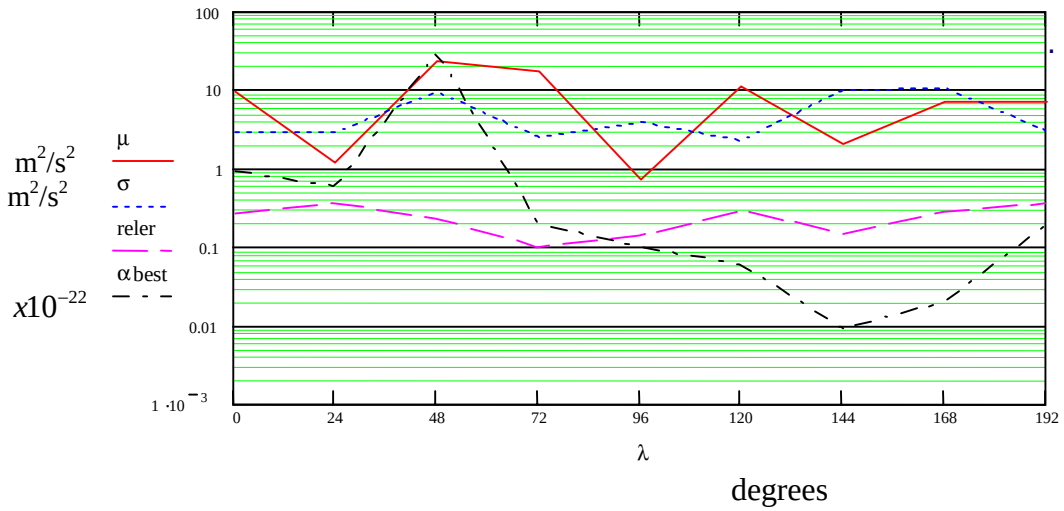

Figure 5.15: Solution errors and optimum α for different geographical locations with respect to longitude for *DGD* kernel, H=400 km, sampling of $0^o.8$ and for 24^o square area. $\phi_m = 51^o$, using EGM96(20-180). Both random and model errors affect the solution.

From tests made so far, we could conclude that our systems are ill-conditioned for the GRACE operational altitude (300-500 km), as seen in Figure 5.1. To some extend, the ill-condition of the systems is also affected by sampling interval and size of the integration area. The smaller the data separation, the more unstable the system. The same can be observed with the increase of the integration area (see Figure 5.2).

Some of the results obtained indicate that, for a given grid of points being regular with respect to latitude and longitude, the ill-posedness tends to increase toward the polar regions due to the meridian convergence, which brings the points closer along parallels. Using the same configuration as for Figure 5.1, relatively small variation resulted in going from the equator to 80^o latitude for both kernels as seen in Figure 5.3.

For the systems analyzed here, requirements on data accuracy seems to be very demanding. For instance, errors smaller than $1x10^{-5}$ m^2/s^2 are required on *DT* to obtain solution errors of the level of 1 m^2/s^2 with a relative error of about 10 % with respect to the signal (see Figure 5.4). However, the solution is not very sensitive to measurement errors, since 0.01 m^2/s^2 error in *DT* yields solution errors of about 2 m^2/s^2.

Apparently, model errors seem to introduce also large mean values in the errors of both, *T* using *DT* and *DGD*. For a 24^o square area of integration, the mean value of the errors in *T* is about 5 m^2/s^2 for both *DT* and *DGD* kernels, see Figures 5.11, 5.14, 5.15 and Table 5.1.

5.2 Some Analysis on Regularization Performance

5.2.1 Solution Errors in terms of Altitude

As the ill-condition of the system increases with altitude as seen in Figure 5.1, so will the solution errors. This can also be appreciated in Figure 5.16 which displays the best solution of *T* obtained from *DT* and *DGD* measurements given at different altitudes in the 300-500 km range. In both cases, the errors in the central region increase from about 1 m^2/s^2 at 300 km to 3.5 m^2/s^2 at 500 km. The Figure also plots the errors for the total area which area considerably larger, ranging from about 40 m^2/s^2 at 300 km to 58 m^2/s^2 at 500 km, mainly due to the edge effect.

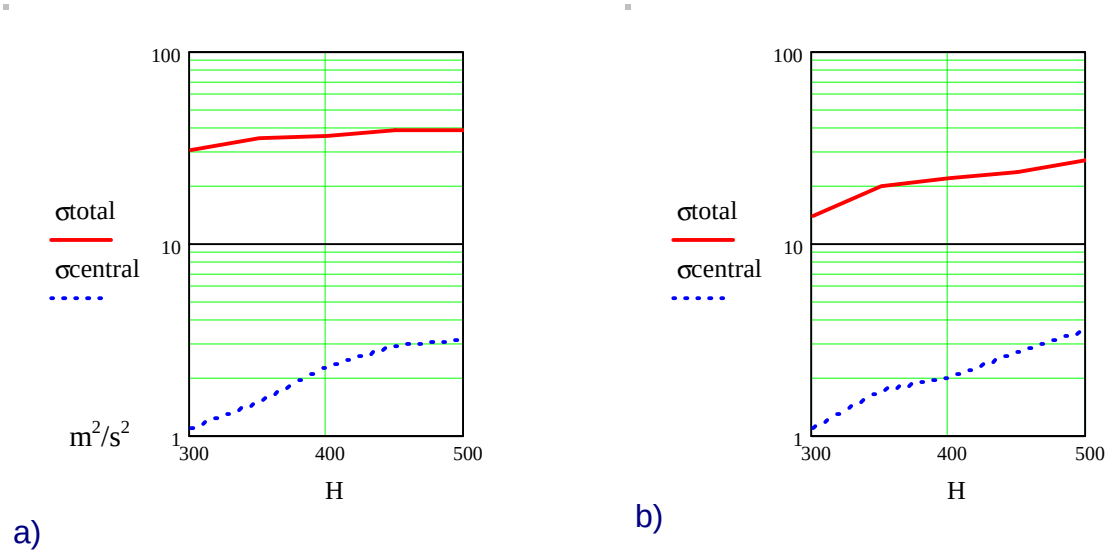

Figure 5.16: Solution errors in term of altitude H for central area (σcentral) 4^o square and the total area (σtotal). Kernel: a) *DT* and, and b) *DGD;* sampling of $0^o.8$ and for 24^o square data. $\phi_m = 51^o$; $\lambda_0 = 0^o$; EGM96(20-180).

5.2.2 Solution Errors in terms of Sampling Interval

We now look at the error behavior with respect to sampling interval. Considering the same configuration, but with H = 400 km, we solve for *T* using different sampling intervals. The results are displayed in Table 5.1. The standard deviation of the central area increases systematically from 2.2 m^2/s^2 at $0^o.2$ interval to 3.5 m^2/s^2 at $1^o.2$ interval. As expected, more regularization is required as the sampling interval decreases. The α-value also decreases from $3x10^{-24}$ to $1x10^{-25}$ as the sampling interval increases from $0^o.2$ to $1^o.2$. In Figure 5.14 we display the error variations in terms of α for solutions using the intervals $0^o.4^o$, $0^o.8$ and $1^o.2$. The three plots show that a displacement of one order of magnitude of α with respect to its best value can increase the solution error more than 1

m^2/s^2. The same pattern was observed when using *DGD* as measurements, with 0.01 mgal level of random noise, as can be seen on Figure 5.15.

Sampling interval	Solution Errors m^2/s^2				Rel Error. Central area	α_{best}
	Central area		Total Area			
	mean	stdev	mean	stdev		
0.2^o	7.5	2.2	6.5	48	0.20	$3x10^{-24}$
0.4^o	7.6	2.5	6.5	49	0.22	$1x10^{-24}$
0.6^o	7.7	2.7	6.6	49	0.24	$8x10^{-25}$
0.8^o	7.7	2.9	6.8	48	0.26	$5x10^{-25}$
1.0^o	7.9	3.3	7.1	66	0.3	$3x10^{-25}$
1.2^o	8.1	3.5	7.5	88	0.32	$1x10^{-25}$

Table 5.1: Errors in *T* regularized solution in terms of sampling interval and the corresponding regularization parameter for H = 400 km and from *DT*. Central area corresponds to 4^o square.

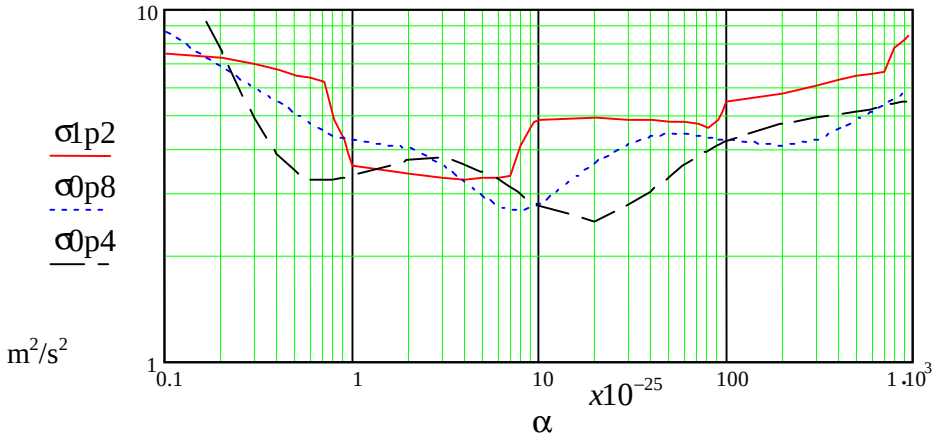

Figure 5.17: Errors in terms of α for different sampling intervals ($0^o.4$, $0^o.8$, 1.2^o), using *DT* kernel, H=400 km, for 24^o square area. $\phi_m = 51^o$, $\lambda_0 = 0^o$, using EGM96(20-180).

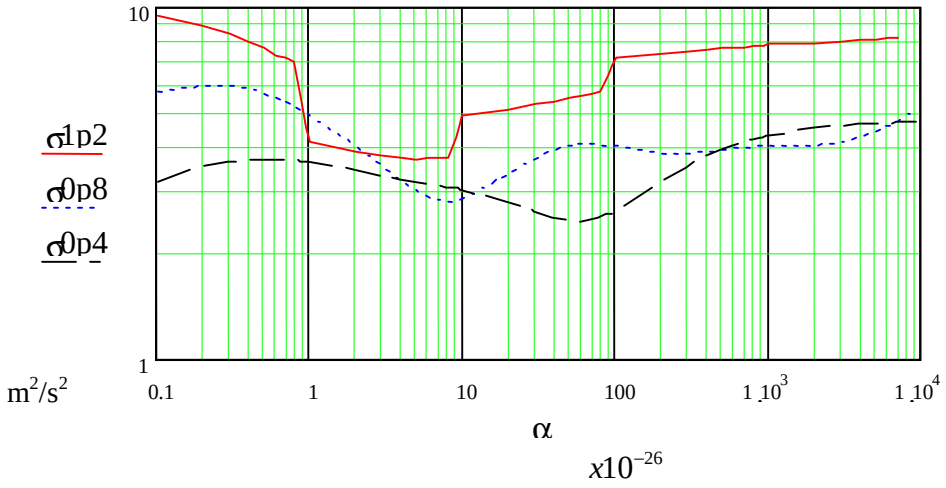

Figure 5.18: Errors in T in terms of α for different sampling intervals; $0^o.4$, $0^o.8$, $1^o.2$, using *DGD* kernel, H=400 km, for 24^o square area. $\phi_m = 51^o$, $\lambda_0 = 0^o$, using EGM96(20-180).

5.2.3 Solution Errors in terms of Area Coverage

The third main factor affecting a system's ill-condition as analyzed before is the area coverage. For this factor we considered three different area sizes; 12^o, 24^o and 36^o squares with $0^o.8$ sampling interval. The ill-posedness tends to increase with the area. This fact is supported by Figures 5.19 and 5.20. In the first Figure, we have the solution of T obtained from *DT*. The best α-values obtained were $0.75x10^{-25}$, $7.5x10^{-25}$, and $20x10^{-25}$ for the three area sizes, respectively. The corresponding estimation errors were 3.6, 2.7, and 2.1 m^2/s^2. In Figure 5.20 we have the solution of T obtained from *DGD*. The best α-values obtained were $3x10^{-26}$, $8x10^{-26}$, and $95x10^{-26}$ for the three area sizes, respectively. The corresponding error values were 4.7, 2.8 and 2.6 m^2/s^2 respectively.

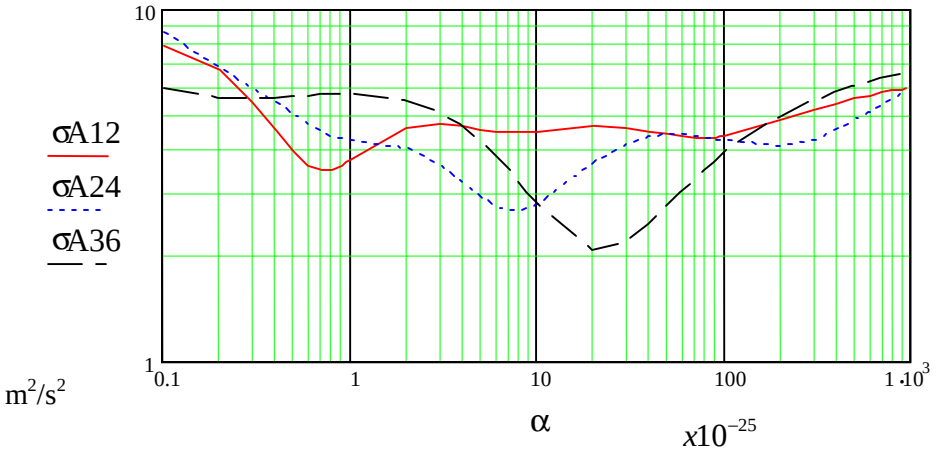

Figure 5.19: Errors in terms of α for different areas of data; 12°, 24° and 36° squares, using *DT* kernel, H=400 km, for 24° square area. $\phi_m = 51^o$, $\lambda_0 = 0^o$, using EGM96(20-180).

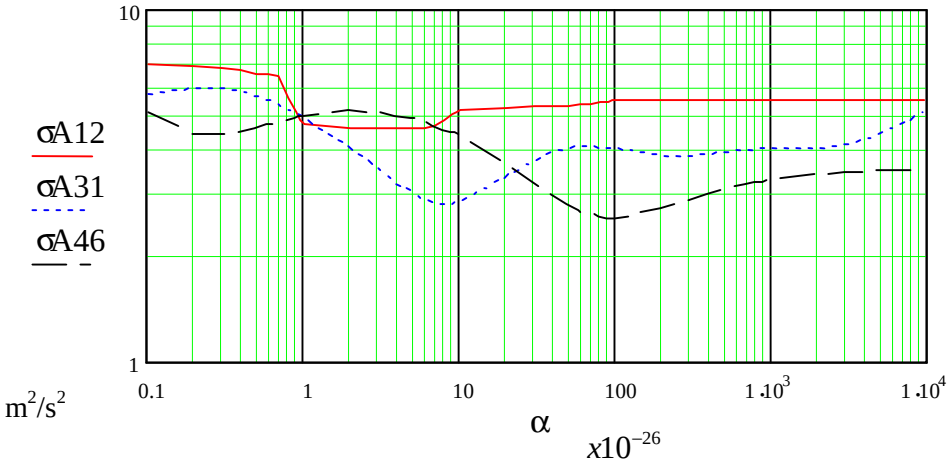

Figure 5.20: Errors in *T* in terms of α for different areas of data; 12°, 24° and 36°, using *DGD* kernel, H=400 km, for 24° square area. $\phi_m = 51^o$, $\lambda_0 = 0^o$, using EGM96(20-180).

5.2.4 Effect of nmax variations of reference field

As mentioned in the previous section, one way to diminish effects of truncation errors due to the limited integration area is by employing the remove/restore technique, which implies not considering the lower frequencies of the signal in the downward continuation process.

Now, we do some analysis of the effect in the regularized solution errors by varying the maximum degree and order of the reference field subtracted. The regularization was performed with different degrees of reference field subtracted from the measurements. It was observed that, by increasing the maximum degree of this field from nmax = 20 to nmax = 40 the errors were reduced by up to 1 m^2/s^2 in our tests as seen in Figures 5.21 and 5.22. Figure 5.21a displays the solution errors with nmax = 20, 30, 40 in terms of α. We can see from the graph, that the lower the nmax the larger is the error, ranging from about 1.7 to about 2.7 m^2/s^2. Similarly, when using *DGD* the error ranged from 1.8 to 2.8 m^2/s^2 as shown in Figure 5.22a. Nonetheless, the relative errors do not show a systematic decrease or increase with nmax variation for both type of kernels (see Figures 5.21b and 5.22b).

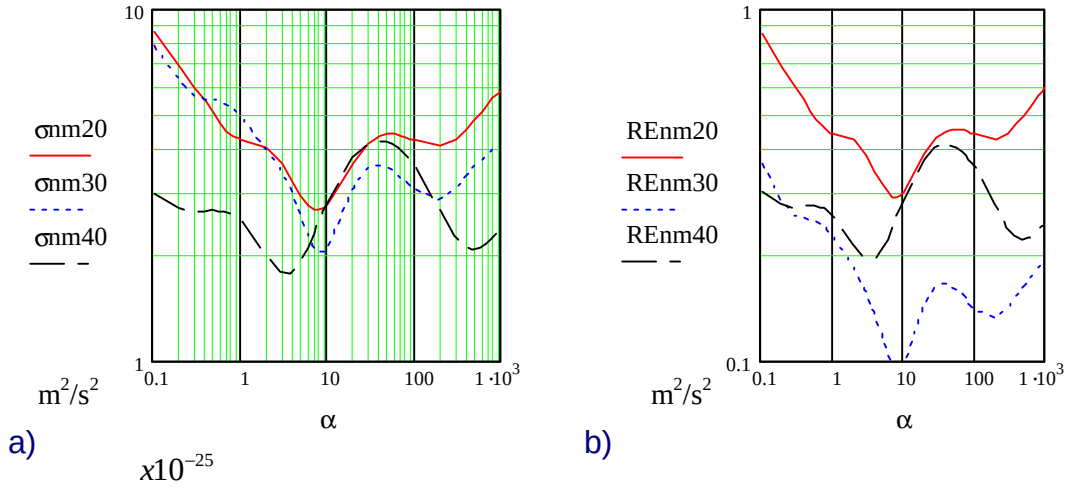

Figure 5.21: a) Standard deviation and b) relative errors in *T* in terms of α for different reference fields (nmax = 20,30,40), using *DT* kernel, H=400 km, for 24^o square area. $\phi_m = 51^o$, $\lambda_0 = 0^o$, using EGM96(20-180).

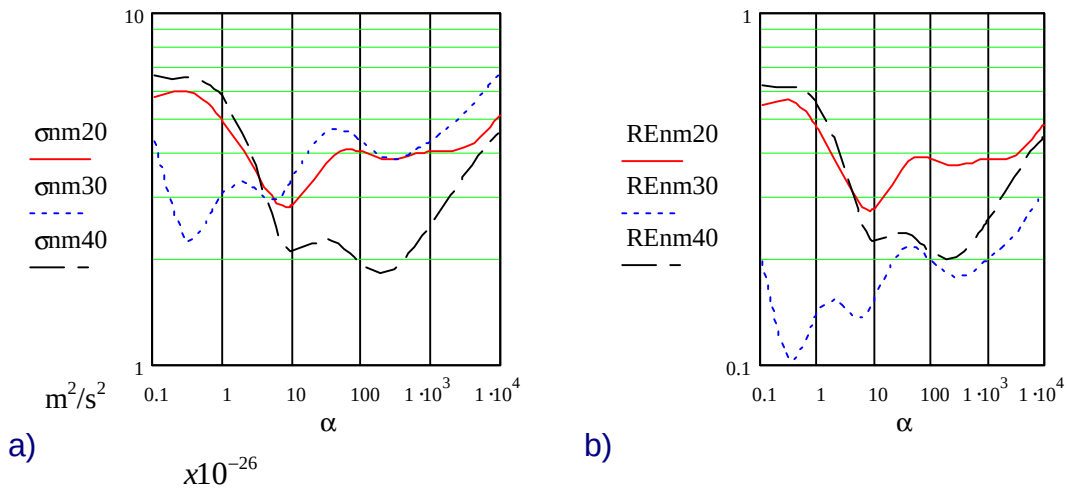

Figure 5.22: a) Standard deviation and b) relative errors in T in terms of α for different reference fields (nmax = 20,30,40), using *DGD* kernel, H=400 km, for 24^o square area. $\phi_m = 51^o$, $\lambda_0 = 0^o$, using EGM96(20-180).

Tests have been made in this section to analyze the solution accuracy in terms of variations in sampling interval, integration area and altitude. For all these cases, the solution errors increase together with the ill-condition of the system, see Table 5.1 and Figures; 5.16, 5.17, 5.18, 5.19 and 5.20.

With respect to solution errors in terms of maximum degree and order of the reference field subtracted from both types of measurements, the solution errors tend to decrease as the nmax increases. However, this was not observed with the relative errors as shown by Figures 5.21 and 5.22.

5.3 Interpolation Errors

In this study, for simplicity in the analysis and computations and to be able to use the traditional fast Fourier transform, it is assumed, as mentioned before, that measurements are given on a regular grid with respect to geographical coordinates at a constant altitude H with respect to a boundary that approximates the Earth's surface. Furthermore, it is also assumed that both satellites fly with a constant angular central distance between them and along meridians, that is, a constant orientation. In order to generate this type of geometrical data configuration from measurements produced over real orbits, some interpolations and extrapolations will be required. We now analyze the associated interpolation and/or extrapolation errors.

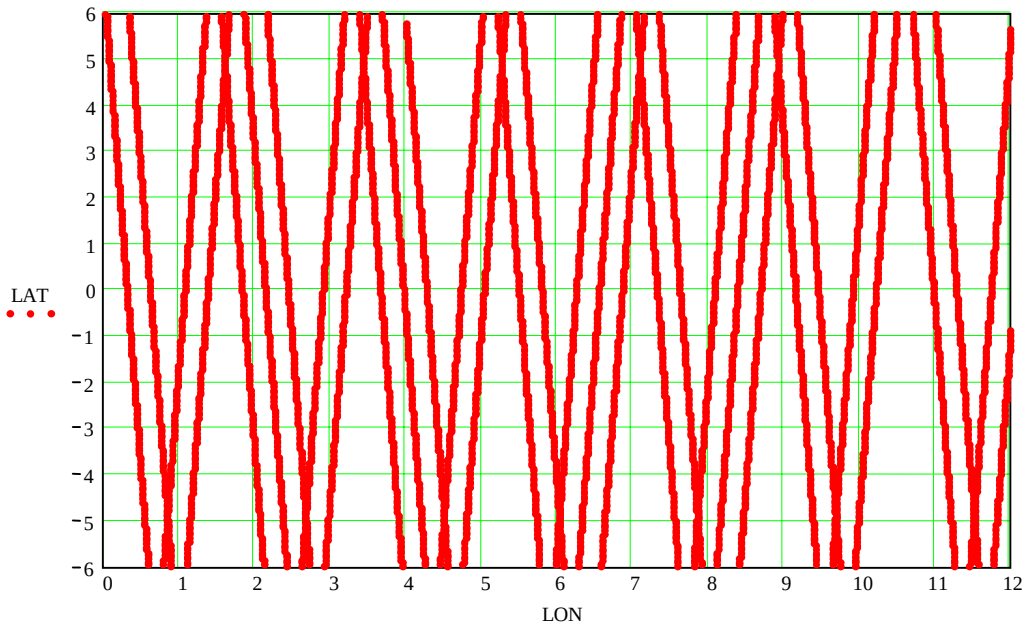

Figure 5.23: Ground track of a 30-day GRACE-type Keplerian orbit at about 430 km of altitude. For a 12^{o} square window in the equatorial area.

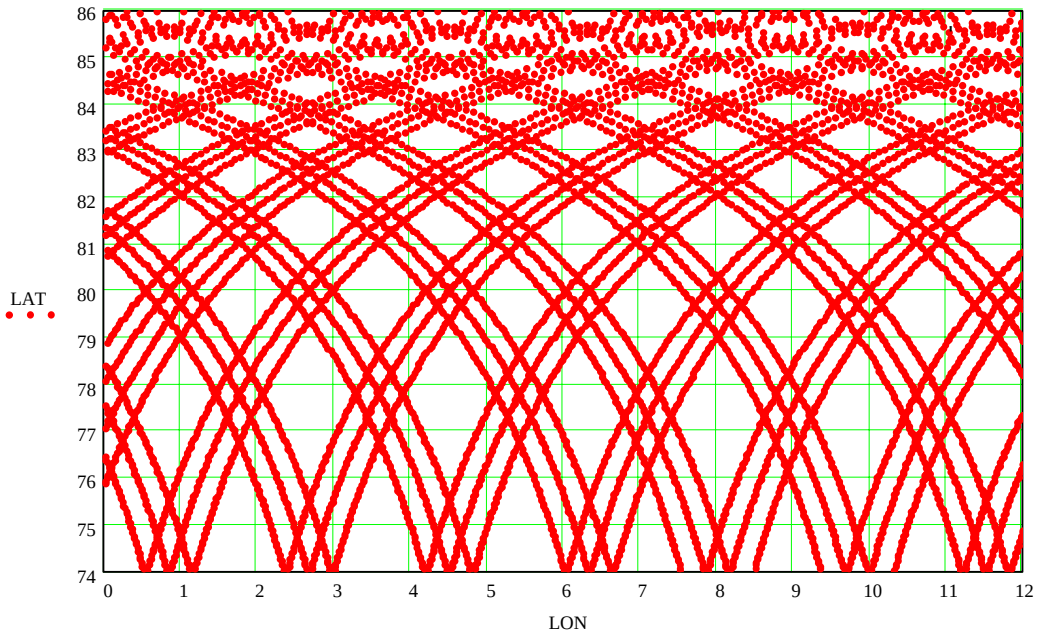

Figure 5.24: Ground track of a 30-day GRACE-type Keplerian orbit at about 430 km of altitude. For a 12^{o} square window in the near pole area.

5.3.1 Interpolation to a Regular Grid

First, to estimate errors in interpolating to a regular grid with respect to latitude and longitude, we generated a 50-day circular Keplerian orbit with 89^o inclination and radius of 6771 km that corresponds to an altitude of 430 km; the sampling rate for the output was 1 Hz (although GRACE output is 0.1 Hz). A real orbit will produce a data distribution that will deviate from a regular latitude-longitude grid approximately as does a Keplerian orbit, although the Keplerian orbit produces regularity in longitude. We computed values of *DT* and *DGD*, with the same assumptions considered so far, at the points generated by the orbit. In 12^o square windows at different latitudes the potential differences were interpolated to a regular grid of $0^o.4$ interval in both directions. The interpolation was done with a cubic spline approximation, using the Delawny triangulation method, and considering 30, 40 and 50-day data. The respective rms distances of interpolation were about $0^o.2$, $0^o.15$, and $0^o.12$. Figures 5.23 and 5.24 show the data for 30-day orbit for the window in the equator and near the pole.

Days Of orbit	Number of Seconds	Central latitude of areas Number of points in each area				
		0	20	40	60	80
30	2592000	5809	5983	6428	7049	10809
40	3456000	7702	8186	8460	9250	14396
50	4320000	9505	9849	10440	11537	17844

Table 5.2: Data generated for each interpolation window of 12^o square for 30, 40 and 50-day Keplerian orbit.

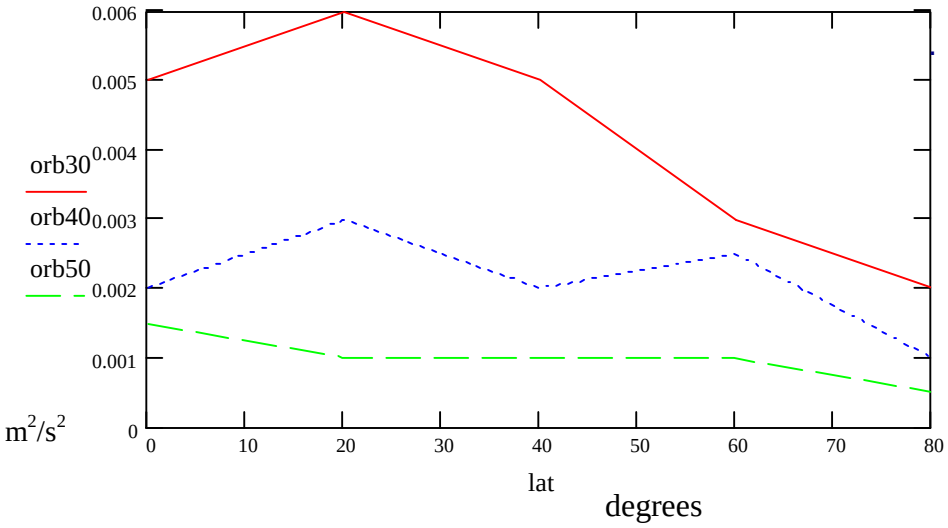

Figure 5.25: Errors in interpolation of *DT* to a regular grid of $0^o.4$ interval from data generated by 30, 40 and 50-days orbits over 12^o square areas at different latitudes.

In order to analyze errors in interpolating to a regular grid with respect to latitude and longitude, windows at different latitudes, from the equator to the 80^o parallel were considered for the data. Table 5.2 displays the number of points obtained for each interpolation window and the orbit duration. We can see that the number of points increases as the data window moves toward the pole. For instance, for the 30-day orbit the number of points is 5860 at the equator and 10809 at 80^o latitude. On the other hand, the number of points generated at the equator increases to 9505 for a 50-day orbit. The interpolation errors obtained were relatively small as shown by Figures 5.25 and 5.26. Figure 5.25 shows the interpolation errors for *DT* measurements. The errors decrease almost systematically toward the pole, but within the same order of magnitude. For example, with a 40-day orbit they range between 0.003 m^2/s^2 and 0.001 m^2/s^2 at latitude 80. The improvement with latitude is expected since more data are generated in the polar region due to the meridian convergence, as shown in Table 5.2. The improvement of interpolation with a 50-day orbit compared to a 30-day orbit is significant. For instance, at mid-latitude a 30-day orbit produced interpolation errors of about 0.005 m^2/s^2, half of the standard deviation in the measurement error adopted in this study; whereas a 50-day orbit yielded 0.001 m^2/s^2 interpolation error, which is 5 times smaller. A similar situation was observed when interpolating *DGD* values. As in the *DT* case, errors also generally decrease toward the pole. Next, random noise of 0.01 m^2/s^2 and 0.01 mgal was added, respectively, to the *DT* and *DGD* values and then the same interpolation procedure was applied. The errors of the interpolated values obtained tend to decrease with respect to both latitude and number of data points as shown by Figures 5.27 and 5.28.

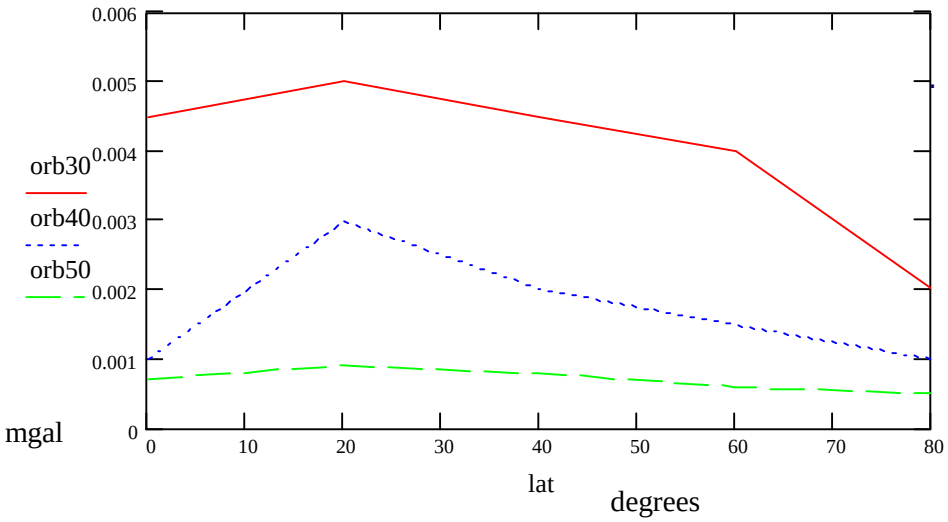

Figure 5.26: Errors in interpolation of *DGD* to a regular grid of $0^o.4$ interval from data generated by 30, 40 and 50-day orbits over 12^o square areas at different latitudes.

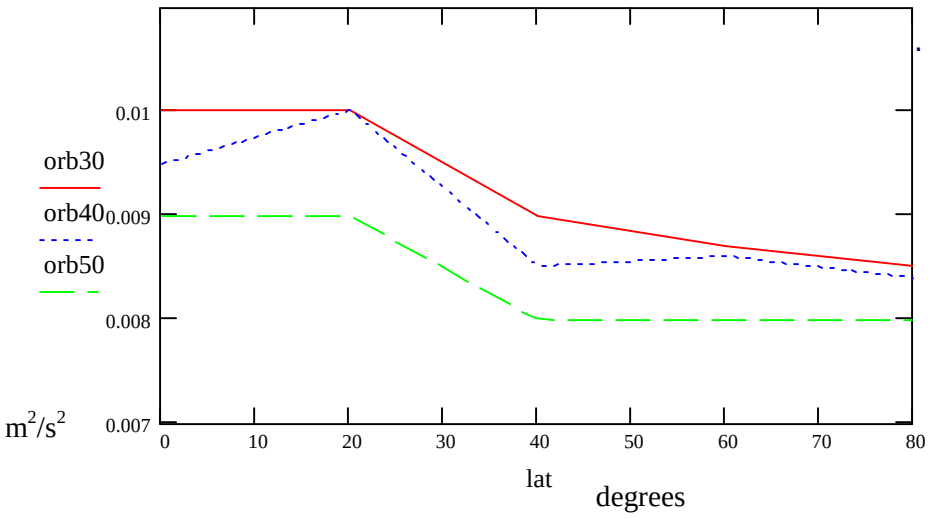

Figure 5.27: Errors in interpolation of *DT* to a regular grid of $0^o.4$ interval from data generated by 30, 40 and 50-day orbits over 12^o square areas at different latitudes. Random noise was added to the measurements.

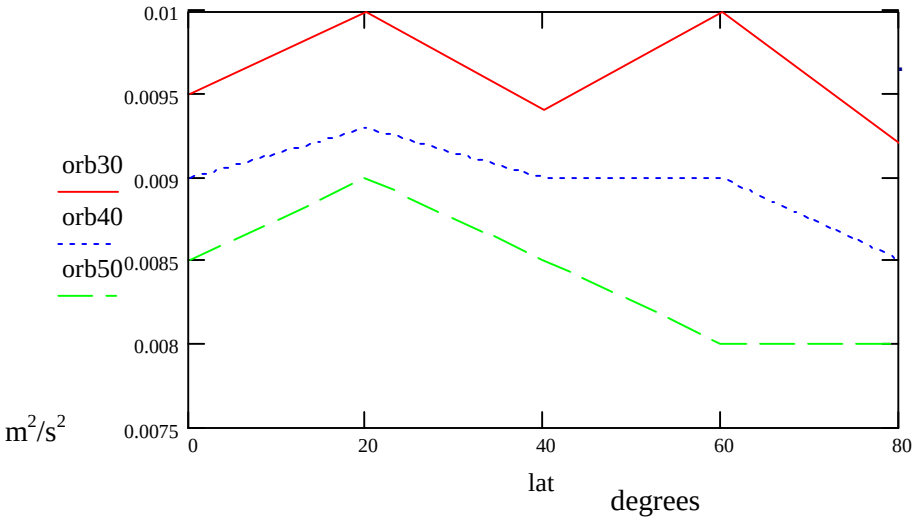

Figure 5.28: Errors in interpolation of *DGD* to a regular grid of $0^o.4$ interval from data generated by 30, 40 and 50-day orbits over 12^o square areas at different latitudes. Random noise was added to the measurements.

5.3.2 Interpolation to same Altitude and Intersatellite Distance

For the analysis of errors of interpolation to the same altitude and inter-satellite distance we generated orbits for both satellites employing the spherical harmonic model of the geopotential, EGM96, up to degree and order 180 by means of numerical orbit integration according to the Adams-Cowell multistep predictor-corrector algorithm. Again, the satellite's state vector was produced at one-second intervals. The initial parameters of the orbits were 400 km altitude above the Earth's mean radius, zero eccentricity, and 89^o inclination. The initial inter-satellite distance was 230 km. We chose a 200-second orbital of arc (about 12^o along the meridian) at different latitudes. At every epoch, the *DT* and *DGD* values related to the actual locations of both satellites were computed using the EGM96 geopotential model up to degree and order 180.

Type of interpolation	Initial latitude of each segment Standard deviation of interpolation errors m^2/s^2			
	0	20	45	75
To same H	$1x10^{-4}$	$4x10^{-4}$	$1x10^{-4}$	$4x10^{-4}$
To same ρ_{12}	$2x10^{-4}$	$2x10^{-3}$	$2x10^{-4}$	$5x10^{-3}$

Table 5.3: Errors of interpolating *DT* from 12^o arcs at different latitude to same altitude and intersatellite distance using LSC.

Type of interpolation	Initial latitude of each segment Standard deviation of interpolation errors (mgal)			
	0	20	45	75
To same H	$2x10^{-4}$	$3x10^{-4}$	$1x10^{-4}$	$3x10^{-4}$
To same ρ_{12}	$3x10^{-4}$	$1x10^{-3}$	$4x10^{-4}$	$5x10^{-3}$

Table 5.4: Errors of interpolating *DGD* from 12^o arcs at different latitude to same altitude and intersatellite distance using LSC.

Next, the computed observables were interpolated to the same mean inter-satellite distances and mean altitude of satellites. LSC was used according to equations (4.61) and (4.63) to interpolate the data to the desired regular configuration. The covariance matrices employed were based on the degree variance as computed with equation (4.54) and using the spherical harmonic coefficients of the EGM96 geopotential model limited to degree and order 20-180.

Tables 5.3 and 5.4 show the results for the different arcs, considering *DT* and *DGD* as measurements, respectively. Both types of measurements produced similar interpolation errors. Also both type of interpolation yielded similar errors. The interpolation errors of *DT* were of the order of 10^{-4} m^2/s^2 with respect to H for all latitudes considered and ranged from $2x10^{-4}$ m^2/s^2 at the equator to $5x10^{-3}$ m^2/s^2 at 75^o latitude with respect to intersatellite distance. One fact that can be appreciated is that all errors are relatively small near the equator ($\leq 2x10^{-3}\, m^2/s^2$).

In the interpolation to same altitude, the r.m.s. of the differences of the true H's with respect to the average H was about 100 m for all arcs considered. However, data generated over an area will consist of orbit arcs with much larger height variations with respect to each other. In order to have a better assessment about the errors associated with the extrapolation of the measurements to the same altitude, a 10-day orbit was generated using the EGM(2-180) field. The elevations of *DT* values generated over a 10^o square area at the equator had an average of about 400 km with a standard deviation of 4 km. Then, the same interpolation procedure, using LSC, was applied to data produced over one orbital arc of about 12^o. The *DT* values were then extrapolated to different altitudes below and above the data mean altitude. Figure 5.29 shows the extrapolation errors obtained. The errors increase steadily as the extrapolation altitude moves away from the mean elevation. We can see from the figure that for 4 km extrapolation the errors are about half the magnitude of the measurement errors considered in this study (0.01 m^2/s^2). Nevertheless, smaller extrapolation errors could be expected when considering more data in the process.

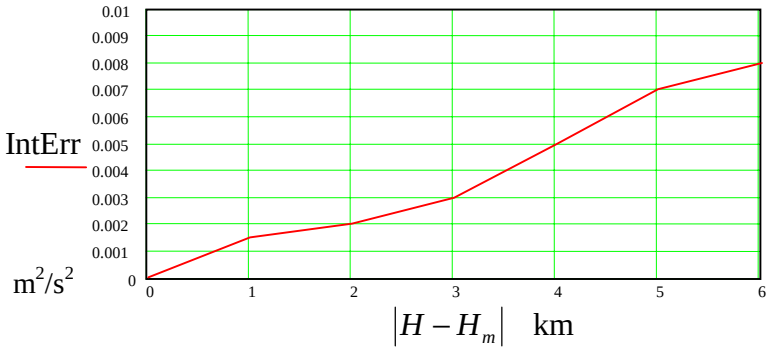

Figure 5.29: Errors in extrapolating *DT* values to same attitude in terms of height difference between the mean H = 400 km and the H of extrapolation.

5.4 Performance of Regularization Methods

In chapter 4, we discussed some of the more popular regularization methods. Beside the Tikhonov method, which we have considered so far, other methods are the conjugate gradient (GC) method, the truncated singular value decomposition (TSVD) method, and the damped singular value decomposition (DSVD) method; see equations (4.48), (4.49) and (4.77).

In this section we compare their performance in obtaining the disturbing potential *T* at zero altitude from *DT* and *DGD* values given at orbital altitude. We also compare these to the performance of inversion with the 1D-FFT according to equations (4.25), (4.27) and (4.40). The same orbital geometry is assumed; constant altitude H = 400 km; constant LOS orientation, south-north direction, constant intersatellite distance, 230 km; and a regular grid with 0.8 intervals covering 24^o square area. The true values of the quantities involved where obtained from the EGM96 field using spherical harmonic coefficients of degree and order in the range 20-180.

In order to compare and analyze the performances with different geographical locations and different signal content, we chose three test areas with the same configuration described above, but different geographical location. Test area #1 is centered at $\phi_m = 50^o$, $\lambda_m = 0^o$. Test area #2 is centered at $\phi_m = 0^o$, $\lambda_m = 0^o$ and test area #3 is centered at the Himalaya at $\phi_m = 27^o$, $\lambda_m = 87^o$. We applied the regularization methods with both *DT* and *DGD* as measurements for each test area. Errors in the solution with TSVD were found to be considerably larger (about three times larger) than in the solutions with other methods for all test areas. Therefore, we do not consider this method further.

5.4.1 Considering only Measurement Errors

First, we compared the performances considering only random errors (no model errors). The comparison was done for test area #1. Tables 5.5 and 5.6 show the errors statistics

for the case of using *DT* and *DGD*, respectively. Tikhonov method produced the smallest errors for the central area namely, 2.1 and 2.4 m^2/s^2 for *DT* and *DGD*, respectively, with corresponding relative errors of 18% and 21%. We could say that, in general, all methods yielded the same level of errors, considering both tests. The largest error (s.d.) was 3.0 m^2/s^2 obtained with DSVD when using *DGD* data.

Method	Total area m^2/s^2		Central area m^2/s^2		Rel error	Reg param
	Mean	Stdev	Mean	stdev		
Tikhonov	0.00	3	0.1	2.1	0.18	$1\cdot10^{-25}$
DSVD	0.00	7.4	0.4	2.5	0.22	$3\cdot10^{-21}$
CG	0.4	10	0.5	2.6	0.23	13 iter
1D FFT with Tikhonov	0.03	6.0	0.1	2.5	0.22	$6\cdot10^{-21}$

Table 5.5: Errors in *T* from *DT* using different regularization methods considering only random errors, H=400 km, sampling interval of $0^o.8$ and for 24^o square area, area test #1, using EGM96 field (20-180).

Method	Total area m^2/s^2		Central area m^2/s^2		Rel error	Reg param
	Mean	Stdev	Mean	stdev		
Tikhonov	0.01	4.9	0.1	2.4	0.21	$4\cdot10^{-26}$
DSVD	0.60	10	0.5	3.0	0.27	$8\cdot10^{-27}$
CG	0.07	6.7	0.12	2.5	0.22	31 iter
1D FFT with Tikhonov	0.01	7.38	0.9	2.7	0.24	$2\cdot10^{-31}$

Table 5.6: Errors in *T* from *DGD* using different regularization methods considering only random errors, H=400 km, sampling interval of $0^o.8$ and for 24^o square area, area test #1, using EGM96 field (20-180).

5.4.2 Considering Measurement and Model Errors

Next, we repeated both tests but this time also considering model errors. Results are tabulated in Tables 5.7 and 5.8. As in previous tests with model errors, a large mean error is observed with all the methods. With respect to the standard deviation in the central area, the best result was produced by the DSVD method with *DT* data, namely 2.3 m^2/s^2

with 21% relative error. The worst result, for both data types, was obtained with the CG method, yielding standard deviation in the central area of 3.3 and 4.5 m^2/s^2 with *DT* and *DGD*, respectively.

Method	Total area m^2/s^2		Central area m^2/s^2		Rel error	Reg param
	Mean	Stdev	Mean	stdev		
Tikhonov	0.4	49	7.7	2.7	0.26	$5\cdot10^{-25}$
DSVD	4.7	26	10	2.3	0.21	$3\cdot10^{-21}$
CG	0.5	80	5.8	3.3	0.30	47 iter
1D FFT with Tikhonov	3.6	19	10	3.0	0.28	$4\cdot10^{-29}$

Table 5.7: Errors in *T* from *DT* using different regularization methods considering random and model errors, H=400 km, sampling interval of $0^o.8$ and for 24^o square area, area test #1, using EGM96 field (20-180).

Method	Total area m^2/s^2		Central area m^2/s^2		Rel error	Reg param
	Mean	Stdev	Mean	stdev		
Tikhonov	7	23	9	2.9	0.26	$9\cdot10^{-26}$
DSVD	4	15	6.5	2.8	0.25	$1\cdot10^{-26}$
CG	4	15.2	0.1	4.5	0.4	11 iter
1D FFT with Tikhonov	5	18	5	3.5	0.32	$3\cdot10^{-31}$

Table 5.8: Errors in *T* from *DGD* using different regularization methods considering random and model errors, H=400 km, sampling interval of $0^o.8$ and for 24^o square area, area test #1, using EGM96 field (20-180).

Method	Total area m^2/s^2		Central area m^2/s^2		Rel error	Reg param
	Mean	Stdev	Mean	stdev		
Tikhonov	07.6	37	6.5	1.7	0.09	$4\cdot10^{-25}$
DSVD	6	19	6.4	2.6	0.14	$4\cdot10^{-21}$
CG	7	28	7.4	2.9	0.16	27
1D FFT with Tikhonov	5	33	6	3.0	0.16	$3\cdot10^{-30}$

Table 5.9: Errors in *T* from *DT* using different regularization methods considering random and model errors, H=400 km, sampling interval of $0^o.8$ and for 24^o square area, area test #1, using EGM96 field (20-180).

In test area #2, the Tikhonov method gave the best results with the *DT* data, where the error (s.d) is 1.7 m^2/s^2 with a relative error of 0.9%; and, the CG method was best with *DGD* data, yielding an error (s.d.) of 2.3 m^2/s^2. On the other hand, the 1D-FFT method yielded larger errors using *DT* data. The error (s.d.) was 3.0 m^2/s^2, and the DSVD method with *DGD* data yielded 4.1 m^2/s^2, see Tables 5.9 and 5.10.

Finally, the comparison for test area #3 is represented in Tables 5.11 and 5.12. The Tikhonov method produced the smallest error for *DT*, 10.2, while the 1D-FFT method yielded the smallest error for *DGD*, 13.0 m^2/s^2. The 1D-FFT method produced the largest errors with *DT* data producing a 19.2 m^2/s^2 error (s.d.) and, the DSVD method yielded the worst result with *DGD* data, having an error (s.d.) of 17.5 m^2/s^2.

Method	Total area m^2/s^2		Central area m^2/s^2		Rel error	Reg param
	Mean	Stdev	Mean	stdev		
Tikhonov	7.1	24	8.6	3.3	0.19	$3\cdot10^{-26}$
DSVD	4.5	13.4	7.3	4.1	0.21	$6\cdot10^{-27}$
CG	7	24	7.4	2.3	0.12	41
1D FFT with Tikhonov	5	34	8.3	3.4	0.18	$2\cdot10^{-32}$

Table 5.10: Errors in *T* from *DGD* using different regularization methods considering random and model errors, H=400 km, sampling interval of $0^o.8$ and for 24^o square area, area test #1, using EGM96 field (20-180).

Method	Total area m^2/s^2		Central area m^2/s^2		Rel error	Reg param
	Mean	Stdev	Mean	stdev		
Tikhonov	11	171	18.5	10.2	0.09	$2\cdot10^{-26}$
DSVD	11	96	19	26	0.21	$3\cdot10^{-22}$
CG	19	103	19	15.7	0.13	55
1D FFT with Tikhonov	2.0	92	2.3	19.2	0.22	$6\cdot10^{-22}$

Table 5.11: Errors in *T* from *DT* using different regularization methods considering random and model errors, H=400 km, sampling interval of $0^o.8$ and for 24^o square area, area test #1, using EGM96 field (20-180).

Method	Total area m^2/s^2		Central area m^2/s^2		Rel error	Reg param
	Mean	Stdev	Mean	stdev		
Tikhonov	8.7	68	13	13.0	0.11	$2\cdot10^{-27}$
DSVD	8.5	55.6	12	17.5	0.15	$9\cdot10^{-28}$
CG	8.7	76	8.7	13.6	0.12	85
1D FFT with Tikhonov	10	102	12	10.8	0.09	$1\cdot10^{-33}$

Table 5.12: Errors in *T* from *DGD* using different regularization methods considering random and errors, H=400 km, sampling interval of $0^o.8$ and for 24^o square area, area test #1, using EGM96 field (20-180).

Overall, the Tikhonov method performed better than the other methods as evaluated by the given tests. This method did not produce the largest error in any of the tests and, on the other hand, produced the smallest error in almost all the tests. The other three methods yielded similar results among them. With this method, also slightly better results were obtained using *DT* rather than *DGD.*

5.5 Finding the Best Regularization Parameter

So far, we have determined the best regularization parameter just by trial for the different regularization methods considered. We have been able to do this since we have access to the true solution. In real life, one only has access to the measurements. Therefore, we

have to define a way to find the optimum α for the Tikhonov, DSVD and 1D-FFT methods and the optimum iteration number for the CG method. Two of the most common methods used for this task are the discrepancy principle method and the L-curve method, see (chapter 4).

The discrepancy method was tried for the Tikhonov and the DSVD methods, but yielded poor results. No convergence could be achieved toward the correct results even when starting with a good approximation of α. Thus, this method is not further discussed. On the other hand the L-curve method which can be applied to the Tikhonov, the DSDV and the 1D-FFT methods produced relatively acceptable results in the tests made.

For the following tests, we define *sol* = *f* and assuming for equation (4.90), $n = 0$ so the solution norm used in the application of the L-curve method is given by $\|sol\| = \|f\|$. The residual norm $\|res\|$ required by this method is defined by equation (4.89). Also here we define the *log* operator to be the natural logarithmic of base *e*.

5.5.1 Considering only Measurement Errors

The L-curve method yielded relatively good results when considering only random errors. The corner of the curve was sharp enough and the corresponding residual's norm $\|res\|$, corresponds on its own to the best α with good accuracy, about 0.5 m^2/s^2 for test area #1 using both *DT* and *DGD*. Figure 5.30a displays the log-log plot, expected to have an L-shape, of the solution norm, $\|sol\|$ (see section 4.3.6.2), obtained using *DT* as measurements, and the residual norm. In the Figure, the corner of the curve corresponds to about –3.387 on the abscissa. This value corresponds in Figure 5.30b to an α of $2.3x10^{-27}$, which is related to 2.7 m^2/s^2 of solution error in Figure 5.31. The difference of this solution error value with respect to the minimum error value is about 0.5 m^2/s^2. The uncertainty of the $\log\|res\|$ value obtained from Figure 5.30 is about 0.001. The associated uncertainty of α is about $0.2x10^{-27}$ which is translated to 0.1 m^2/s^2 of uncertainty in solution errors. Similar results were obtained with data of the other areas and also employing *DGD* values. That is, these tests showed that the optimal α does not correspond exactly to the corner of the curve, but it is reasonably close.

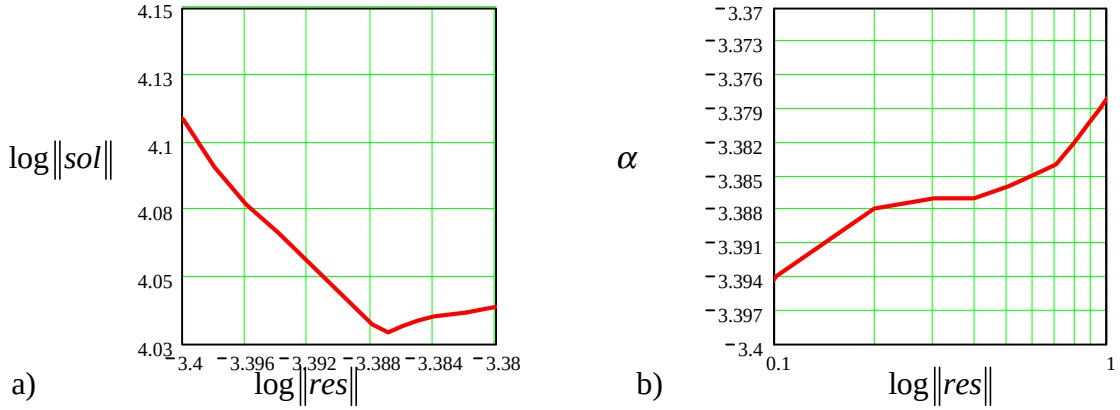

Figure 5.30: a) Plot of the L-curve in the solution of T from DT at H=400 km on 24^o square area with $0^o.8$ sampling interval in Test area #1 considering only measurement errors. Using Tikhonov's method; b) Plot of $\log\|res\|$ in terms of α.

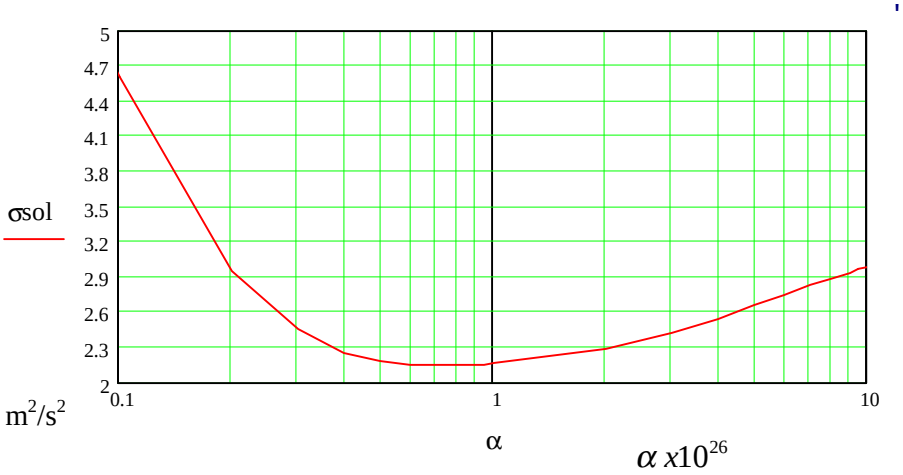

Figure 5.31: Corresponding solution errors for the α values of Figure 5.27b.

5.5.2 Considering Measurement and Model Errors

However, in the presence of model errors, the method did not perform as well. The method presented a couple of problems. One problem is that around the corner region the curve is not sharp enough to determine the right location of the corner. Figure 5.32 displays the L-curve obtained when both random and model errors are included and when considering only the central area (test area #1). The other problem found was that the $\log\|res\|$ of the best α its considerably displaced to the right of the curve's corner.

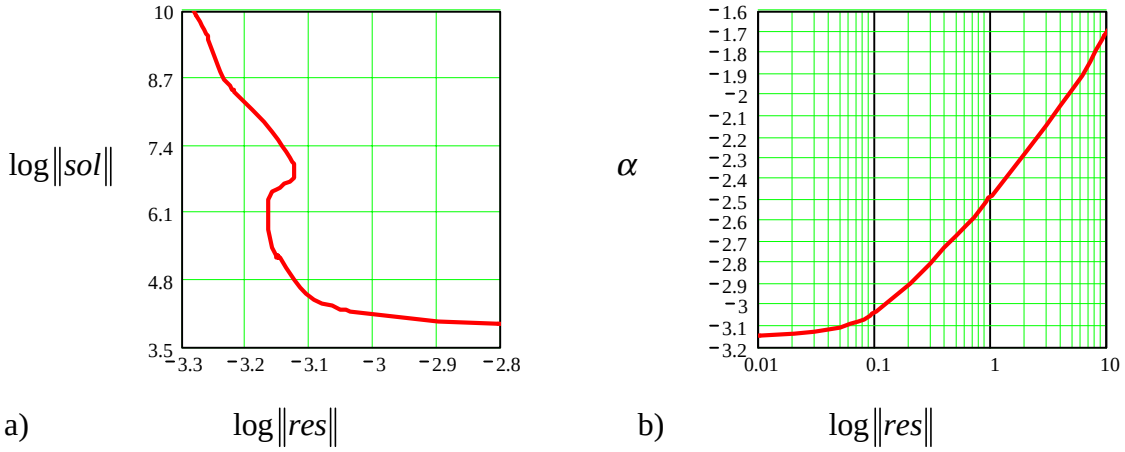

Figure 5.32: a) Plot of the L-curve in the solution of T from DT at H=400 km on 24^o square area with $0^o.8$ sampling interval in Test area #1 considering measurement and model errors. Using Tikhonov's method; b) Plot of $\log\|res\|$ in terms of α.

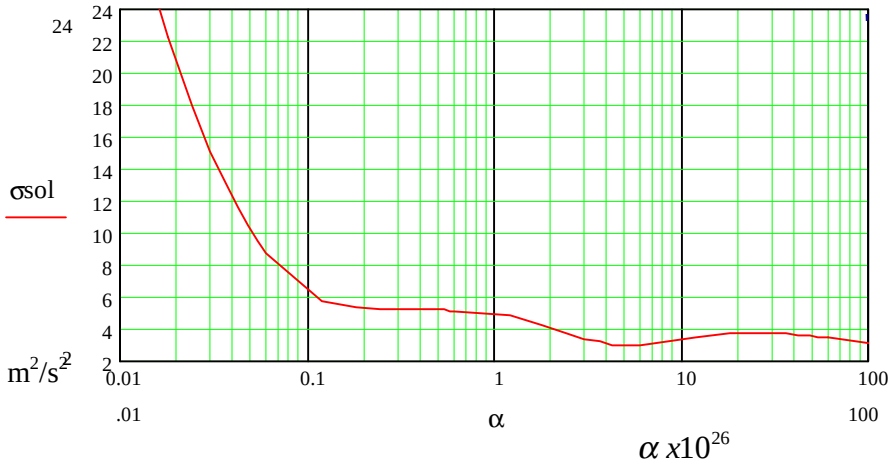

Figure 5.33: Corresponding solution errors for the α values of Figure 5.29b.

With respect to the uncertainty of defining the L-curve's corner, if the uncertainty of the related $\log\|res\|$ value (-3.07) obtained from Figure 5.32 is about 0.05, then the associated uncertainty of α ($0.08x10^{-26}$) is about $0.04x10^{-26}$ which translates to about 5 m^2/s^2 of uncertainty with respect to the related solution error value (7.5 m^2/s^2 in Figure 5.33). From Figure 5.33 we can see that the solution error (7.5 m^2/s^2) related to the L-curve's corner has a difference of 4.6 m^2/s^2 with respect to the minimum error (2.9 m^2/s^2). On the other hand the best α value, or the one that corresponds to this minimum error

value, is about $5x10^{-26}$. The related $\log\|res\|$ values is about –1.96 which is displaced 1.07 units to the right of the curve's corner in Figure 5.32a.

5.5.3 Computation of the k Factor

Now, the problem is to characterize the extra regularization imposed by model errors. Toward this, we express the residuals norm, $\|res\|$, related to the best α in terms of the $\|res\|$ related to the L-curve corner by using a factor *k* as follow

$$\|res\|(\alpha_{best}) = k\left[\|res\|(\alpha_{corner})\right] \tag{5.3}$$

Thus, we end up searching not for the α_{corner} but for the best α or the *k* parameter that relates the norms associated with α_{best} and α_{corner}. In order to find or estimate *k* for a given configuration, different sets of independent data (the same ones used before) that can be processed with the same kernel were used. For every data set a k_i was computed according to equation (5.3), then an average and standard deviation for the set $\{k_i\}$ was found: $\mu_k = 2.3, \sigma_k = 0.9$. Subsequently, for every data set the μ_k was used, instead, to solve for the corresponding $\|res\|(\alpha_{best}(\mu_k))$ from equation (5.3). This will produce variations δf in the solution. This variation and its relative values are defined as

$$\delta f = f^{\varepsilon}_{\alpha(k_i)} - f^{\varepsilon}_{\alpha(\mu)}, \quad rel(\delta f) = \left|\frac{\delta f}{f}\right| \tag{5.4}$$

The computed $\alpha_{best}(\mu_k)$ values were employed to obtain the solution of *T*. Figure 5.34 shows the k_i values and the solution variations δf produced by using $\alpha_{best}(\mu_k)$ instead of $\alpha_{best}(k_i)$. The figure also shows the relative solution variations $rel(\delta f)$. The variations obtained are relatively small. The average values of δf and $rel(\delta f)$ are 1.6 m^2/s^2 and 4.3% respectively. Smaller variations in the solution were obtained when using *DGD* values. The average values obtained were 1.3 m^2/s^2 and 4.0%, for δf and $rel(\delta f)$, respectively (see Figure 5.35). When applying this type of analogies to DSVD method even smaller variations were obtained. The results are displayed in Figure 5.36. The average solution variation is 0.4 m^2/s^2 and the average relative solution variation is 2.6%. The statistics of *k* are $\mu_k = 6.8, \sigma_k = 2.5$.

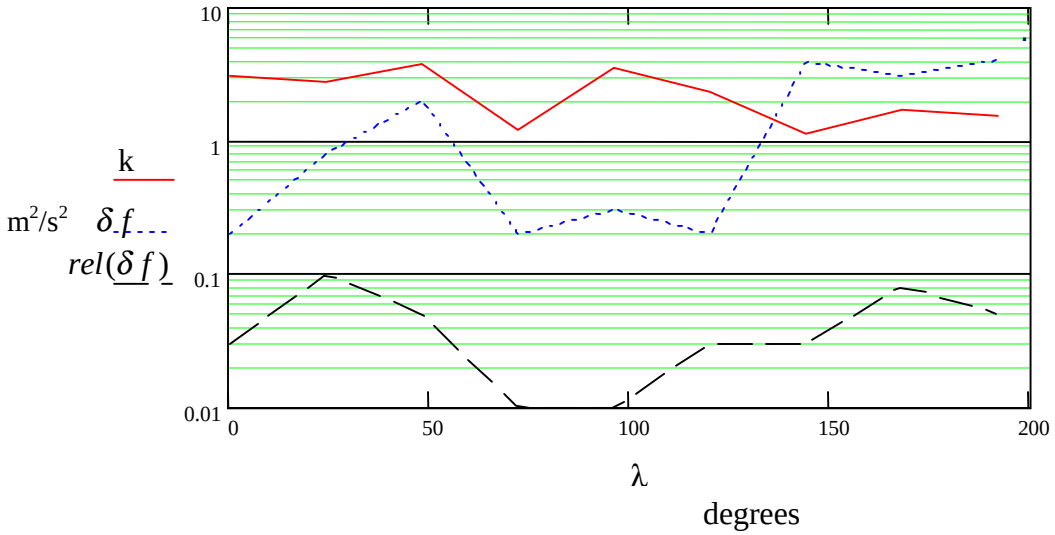

Figure 5.34: Plot of the k coefficient for the residual's norm associated with the best α according to the L-curve, using Tikhonov method and the *DT* kernel for different longitudes; configuration of area test #1

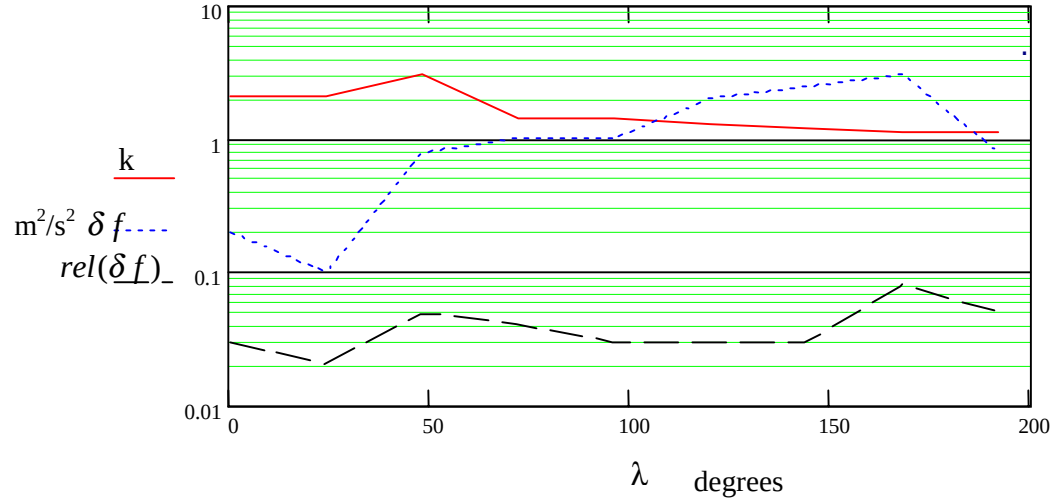

Figure 5.35: Plot of the k coefficient for the residual's norm associated with the best α according to the L-curve, using Tikhonov method and the *DGD* kernel for different longitudes; configuration of area test #1

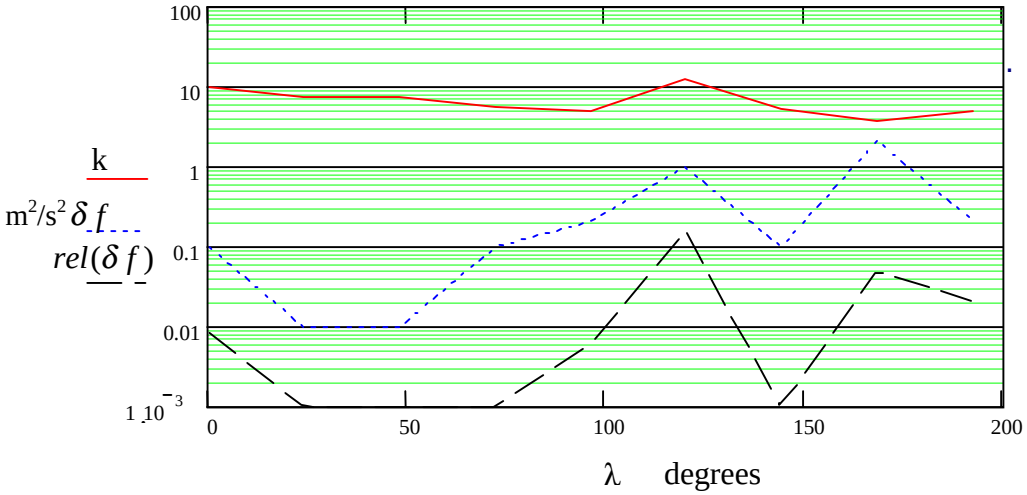

Figure 5.36: Plot of the k coefficient for the residual's norm associated with the best α according to the L-curve, using DSDV method and the *DGD* kernel for different longitudes; configuration of area test #1

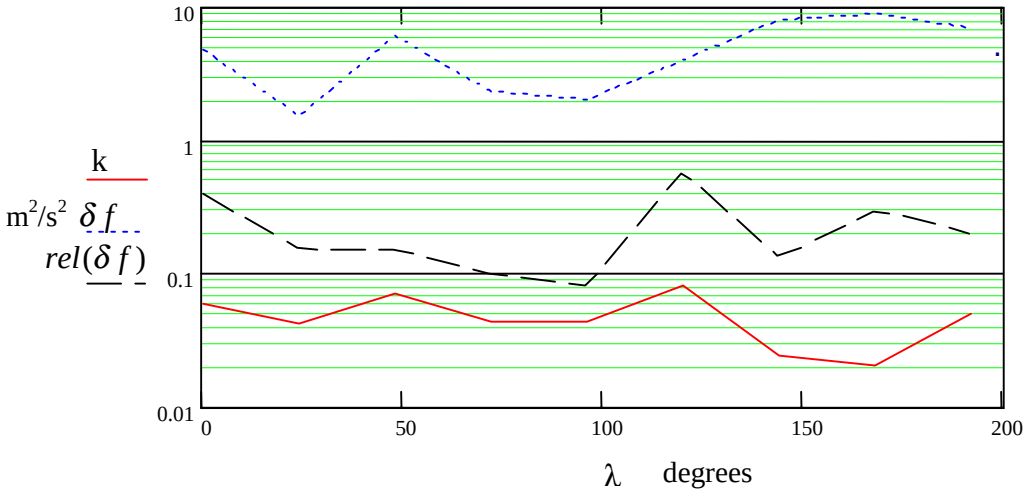

Figure 5.37: Plot of the k coefficient for the residual's norm associated with the best α according to the discrepancy principle, using CG method and the *DGD* kernel for different longitudes; configuration of area test #1

With respect to the CG method, the search of the best iteration number was more difficult to perform. The *k* value to determine here is defined according to equation (4.78). We use the same data sets as for the Tikhonov and DSVD methods. The variation in the solution produced by using the associated μ_k instead of the k_i are relatively large, see Figure 5.37.

The average of the variations in the solution was 4.9 m^2/s^2 and the average of the relative variation was 24%. These values are of the same level of the solution errors themselves. Moreover, even when considering only measurement errors, the variations produced in the solution by using the average k yielded unacceptable results.

5.5.4 Validation of the k Factor

In order to get a better understanding of the solution variations δf, see equation (4.4), associated with the estimated μ_k value of the previous section, we use results of the test in section (5.5.2). Using Figures 5.32 and 5.33 we have already found the values $\log\|res\|_{corner} = -3.07$, $\log\|res\|_{best} = -1.96$. With these values we obtain from Figure 5.38 the corresponding $\|res\|$ values, which are $\|res\|_{corner} = 0.047$, $\|res\|_{best} = 0.14$ Now, using equation (5.3), we obtain $k_i = 3.0$. From figure (5.39) we can see that this $\|res\|_{best}$ value corresponds to $\alpha_{best} = 5x10^{-26}$. Nevertheless, if we instead use $\mu_k = 2.3$ to compute the best residual's norm with equation (5.3) and the value of the above $\|res\|_{corner}$, we obtain the value $\|res\|_{best}(\mu_k) = 0.108$, this corresponds, in Figure 5.39, to an $\alpha_{best}(\mu_k)$ value of $2.5x10^{-26}$. The variation in the solution produced by using $\alpha_{best}(\mu_k)$ rather than α_{best} will be of 0.2 m^2/s^2, see Figure 5.33. Figure 5.40 shows, for the present test, the relationship between k and solution variations produced.

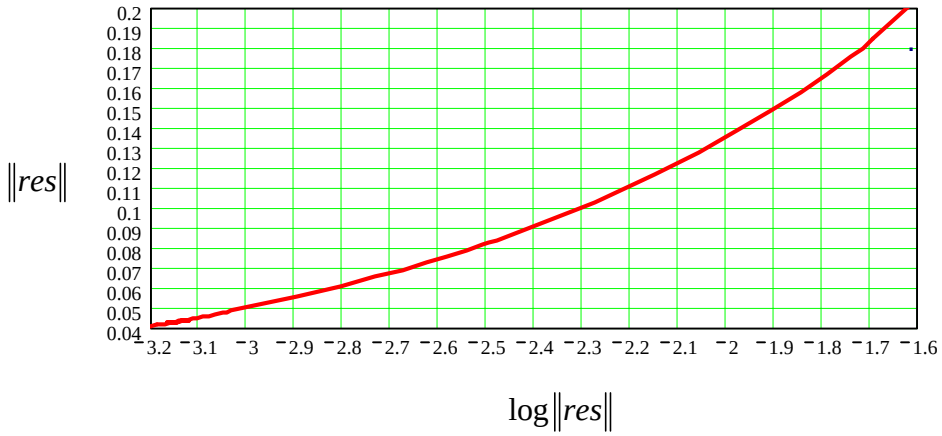

Figure 5.38: Relationship between the residual's norm and its logarithmic value of data in Figure 5.29.

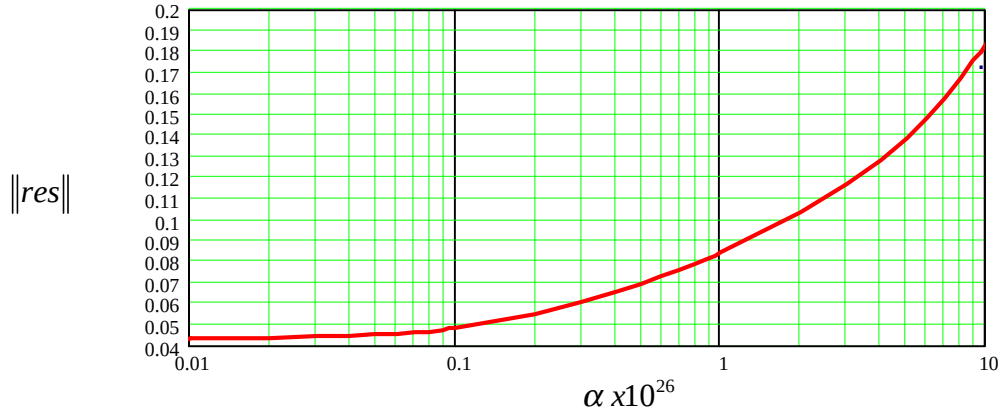

Figure 5.39: Relationship between the residual's norm and the α values of data in Figure 5.29.

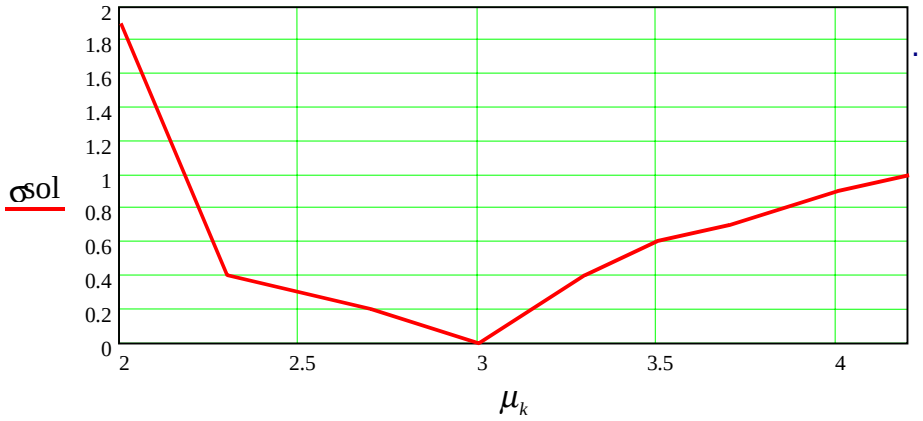

Figure 5.40: Variations produced in terms of *k* in the solution of *T* from *DT* at H=400 km on 24^o square area with $0^o.8$ sampling interval in Test area #1 considering measurement and model errors. Tikhonov's method is used.

5.5.5 The k Factor in terms of Geometrical Configurations

The value of *k* will depend mainly on model errors. We know that model errors tend to increase as the sampling interval gets larger (Figures 5.17 and 5.18), requiring more regularization and causing the *k* value to become larger. On the other hand, model errors will tend to decrease as we increase the area of integration (Figures 5.19 and 5.20). Therefore, the *k* value will tend to 1, as the area gets larger. Figures 5.41 and 5.42 support these facts. Figure 5.41 shows the relationship between *k* and the sampling interval for both data types, *DT* and *DGD*. Values of *k* using *DT* are relatively larger, going from 2.3 at $0^o.2$ grid interval to 3.3 at $1^o.2$ grid interval; whereas, when using *DGD*, they increase from 1.7 to 2.6, respectively. Figure 5.42 shows the *k* dependency on area coverage for

both types of kernels, *DT* and *DGD*. For *DT k* decreases from 3.1 at 12^o square to 1.7 at 48^o square.

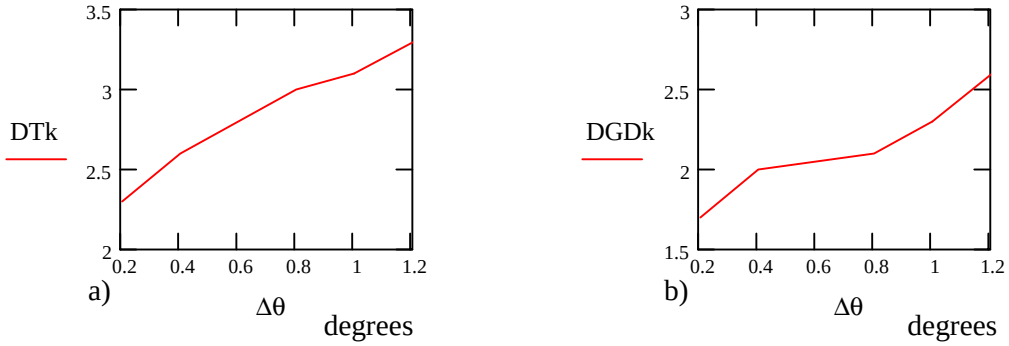

Figure 5.41: Plot of the k coefficient for the residual error in terms of sampling interval to find the best α according to the L-curve with Tikhonov method using the *DT* and *DGD* kernel with configuration of area test #1.

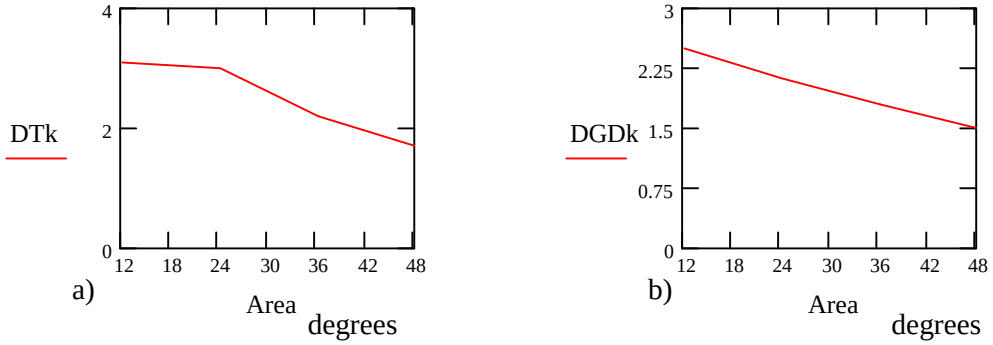

Figure 5.42: Plot of the k coefficient for the residual error in terms of area coverage to find the best α according to the L-curve with Tikhonov method using the *DT* and *DGD* kernel Configuration of area test #1.

The determination of the μ_k factor relating the residual's norm that corresponds to the L-curve corner with the residual's norm than corresponds to α_{best} was done with knowledge of the true solutions that allowed finding α_{best}. Since for actual situations the true solutions are not known, one can only hope that the use of μ_k, obtained from these simulations based on the given geometrical configurations, will produce near optimal solutions. In order to further check the sensitivity of the μ_k factor, set of measurements was simulated with the same geometrical configuration used so far but centered at longitude 230^o, being different from the data sets used to obtain μ_k. The true *k* obtained was 1.22, and the additional error produced in the solution by using the previously

computed $\mu_k = 2.3$ instead of the true k was 0.3 m^2/s^2, which is about 0.02% of the solution signal.

5.6 Regularization combined with B-Spline Smoothing

Now, we stabilize the inversion process by combining Tikhonov type regularization with 2-D B-spline smoothing. The justification of this method is the following. In principle, applying an appropriate smoother to the data or solution in order to remove of the high frequencies, which are contaminated by random errors, can do the job of regularization. If this is the case, we just apply the same smoother to the true solution and compare. However, there is a drawback for smoothers like B-spline, cubic splines and frequency domain smoothers. They tend to perform better with greater amount of data and higher data density. In many situations the available density and amount of data is not enough to achieve the desired accuracy with a certain amount of smoothing.

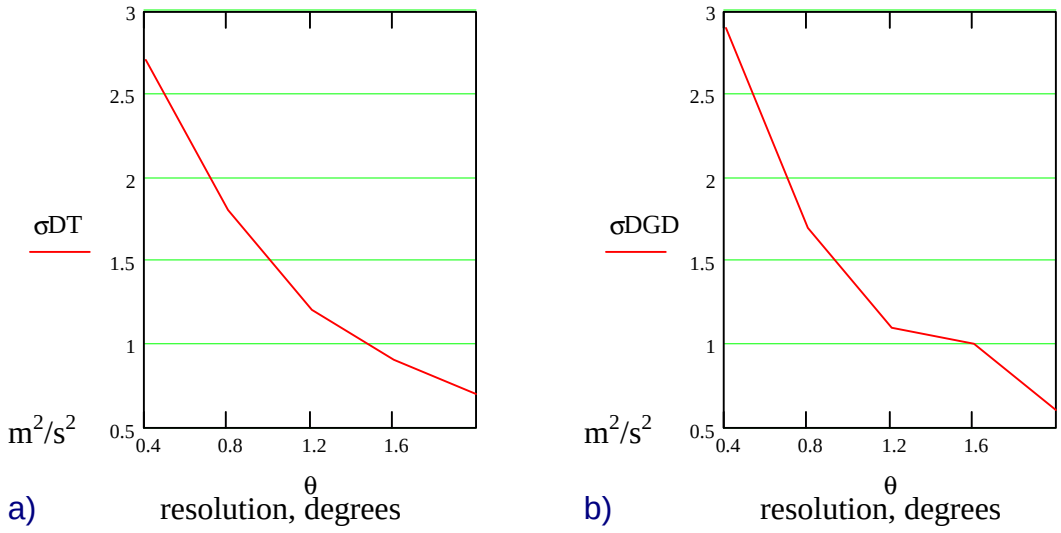

Figure 5.43: Errors from applying Tikhonov regularization with B-spline smoothing. For area test #1 grid of 24^o square, $0^o.4$ sampling interval with *DT* and *DGD*. H=400km EGM96 (20-180) central 4^o square.

For our situation we wanted to use a smoother that can also be applied to the true values. Using B-splines the data is smoothed in a least squares sense. However, when applied to our systems, it was not enough to overcome the ill-posedness of the problem. Therefore, we have to combine it with some regularization to improve the performance. For the tests, this time, we used $0^o.4$ sampling interval since smoothing methods tend to perform poorly with less data density. In order to keep the same area as with previous tests we used a 60x60 grid producing a system with computational requirements near the limits of the capabilities of a PC with respect to memory and speed. The system to solve involves the solution of 3600 unknowns. The method was applied to test area #1 and for both data type, *DT* and *DGD*. The solution errors obtained for $1^o.2$-$1^o.6$ resolutions were about 1

m^2/s^2, which would corresponds to a 10 cm geoid with 150 km resolution. These results were obtained with both kernels, *DT* and *DGD*, see Figure 5.43.

CHAPTER 6

DISCUSSION AND CONCLUSIONS

In this study we have analyzed the feasibility of using in-situ GRACE measurements for local gravity field determination as an alternative to global solution methods, which yield solutions in terms of spherical harmonic coefficients. The method analyzed is based on integral inversion aided with regularization techniques. The observables considered are potential differences *DT* and the LOS component of the gravity disturbance differences *DGD* as they are given by equations (1.20) and (1.12) respectively.

Both observables are affected by position, velocity and acceleration errors. With respect to position errors, the higher precision requirement is on relative position for *DT*. About 1 cm of relative positional accuracy will yield *DT* with 0.01 m^2/s^2 of precision. For velocities, the higher precision requirement is for relative velocity for both *DT* and *DGD.*

Using *DT* and *DGD* according to equations (3.8) and (3.21), respectively, the solution of the disturbing potential *T* at the Earth's surface in spherical approximation can be obtained by integral inversion through appropriate discretization. For the operational altitude of the GRACE mission, which is projected to be 300-500 km, the process turns out to be very ill-conditioned mainly due to gravity field attenuation with altitude. For instance, the discretization of the associated kernels, for a $0^o.4$ interval regular grid over a 12^o square area, will produce systems with condition numbers of about $1x10^{19} - 1x10^{21}$ for the GRACE operative altitudes.

To some extend, the ill-condition of our systems is also affected by sampling interval and area coverage of the measurements. For the sampling interval of the tests made, the condition number increases as the sampling interval becomes smaller, ranging from $8x10^{20}$ and $9x10^{21}$ at 0.2^o sampling interval, respectively, for the *DT* and *DGD* kernels to about $8x10^{18}$ at $1^o.2$ sampling interval for both kernels (see Figure 5.2a). However, for the range of sampling intervals considered in the Figure the instability of the systems was relatively the same.

In the case of size of integration area, the ill-condition increases with the area since, for a given sampling interval, more area means more points involved producing larger condition number. This fact is supported by Figure 5.2b. Using $0^o.4$ constant interval, the condition number varied from $1x10^{18}$ to $3x10^{22}$, respectively, for 4^o and 24^o square area for the *DT* kernel. On the other hand, the *DGD* kernel showed larger values, going from $1x10^{19}$ to $4x10^{22}$ respectively for the same grids.

For a given grid of points being regular with respect to latitude and longitude, the ill-condition tends to increase toward the polar regions due to the meridian convergence, which brings the points closer along parallels. Using the same configuration as for Figure 5.1, the change of the condition number is relatively small in going from the equator to 80^o latitude for both kernels as seen in Figure 5.3.

Data error requirements seem to be very demanding for downward continuation of both *DT* and *DGD*. The Tikhonov regularization method was applied for the following configuration a grid with $0^o.8$ sampling interval over a 24^o square area at 400 km altitude. Measurement errors smaller than $1x10^{-5}$ m^2/s^2 are required to obtain errors of the level of 1 m^2/s^2 with a relative error of about 10 %. Nevertheless, when using 0.01 m^2/s^2 measurement errors the solution errors obtained were about 3 m^2/s^2 with a relative error of 20 %, which indicates that the system is not too sensitive to measurement errors. These results can be appreciated in Figures 5.4 and 5.6.

When considering model errors, large mean values of the solution errors were observed. For all the tests considered in Figure 5.14, the average of the solution errors mean values is 6 m^2/s^2. The average of the standard deviation and relative error are 5.9 m^2/s^2 and 23%, respectively. Thus, in the average the standard deviation was twice larger than in the case of only random noise. Similar results were obtained for the *DGD* kernel, for which the averages of the standard deviation and mean are 5.3 and 8.7 m^2/s^2, respectively. The mean value of the relative error was 24% (see Figure (5.15)).

In the case of the edge effect, solution errors greater than 100 m^2/s^2 on the southern limits of the area with a total standard deviation of 48 m^2/s^2 were observed for the given configuration. This is also corroborated by Table 5.1 where some of the standard deviations corresponding to the total area are even larger than 48 m^2/s^2.

Solution errors tend to decrease with lower data altitude. This can be appreciated on Figure 5.16, which displays the best solution of *T* obtained at different altitudes in the 300-500 km range using *DT* and *DGD* measurements. In both cases, the errors varies from about 1 m^2/s^2 at 300 km to 3.5 m^2/s^2 at 500 km. The Figure also plots the errors for the total area which area considerably large, from about 40 m^2/s^2 at 300 km to 58 m^2/s^2 at 500 km, mainly due to the edge effect.

With respect to sampling interval the solution errors increase with the size of data interval. Disturbing potential values were estimated from *DT* values at 400 km altitude

with data over a 24^o square area with different sampling intervals. Table 5.1 displays errors statistics. The standard deviation of the central area increases systematically from 2.2 m^2/s^2 at $0^o.2$ interval to 3.5 m^2/s^2 at $1^o.2$ interval. As expected, more regularization is required with the interval reduction. The α value also varies from $3x10^{-42}$ to $1x10^{-43}$ at $0^o.2$ and $1^o.2$ respectively. Similar results were obtained for the *DGD* kernel.

The third factor affecting the ill-condition analyzed before is the area coverage. For this factor, we considered three different area size; 12^o, 24^o and 36^o square for $0^o.8$ interval. The ill-condition tends to increase with the area. Plots in figures 5.19 and 5.20 support this fact. In the first figure, we have the solution of T obtained from *DT* for 12^o, 24^o and 36^o square areas. The corresponding estimated errors were 3.6, 2.7 and 2.1 m^2/s^2. In the last figure we have the solution of *T* obtained from *DGD*. The corresponding error values were 4.7, 2.8 and 2.6 m^2/s^2.

There are three types of interpolation involved in the geometric configurations employed in this study. They are interpolation to a regular grid in latitude and longitude, same altitude, and to the same intersatellite distance. Each interpolation will have an error associated.

For interpolation to a regular grid in latitude and longitude, the errors associated were relatively small. Figures 5.25 and 5.26 show the errors in interpolating values of *DT* and *DGD*, respectively, to a grid of $0^o.4$ intervals using data from 30, 40 and 50-day Keplerian orbits. The interpolation was made with cubic spline approximation using Delaunay triangulation method. The errors obtained seem to decrease almost systematically toward the pole. However they stay within the same order of magnitude from the equator to latitude 80^o. For example, with a 40-day orbit they range from 0.002 m^2/s^2 at the equator to 0.001 m^2/s^2 at latitude 80^o. The improvement with latitude is expected since more data is generated in the polar region due to the meridian convergence, this is supported by Table 5.2. The improvement of interpolation with a 50-day orbit with respect to a 30-day orbit is significant. For instance, at mid-latitude a 30-day orbit will produce interpolation error of about 0.005 m^2/s^2, half of the measurement error adopted in this study, whereas a 50-day orbit yielded about 0.001 m^2/s^2 interpolation error, which is 5 times smaller.

For the other 2 types of interpolation made, LSC was used to interpolate the data to the desired regular configuration. Both types of observables, *DT* and *DGD* produced similar results. When considering data over a 12^o orbital arc, interpolation errors to same altitude and distance were relatively small. The errors in interpolating to the same H are of the order of $1x10^{-4}$ m^2/s^2 for all latitudes considered on Table 5.3, whereas the error of interpolation to the same intersatellite distance was $2x10^{-4}$ m^2/s^2 at the equator and $5x10^{-3}$ m^2/s^2 at 75^o latitude. However, when considering data for a 10-day orbit the altitude of different orbital arc varied about 12 km requiring extrapolation of data. The extrapolation errors obtained, when extrapolating data of a 12^o orbital arc to a different altitude, were up to 0.008 m^2/s^2 for 6 km extrapolation distance.

The inversion methods treated in chapter 4 were tested and their performance compared by employing three test areas with the same configuration described above, but different geographical location. The regularization methods were applied with both, *DT* and *DGD* for every test area. The methods that performed better were: The Tikhonov methods, the damped singular value decomposition methods (DSVD), the conjugate gradient method (CG) and the 1-D FFT with Tikhonov methods.

We could say that these 4 methods yielded the same level of errors when considering only random errors for test area #1, see Tables 5.5 and 5.6. The errors were about 2.5 m^2/s^2 in *T* with 0.8 resolution with relative error of 23%. Next, the methods were applied for the 3 test areas considering model errors. From the results, which are displayed in Tables 5.7-5.12 we could conclude the following. Overall, Tikhonov method performed better than the other 3 methods for the given tests. This method did not produced the largest error in any of the tests and, on the other hand, produced the smallest error in almost all the tests. The other three methods could be considered to yield similar results among them. The projected Landweber iteration method applied to 1-D FFT did not offer any improvement in the solution. Convergence was never achieved for the tests considered.

One important aspect for the regularization methods is to find the best regularization parameter. Two popular methods considered here are the discrepancy principle and the L-curve method. The discrepancy method was tried for the Tikhonov, DSVD and 1-D FFT combined with Tikhonov regularization methods and gave poor results. No convergence could be achieved toward the optimal regularization even when starting with a good approximation of α. The L-curve method, which can be applied to Tikhonov, DSVD and the 1D-FFT with Tikhonov method, yielded good results when considering only random errors. The corner of the curve was sharp enough and the residual's norm corresponding the best α was relatively near the L-curve corner. The additional error on *T* produced by using the α_{corner} instead of the α_{best} was about 0.2 m^2/s^2 for test area #1 using both *DT* and *DGD*. Figure 5.27a displays the L-curve plot obtained when considering only random errors, using *DT* as measurements. However, when considering model errors, the method did not perform as good. The additional error on *T* produced by using the α_{corner} instead of the α_{best} was about 5 m^2/s^2. This may be due to the severe presence of model errors, specifically the edge effect. A couple of problems were found when searching for the best α with the L-curve in the presence of model errors. One problem was that around the corner region the curve is not smooth enough to determine the right position of the corner. Figure (5.29) display the L-curve obtained when contemplating random and model errors and considering only the central area. The other problem found was that the best α does not correspond to the norm value related to the corner of the curve. It is displaced to the right of the corner. This is most likely due to the extra regularization required by the model errors.

A geometry adaptive method was employed to find the best α. The method consists of determining a *k* parameter that relates the residual norm corresponding to the corner of the L-curve with the residual for to the best α, according to equation (5.3).

The additional errors in the solution produced by the uncertainty of the estimated of *k* were relatively small. The statistics for *k* are; $\mu_k = 2.3, \sigma_k = 0.9$. The average of the variations in the solution and the relative variation are 1.6 m^2/s^2 and 4.3% respectively. Slightly better results were obtained when using *DGD* values. The average of the variations in the solution and the relative variation are 1.3 m^2/s^2 and 4.0% respectively.
When applying the method to DSVD method even smaller errors were obtained. The results are displayed in Figure 5.33. The mean variation on the solution is 0.4 m^2/s^2 and the mean relative solution variation is 2.6%. The *k* statistics were $\mu = 6.8, \sigma = 2.5$.

Apparently, the value of *k* depends mainly on model errors. We know that model errors increase as the sampling interval gets larger. This will also require more regularization to reduce the effect of the measurement error in the solution making the *k* value larger. On the other hand, model errors will be reduced as we increase the area coverage. Therefore, the *k* value will tend to one, as the area gets larger, see Figures 5.38 and 3.39.

For the CG method, the role of regularization parameter is played by the iteration number so, the task here is to find the optimum number of iterations. This number was more difficult to find. The *k* value to determine here is defined according to equation (4.78). The same data sets as for the Tikhonov and DSVD methods were used. The additional errors in the solution produced by the uncertainty of the estimated of *k* were relatively large. The average variation in the solution was 4.9 m^2/s^2 and the average relative variation was 24%. These values are of the same level of solution errors themselves. Moreover, even when considering only measurement errors, the uncertainty of *k* yielded unacceptable results.

Finally, we applied Tikhonov regularization combined with B-spline smoothing. The method yielded smaller errors using the above configuration but with 0.4^o sampling interval. An error of 1.2 and 1.1 m^2/s^2 from *DT* and *DGD*, respectively, for 1.2^o length resolution. The corresponding relative error was about 10%, see Figure 5.40. This could potentially produce about 10 cm geoid for about 150 km resolution.

Some recommendations for future studies are: To further analyze the performance other methods to find the best α as well as the best number of iterations for the CG method. The empirical L-curve method proposed here was found to produce up to 10% additional error in the solution. Further research should concentrate on refining the empirical relationship, like using the solution norm and the residual norm in a combined way rather than only the residual norm.

Another possible line of investigation could be to apply, either to the measurements or to the solution, other smoothing method like low-pass filters, Gaussian kernel etc, in order to reduce effect of measurement errors on the solution.

Effects of model errors have been found to be of concern. One way to reduce them is to employ data over larger area, which implies to use more data producing larger inverting matrices. The use of the 1-D FFT inversion, which allows the use of more data than conventional regularization methods, can also be further investigated.

REFERENCES

Arabelos, D., Tscherning, C. C. (1990), Simulation of regional gravity field recovery from satellite gravity gradiometer data using collocation and FFT, *Bul. Geod.*, 64, pp. 363-382.

Bertero, M., Boccacci, P. (1998), Introduction to inverse problems in imaging, Institute of Physics Publishing Bristol and Philadelphia, London.

Bjerhammar, A. (1968), On Gravity. Royal Institute of Technology, Geodesy Division, Stockholm.

Blaha, T., Hirsch, M., Keller, W., Scheinert, M. (1996), Application of a spherical FFT approach in airborne gravimetry, *Journal of Geodesy*, 70, pp. 663-672.

Bock, Y. (1983), Estimating crustal deformation from a combination of baseline measurements and geophysical models, *Bull. Geod.*, 57, pp 294-311.

Brigham, E., O. (1988), The Fast Fourier Transform and its Applications. Prentice-Hall, Inc Englewood Cliffs, N.J.

Bouman, J. (1998), Quality of regularization methods, DEOS Report no 98.2, Delft University Press.

Colombo, O. L. (1981), Global Geopotential Modeling from Satellite-to-Satellite Tracking, Dep. of Geod. Sci., Rep. 317, Ohio State Univ., Columbus.

Colombo, O, L. (1984), The Global Mapping of Gravity with two Satellites, Netherlands geodetic Commission.

Douglas, B. C., Goad, C. C., Morrison, F. F. (1980), Determination of the Geopotential from Satellite-to-Satellite Tracking Data, *Journal of Geo. Res*. Vol. 85, No. B10 pp. 5471-5480.

Fischell, R. E., Pisacane, V. L. (1978), A Drag Free Lo-Lo Satellite System for Improved Gravity Field Measurements, Applications of Geodesy to Geodynamics, Dep. of Geod. Sci. Rep. 280, p. 213, Ohio State Univ., Columbus.

Forsberg, R., Sideris, M. G. (1993), Geoid computations by the multi-band spherical FFT approach, *Manus. Geod.*, 18, pp. 82-90.

Gaposchkin, E. M. (1998), SST Geopotential Determination Using Inverse Methods. AGU Spring Meeting, May, 1998 Boston, MA.

Haagmans, R., Min, E., Gelderen, M. v. (1993), Fast evaluation of convolution integrals on the sphere using 1-D FFT, and a comparison with existing methods for Stokes' integral, *Manus. Geod.*, 18, pp. 227-241

Hajela, D. P. (1974), Director Recovery of mean gravity anomalies from satellite to satellite tracking, Dep. of Geod. Sci., Rep. 218, Ohio State Univ., Columbus.

Hajela, D. P. (1977), Recovery of 5 Deg. mean gravity anomalies in local areas from ATS-6/GEOS-3 satellite to satellite range-rate observations, Dep. of Geod. Sci., Rep. 259, Ohio State Univ., Columbus.

Hajela, D. P. (1978), Improved procedures for the recovery of 5 Deg. mean gravity anomalies from ATS-6/GEOS-3 satellite to satellite range-rate observations using least squares collocation, Dep. of Geod. Sci., Rep. 276, Ohio State Univ., Columbus.

Hajela, D. P. (1979), Tests for the Recovery of 5 deg. Mean Gravity Anomalies in Local Areas From ATS 6/Geos 3 Satellite to Satellite Range-Rates Observations. *Journal of Geo. Res.*, Vol. 84 No. B12, p 6884.

Hajela, D. P. (1981), A simulation study to test the prediction of 1°X1° mean gravity anomalies using least squares collocation from GRAVSAT mission, Dep. of Geod. Sci., Rep. 316, Ohio State Univ., Columbus.

Hanke, M. (1995), Conjugate gradient type methods for ill-posed problems, Longman Scientific and Technical. USA.

Hansen, C., O'Leary, D. (1993), the use of the L-curve in the regularization of discrete ill-posed problems. *SIAM J. Sci. Comput.*, 14(6), pp. 1487-1503.

Hansen, C., O'Leary, D. P. (1997), Regularization Algorithms Based on Total Least Squares, Resent advances in total least squares techniques and errors-in-variables modeling, SIAM, Philadelphia; pp. 127-137.

Heiskanen, W., A., Moritz, H. (1967), Physical Geodesy, W. H. Freeman and Company, San Francisco.

Hofmann, B. (1986), Regularization for applied inverse and ill-posed problems, Teubner-Tebner, Leipzig.

Hotine, M. (1968), Mathematical geodesy, Dept. of Commerce, Environmental Science Services Administration, Washington, U.S.

Ilk, k. H. (1984), On the analysis of satellite to satellite tracking data, International Symposium on Space Techniques for Geodynamics.

Ilk, k. H. (1985), On the regional mapping of gravitation with two satellites. Proc. 1. Hotine Marussi Symp. On math, geodesy, pp. 807-833, politechnic di Milano.

Ilk, k. H. (1987), Regional Gravity Field Mapping: gravity gradiometry versus satellite-to-satellite tracking techniques. Proceedings of the IAG Symposia, pp. 284-295, International Association of Geodesy, Paris.

Ilk, k. H. (1993), regularization for high resolution gravity field recovery by future satellite techniques, Inverse Problems: Principles and applications in geophysics, technology, and medicine, Proceedings of the International Conference held in Potsdam, Mathematical Research volume 74, Akademie Verlag.

Ilk, k. H., Kusche, (2000), A Contribution to Data Combination in Ill-posed Downward Continuation Problems, Institute of Theoretical Geodesy, University of Bonn, Germany.

Jansson, P. A. (1998), Deconvolution of images and spectra, Academic Press, San Diego.

Jekeli, C., Rapp, R. H. (1980), Accuracy of the determination of mean anomalies and mean geoid undulations from a satellite gravity field mapping mission, Dep. of Geod. Sci. Rep. 307, Ohio State Univ., Columbus.

Jekeli, C. (1981), Modifying Stokes' function to reduce the error of geoid undulation computations, *Journal of Geo. Res*., Vol. 86, No. B8, pp. 6985-6990.

Jekeli, C. (1998a), On the determination of the local gravity field from satellite-to-satellite tracking, Report for Mission Analysis and Science Requirement Support for Gravity Recovery and Climate Experiment (GRACE), University of Texas, Austin.

Jekeli, C. (1998b), An Analysis of Geopotential Difference Determination from Satellite-to-Satellite Tracking, The 2nd joint meeting of the International Gravity Commission and the International Geoid Commission, 7-12 September, Trieste, Italy.

Jekeli, C. (1999), The determination of gravitational potential differences from satellite-to-satellite tracking, revision summitted to *Celestial Mechanics and Dynamical Astronomy*.

Jekeli, C., Garcia, R. (2000), Local Geoid Determination with In Situ Geopotential Data Obtained from Satellite-to-satellite Tracking, Gravity from Dedicated Satellite Experiments Gravity, Geoid, Geodynamics 2000 Symposium Banff, Canada.

Kahn, W. D., Klosko, S. M., Wells, W. T. (1982), Mean Gravity Anomalies From a Combination of Apollo/ATS 6 and GEOS 3/ATS 6 SST Tracking Campaigns, *Journal of Geo. Res*., Vol. 87, No. B4, pp. 2904-2918.

Kaula, W. M. (1966) Theory of satellite geodesy; applications of satellites to geodesy, Blaisdell Pub. Co., Waltham, Mass.

Kaula, W. M. (1983), Inference of variations in the gravity field from satellite-to-satellite range-rate, *Journal of Geo. Res*., Vol 88, No B10, pp. 8345-8353

Keating, T., Taylor, P., Kahn, W., Lerch, F. (1986), Geopotential Research Mission Science, Engineering, and Program Summary, NASA Technical Memorandum 86240.

Kim, J. (2000), A Low-Low Satellite-to-Satellite Tracking Mission, Doctoral dissertation, The University of Texas at Austin.

Klees, R., Boumsn, J., Koop, R., Visser, P. (2000), From Eotvos to mGal, Technical Report on Regularization and downward continuation, study team 1-Workpackage 2, SID/DEOS.

Lagendijk, R. L., Biemond, J., (1991), Iterative identification and restoration of images, Kluwer Academic Publishers, Norwell, Massachusetts USA.

Lemoine, F. G. et al., (1998), The development of the joint NASA GSFC and the National Imagery Mapping Agency (NIMA) geopotential model EGM96. NASA/TP-1998-206861, GSFC, Greenbelt, Mariland.

Mackenzie, R., Moore, P. (1983), A geopotential error analysis for a non-planar satellite to satellite tracking mission, *Journal of Geodesy,* 71, pp. 262-272.

Moritz, H. (1978), Least-Squares Collocation, *Reviews of geophysics and space Physics*, Vol. 16, no 3, p. 421.

Morozov, V., A. (1984), Methods for solving incorrectly posed problems, Springer-Verlag New York.

Pisacane, V. L., Yionoulis, S. M. (1980), Recovery of Gravity variations from Satellite-to-Satellite tracking, The Johns Hopkins University, Applied Physics Laboratory Laurel Maryland.

Reigber, C. (1988), Lecture Notes on Gravity Field Recovery from Satellite Tracking Data, International Summer School of Theoretical Geodesy, Assisi Italy.

Rummel, R. (1975), Downward continuation of gravity information from satellite to satellite tracking or satellite gradiometry in local areas, Dep. of Geod. Sci., Rep. 221, Ohio State Univ., Columbus.

Rummel R., Hajela D. D., Rapp R. H. (1976), Recovery of mean gravity anomalies from satellite-to-to satellite range-rate date using least-squares collocation, Dep. of Geod. Sci., Rep. 248, Ohio State Univ., Columbus.

Rummel, R. (1979), Determination of Short-Wavelength components of the gravity field from satellite -to-satellite tracking or satellite gradiometry - an attempt to an identification of problem areas. *Manus. Geod.,* Vol. 4, pp. 107-148.

Rummel, R. (1980), Geoid heights, Geoid height differences, and mean gravity anomalies from “low-low” satellite-to-satellite tracking - an error analysis. Rep. 306, Dep. of Geod. Sci. Ohio State Univ. Columbus.

Rummel, R. (1980), Error analysis of “low-low” satellite-to-satellite tracking, 4th International Symposium “Geodesy and Physics of the earth”.

Schuh, W. D. (1996), Sunkel, H., Hausleitner, W., Hock, E., Refinement of iterative procedures for reduction of spaceborne gravimetry data, ESA-CIGAR, Workpackage 4, Final Report.

Schwarz, K. P. (1979), Geodetic Improperly Posed Problems and Their Regularization, *Bolletino di Geodesia e Scienze Affini*, vol., 38, no. 3, pp. 389-416.

Schwarz, K. P., Gerstl, M. (1979), Least Squares Collocation and Regularization, *Bull. Geod.,* 53, pp. 343-361.

Schwarz, K. P., Sideris M. G., Forsberg R. (1990), The use of FFT techniques in physical geodesy, *Geophys, J. Int*., 00, pp. 485-514.

Seeber, G. (1993), Satellite Geodesy, Walter de Gruyter, Berlin.

Sideris, M. G., Li, Y. C. (1993), Gravity field convolutions without windowing and edge effects, *Bull Geod.*, 67, pp. 107-118.

Sideris, M. G., She, B. B. (1995), A new, high-resolution geoid for Canada and part of the U.S. by the 1D-FFT method, *Bull. Geod.*, 69, pp. 92-108.

Sjöberg L. (1979), Integral Formulas for Heterogenous Data in Physical Geodesy, *Bull. Geod*., 53, pp. 297-315.

Sjöberg, L. (1982), On the recovery of geopotential coefficients using satellite-to satellite range-rate data on a sphere, *Bull. Geod.*, 56, pp. 27-39.

Stanton, R. (2000), Science and Mission Requirement Document (revision), Jet Propulsion Laboratory, Center for Space Research, University of Texas.

Strang, v H. G. (1990), Stokes formula using Fast Fourier techniques, *Manus. Geod*., 15, pp. 235-239.

Tapley, B. D. (1973), Statistical orbit determination theory. In Resent Advances in Dynamical Astronomy, B. D. Tapley and V. Szebehely (eds.), pp. 396-425, D. Reidel Publ. Co., Holland.

Tscherning, C. C., Rapp, R. H. (1974), Closed covariance expressions for gravity anomalies, geoid undulations, and deflections of the vertical implied by anomaly degree variance models, Dep. of Geod. Sci. Rep. 208, Ohio State Univ., Columbus.

Tziavos, I. N. (1996), Comparizon of spectral techniques for geoid computations over large regions, *Journal of Geodesy*, 70, 350-373.

Wagner, C. A. (1983), Direct Determination of Gravitational Harmonics From Low-Low GRAVSAT Data, Journal of Geo. Res. Vol. 88, No. B12, pp. 10,309-10,321.

Wichiencharoen, C. (1985), Recovery of 1 deg. -mean anomalies in a local region from a low-low satellite to satellite tracking mission., Dep. of Geod. Sci., Rep. 363, Ohio State Univ., Columbus.

Wolff, M. (1969), Direct measurement of the Earth's gravitational potential using a satellite pair. *Journal of Geo. Res.,* 74(22), pp. 5295-5300.

Zhang, C. (1995), A general formula and its inverse formula for gravimetric transformation by use of convolution and deconvolution techniques, *Journal of Geodesy*, 70, pp. 51-64.